Chair of Designing Plastics and Composite Materials

Doctoral Thesis

Prediction of the failure behaviour in steel cable reinforced rubber components using the Finite Element Method

Siegfried Martin Frankl, MEng

August 2022

MONTANUNIVERSITÄT LEOBEN
www.unileoben.ac.at

AFFIDAVIT

I declare on oath that I wrote this thesis independently, did not use other than the specified sources and aids, and did not otherwise use any unauthorized aids.

I declare that I have read, understood, and complied with the guidelines of the senate of the Montanuniversität Leoben for "Good Scientific Practice".

Furthermore, I declare that the electronic and printed version of the submitted thesis are identical, both, formally and with regard to content.

Date 26.08.2022

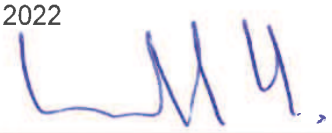

Signature Author
Siegfried Martin Frankl

Acknowledgements

The research work of this thesis was carried out at the Chair of Designing Plastics and Composite Materials at Montanuniversitaet Leoben. The research was carried out in cooperation with our industrial partner Semperit Technische Produkte GesmbH and was supported by the Austrian Research Promotion Agency (FFG) within the "BRIDGE" framework as part of the project "Entwicklung einer Methodik zur Vorhersage des Versagens in elastomeren Gurten mittels Finite Elemente Simulation", grant agreement 864702. Therefore, I would like to thank those who gave me guidance and support.

Special thanks go out to:

Univ.-Prof. Clara Schuecker, head of the chair Designing Plastics and Composite Materials and my academic supervisor of this work, for her trust, excellent supervision, and the opportunity to write this work at her chair. Clara's vast experience and knowledge guided me through this research.

Univ.-Prof. Reinhard Pippan, acting as my thesis mentor, for his interest in my work and the useful discussions.

Univ.-Prof. Otmar Kolednik for his valuable inputs using the concept of configurational forces.

My supervisor Dr. Martin Pletz the project leader from the university side, for support and guidance through my research work. His scientific background enables me to develop new procedures and explore the field of fracture mechanics.

My colleagues at the Chair of Designing Plastics and Composite Materials for the interesting discussions and the pleasant working atmosphere. I really enjoyed being part of the team.

Employees of the R&D group of our industrial partner, in particular DI Alfred Wondracek the project leader from the company side and Florian Arthofer. Their practical experience and stimulating discussions were always essential for the progress of my research.

My parents Siegfried and Katharina for their support, patience, and encouragement throughout my life. I am glad to have a wonderful family. Thank you for everything.

Abstract

Reinforced rubber components are omnipresent and widely used. The damping properties, frictional behaviour, and the large tolerable elastic deformation are indispensable for industrial applications. High-loaded components such as springs, dampers, hydraulic hoses, and conveyor belts are reinforced with steel wires or steel cables. A total failure of such components usually leads to a standstill of the entire system. A component repair or replacement is required to continue operation. Therefore, it is essential to increase the lifetime of such components.

To increase lifetime, the modes and causes of failure need to be known. In reinforced rubber, debonding of the reinforcement/rubber interface and rubber fracture out of the interface occur and lead to ultimate failure. The ability to predict failure enables the optimisation of such components to increase lifetime.

In this work, concepts to predict failure in steel cable reinforced conveyor belts using fracture mechanics are presented. Therefore, the stress and strain fields for later use in fracture mechanics are determined using Finite Element Method (FEM) models. A FEM model captures the mechanical load occurring in a conveyor belt test rig on a global scale. The mechanical response of the steel cables during tension, bending, and torsion due to their wound structure is captured using special modelling approaches. For later use of fracture mechanics on the local scale, more accurate stress and strain fields are evaluated using a submodel. A fracture-mechanical concept is used to predict debonding at the steel cable ends. Predicting rubber fracture out of the interface is a big issue and leads to a high computational effort. Therefore, a concept based on configurational forces is developed to predict rubber fracture more efficiently.

The presented concepts are crucial steps to predict failure in conveyor belts. In the future, the concepts can be adapted and applied in the 3D case to predict failure in conveyor belts. Such a fracture-mechanical procedure is general and can be transferred to other reinforced rubber components.

Kurzfassung

Verstärkte Gummikomponenten sind allgegenwärtig und weit verbreitet. Die Dämpfungseigenschaften, das Reibungsverhalten und die große tolerierbare elastische Verformung sind unverzichtbar für industrielle Anwendungen. Hochbelastete Bauteile wie Federn, Dämpfer, Hydraulikschläuche und Förderbänder werden mit Stahldrähten und Stahlseilen verstärkt. Bei einem Totalausfall muss in der Regel das gesamte System gestoppt werden. Um den Betrieb fortzusetzen, ist eine Reparatur oder ein Austausch der Komponente erforderlich. Daher ist es wichtig, die Lebensdauer solcher Komponenten zu erhöhen.

Um die Lebensdauer zu erhöhen, müssen die Versagensarten und -ursachen bekannt sein. Bei verstärktem Gummi tritt eine Ablösung der Grenzfläche Verstärkung/Gummi und Rissausbreitung in den Gummi aus der Grenzfläche auf und führt zu endgültigem Versagen. Die Fähigkeit, Versagen vorherzusagen, ermöglicht die Optimierung solcher Komponenten, um die Lebensdauer zu erhöhen.

In dieser Arbeit werden Konzepte zur Vorhersage des Versagens in stahlseilverstärkten Fördergurten unter Verwendung der Bruchmechanik vorgestellt. Daher werden die Spannungs- und Dehnungsfelder für die spätere Verwendung in der Bruchmechanik mit der Finite-Elemente-Methode (FEM) ermittelt. Ein FEM-Modell erfasst die in einem Fördergurtprüfstand auftretenden mechanischen Belastungen auf globaler Ebene. Das mechanische Verhalten der Stahlseile bei Zug, Biegung und Torsion, aufgrund ihrer gewundenen Struktur, wird mit speziellen Modellierungsansätzen erfasst. Für die spätere Nutzung der Bruchmechanik auf lokaler Ebene werden genauere Spannungs- und Dehnungsfelder mithilfe eines Submodells ausgewertet. Ein bruchmechanisches Konzept wird verwendet, um die Ablösung an den Seilenden vorherzusagen. Die Vorhersage von Rissen in den Gummi aus der Grenzfläche heraus ist eine große Herausforderung und führt zu einem hohen Rechenaufwand. Daher wird ein Konzept entwickelt, um Risswachstum im Gummi unter Verwendung des Konzepts der konfigurellen Kräfte effizienter vorherzusagen.

Die vorgestellten Konzepte sind entscheidende Schritte, um das Versagen von Förderbändern vorherzusagen. In Zukunft können die Konzepte angepasst und im 3D-Fall angewendet werden, um das Versagen von Fördergurten vorherzusagen. Solche bruchmechanischen Verfahren sind allgemein und auf andere verstärkte Gummikomponenten übertragbar.

Contents

List of Abbreviations and Symbols

Abbreviations

FEM	Finite Element Method
FM	Fracture Mechanics
HS	Homogenised Stiffness
MERR	Maximum Energy Release Rate
TAC	Targeted Angle Correction

Symbols

a	Crack length
d_{drum}	Diameter of the drums
F	Force
$F(t)$	Time dependent force
$\mathbf{f}$	Nodal configurational force vector
G_{c}	Fracture toughness
t	Time
u	Displacement
v	Velocity
Δa	Crack propagation increment
σ_{I}	Maximum principal stress
$\sigma_{\mathrm{I\,max}}$	Highest maximum principal stress
φ_{err}	Permissible angle error

List of Figures

List of Tables

1 Introduction

Reinforced rubber components are widely used and indispensable for industrial applications since there are no alternatives for use under high loads and when flexibility is also required. Rubber as matrix material is essential for these applications. The main reasons for using rubber as a matrix material are the large tolerable elastic deformations and specific properties like damping and frictional behaviour. These components are partially reinforced to achieve the requirements of springs, dampers, hydraulic hoses, and conveyor belts. The focus of this work lies in conveyor belts.

Conveyor belts of different sizes are used to transport bulk materials, as shown in Fig. 1.1 (a). In mines, the loose bulk materials (such as ore) are transported using conveyor belts over distances of up to several kilometres and must endure heavy loads. To sustain the heavy loads, conveyor belts of the highest strength classes are used. In these strength classes, conveyor belts are reinforced with steel cables in the longitudinal direction, as shown in Fig. 1.1 (b). These belts are referred to as *steel cable reinforced conveyor belts*. The necessary total length of several kilometres leads to issues with the transport and the manufacturing of endlessly connected conveyor belts. Therefore, the conveyor belt is manufactured in smaller, easy-to-handle segments. To connect the segments, the rubber is stripped from the steel cables at the ends of segments and then the segments are connected using a specific laying scheme of steel cables, as shown in Fig. 1.1 (c). The process is performed on-site to get an endless conveyor belt using a mobile vulcanisation press. The connection of two belt segments is called a *splice*. The splice is the weak point in a conveyor belt because there are no continuous steel cables and the tensile load has to be transferred by shear stress in the rubber between the steel cables.

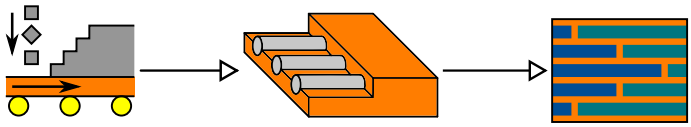

Figure 1.1: Application of a conveyor belt, which is used to transport loose bulk material (a). The geometry shows the necessary steel cable reinforcement due to the heavy load (b). The splice is used to connect the single belt segments to an endless conveyor belt (c).

The ultimate failure of a conveyor belt in the field is associated with high costs due to a transport stop and, in the worst case, the downtime of a mine. Therefore, it is of tremendous interest to avoid failure. Hence, conveyor belts are standardised in terms of their functional and structural requirements [1], reinforcement design [2], and requirements for underground use [3]. Also, vulcanised splices and the essential requirements depending on the conveying task are standardised in [4] and [5], respectively. Therefore, the technical communication

is simplified and the overall quality and reliability of belts from the various manufacturers are comparable. Research has been conducted to study conveyor belts to prevent failure by increasing knowledge and understanding.

Failure in conveyor belts results from mechanical loading and deformation during use. In use, the conveyor belt is loaded with bulk material and runs over rolls. The first step in investigating failure is to determine forces, pressures, and deformations of the conveyor belt running over rolls, as done by Fedorko and Ivančo [6] and Mikušová and Millo [7] using a *Finite Element Method* (FEM) model. Furthermore, it is also important to investigate the deformation from a flat to a tubular conveyor belt shape, as done by Fedorko *et al.* [8] and Fedorko and Molnar [9] using FEM. Therefore, the dynamic interactions with conveyed bulk material particles and system components such as idlers and drums are essential. To investigate this, Fimbinger [10] presents a methodology using the discrete element method.

Since the splice is the weak point, a closer investigation has to focus on the splice of a conveyor belt. For a splice to work, the splicing process and the splicing geometry work together. Currently, the splicing is performed manually at the place of use. The manufacturing accuracy and quality as well as the necessary manufacturing time are decisive factors. To improve the splice quality and minimise the downtime of a belt conveyor, Zaremba *et al.* [11] investigated the manual splicing process with a focus on using a pure water jet to remove the rubber from the steel cables to automate the splicing process. The used splice geometry, laying scheme, and rubber compounds influence the load transfer through the whole splice, which influences the location of the highest stressed region. This is investigated by Keller [12] using simplified small steel cable rubber test specimens and specimen FEM models. Also, the influence of debonded steel cables and cable rupture on the load transfer in the splice is investigated. The used material model and parameters to model the rubber compounds influence the mechanical response in the splice. Therefore, a procedure to evaluate material parameters for the rubber compounds is developed by Froböse [13]. The investigation of failure in conveyor belt splices and their prediction can contribute to further optimisation. Especially, the failure in the interface between steel cable and rubber is important. This is investigated by Li *et al.* [14] using a shear damage criterion in a FEM model, where the steel cable pull-out force is validated by experimental results. The prediction of failure in conveyor belt splices, however, has not yet been explored in depth.

The failure mechanisms occurring in a conveyor belt splice are shown in Fig. 1.2. As described by Keller [12], steel cable rupture, see Fig. 1.2 (a), appears at high test loads and a low number of load cycles. On the other hand, at low test loads and a high number of load cycles, debonding of steel cables or rubber fracture occurs, as shown in Fig. 1.2 (b), (c), and (d). Keller also mentions that the failure of a conveyor belt typically does not occur spontaneously,

but progressively. Debonding of steel cables is observed on cable ends in the splice or on ruptured cables. Kinking of a crack into the rubber, see Fig. 1.2 (d), occurs on ruptured cables or debonded steel cables and leads to ultimate failure, as shown in Fig. 1.2 (e).

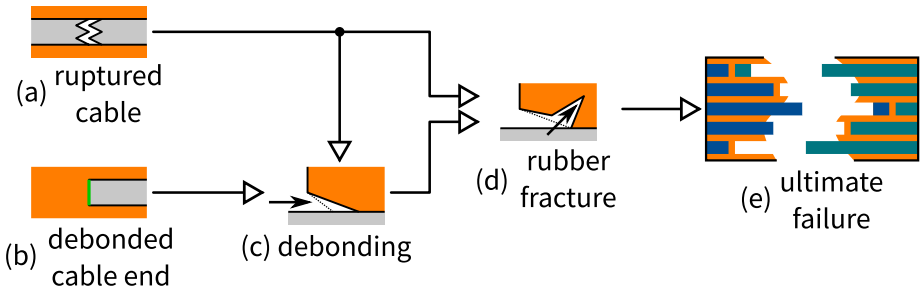

Figure 1.2: Failure mechanisms in a conveyor belt: Debonding of steel cables (c) occurs at ruptured cables (a) and cable ends in the splice (b). Rubber fracture (d) appears at ruptured cables or by kinking of debonded cracks out of the interface and leads to ultimate failure (e).

The overall goal of this conveyor belt research is to improve the cyclic strength of the splice, which is determined experimentally by a standardised test [15]. In this test, a conveyor belt with one splice is running (with a velocity v) on a test rig with two drums, see Fig. 1.3. An additional oscillating force $F(t)$ is applied to the drums, which stretches the belt in the longitudinal direction. The determination of this strength is relevant because the same failure mechanisms occur as in the real application.

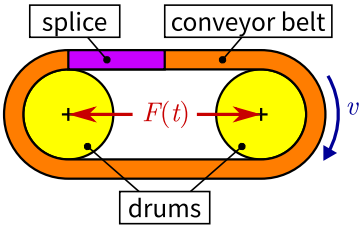

Figure 1.3: Test setup to evaluate the cyclic strength of conveyor belts [15].

2 Hypothesis and state of the art

In this work, the focus lies on the prediction of failure of the splice of a steel cable reinforced conveyor belt. The common approach to predict failure is shown in Fig. 2.1. This approach is divided into three parts. The test rig (a), where the failure should be predicted, such as the test rig from [15], where the cyclic strength of a splice is determined. In the FEM modelling (b), stress and strain fields are determined based on the load situation on the test rig using FEM models. The failure mechanisms occurring in a conveyor belt splice are assessed using the determined stress and strain fields in the failure assessment (c). Based on the assessment, the failure on the test rig is predicted.

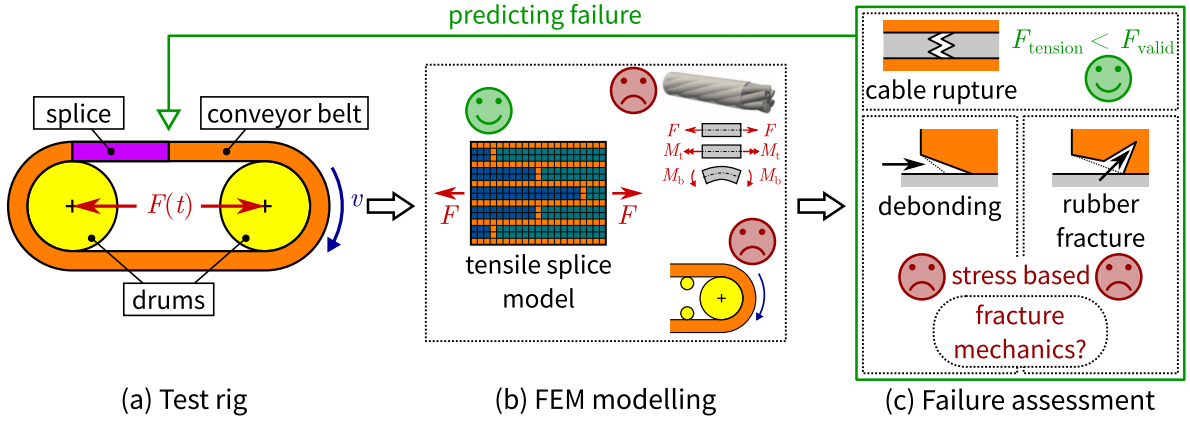

Figure 2.1: Schematic of predicting failure of conveyor belts: Test rig to evaluate the cyclic strength of a splice (a), where failure should be predicted. Available FEM models in the literature (b), where accurate steel cable modelling and the bending around the drums are missing. Relevant failure mechanisms in a splice, which should be assessed using the models (c).

As a first approximation, the splices are loaded in tension using FEM, as shown in Fig. 2.1 (b). These splice models contain one or more rubber layers and embedded steel cables. First FEM models are presented by Nordell *et al.* [16] and further ones by Keller [12] and Froböse *et al.* [17]. For the rubber, a hyperelastic material model is used. The steel cables are approximated by solid cylinders with an isotropic linear elastic material model [12], [17] or by using special FEM elements [16]. Steel cable rupture can be predicted in a simplified way using a tensile force criterion, as shown in Fig. 2.1 (c). Such a tensile force criterion is described in [18]. These tensile FEM models are used for splice optimisation to avoid debonding and rubber fracture based on stresses evaluated in the rubber. Also, the influence on the stress fields of ruptured and debonded steel cables is investigated, as done by Keller [12].

The hypothesis of this work: The failure in conveyor belt splices can be predicted using FEM models. To this end, FEM models in combination with *Fracture Mechanics* (FM) concepts are used. FEM models compute accurate stress and strain fields on a global scale that can be used on the small scale with FM concepts to predict failure.

To this end, various improvements and solutions to detailed problems are developed to solve the whole issue. On the test rig, the conveyor belt is bent around the drums. In the available FEM splice models, bending around the drums is not taken into account. However, Nordell *et al.* [16] mentioned that bending a splice around a drum can significantly influence the resulting stresses in the belt. Neglecting the effect of bending in the FEM model results in uncertainties in the stress and strain results, as highlighted in Fig. 2.1 (b). Therefore, the bending around the drums has to be taken into account.

Steel cables show high tensile stiffness, low bending stiffness compared to a solid, and a tension-torsion coupling as a result of the wound structure, as described in Costello [19]. The specific elastic response of steel cables is investigated by various research groups. Chen *et al.* [20] experimentally investigated the bending of steel cables with a focus on the clamping of the cable ends and found a significant influence on the bending stiffness. A distinct tension-torsion coupling due to axial tensile load is reported by Utting and Jones [21]. Furthermore, in conveyor belts, the rubber penetrates the steel cables. Bonneric *et al.* [22] investigated the influence of rubber penetration in steel cables using FEM models and obtained an increasing bending stiffness. In the conveyor belt splice, the steel cables are not aligned in a straight way and are not arranged exactly in the load direction. In this case, where the steel cables are realigned during loading, the approximation of a steel cable as a solid cylinder in FEM using isotropic linear elastic material models yields unacceptable errors in tensile forces and stresses because of neglecting the mechanical steel cable response, as highlighted in Fig. 2.1 (b).

Rubber is the main component of a conveyor belt. The mechanical properties of rubber depend on its molecular structure, as described in Röthemeyer and Sommer [23] and Gent [24]. Rubber is a viscoelastic and nearly incompressible material with a Young's modulus range of $0.1\,\mathrm{MPa}$ to $100\,\mathrm{MPa}$ [23]. The deformation behaviour is hyperelastic with endurable strains from $100\,\%$ up to $1000\,\%$ [23]. Therefore, rubber ensures the necessary flexibility of conveyor belts. Rubber is a brittle material because no plasticity occurs even at high temperatures. To predict failure in the rubber, FM can be used. The strain energy release rate criterion proposed by Griffith [25] is successfully used by Rivlin and Thomas [26] to describe crack growth. The fracture toughness of rubber ranges from less than $100\,{}^{\mathrm{J}}/_{\mathrm{m}^2}$ up to several ${}^{\mathrm{kJ}}/_{\mathrm{m}^2}$ [24].

For failure assessment, a stress-based concept for debonding of steel cables and rubber fracture has been used [12], [17]. However, the evaluated rubber stresses at the cable ends are mesh dependent and the mesh size affects the stress peak. Therefore, with a stress-based prediction of failure (debonding and rubber fracture) only a qualitative statement is possible, as shown in Fig. 2.1 (c). Accurate quantitative failure modelling using FM is missing. FM can be used to predict the failure of components that fail due to crack growth. The main concepts for assessing whether and in which direction a crack will propagate are based on Griffith [25], Irwin [27], Rice [28], and Eshelby [29]. The crack propagates if the computed crack-driving force is bigger or equal to the crack growth resistance of the material. Therefore, it is essential to determine the crack-driving force numerically. This has been done by Sun and Davidson [30]

by determining the energy release rate, taking into account the effects of friction and geometric nonlinearities. An overview of concepts to determine 2D crack propagation direction in homogeneous materials is given by Brouzoulis *et al.* [31]. As mentioned above, to predict the direction of crack propagation in rubber, a concept based on the strain energy release rate is necessary, which is valid for rubber. Such a concept is the *Maximum Energy Release Rate* (MERR) concept. The propagation direction of MERR can be found by introducing trial cracks, see Hellen [32]. In the case of conveyor belts, the initial cracks are located in the interfaces between the steel cables and the rubber matrix. In this case, further debonding or kinking of a crack out of the interface is possible. The kinking of a crack out of the interface between two elastic solids in the 2D case is analysed by He and Hutchinson [33] using a kink criterion based on the MERR criterion. The proposed criterion uses the fracture toughnesses of the interface and the weak material.

To predict crack growth in realistic multi-material 2D structures, a FEM approach is necessary. Such an approach is presented by Oneida *et al.* [34]. In this approach, it is assumed that the crack propagates in homogeneous materials in the direction of MERR, where the fracture toughness of mode I direction can be used. For crack propagation in the interface, the fracture toughness depends on the occurring mode-mixity, as described by Evans *et al.* [35]. Therefore, the energy release rates for crack growth (and the individual mode-mixity for crack propagation in the interface) are computed numerically by introducing trial cracks. Starting from a crack in an interface or a crack tip touching an interface in a multi-material structure, as shown in Fig. 2.2 (a), for every possible crack propagation along the interface, a trial crack is introduced, see Fig. 2.2 (b). Also, the crack propagation direction is determined for every adjacent material, as shown in Fig. 2.2 (c). This is done by introducing a large number of trial cracks. The crack propagates if one ratio between energy release rate and fracture toughness of the trial cracks is bigger or equal one. The crack propagates in the direction where this ratio has a maximum. The determination of the crack propagation direction in each of the adjacent materials results in a huge computational effort, because of the large number of introduced trial cracks. Especially if the approach is transferred to the 3D case, because of the possible individual crack propagation directions and crack propagation lengths along the crack front. FM concepts have not yet been used in conveyor belts to predict steel cable debonding and further rubber fracture out of the interface.

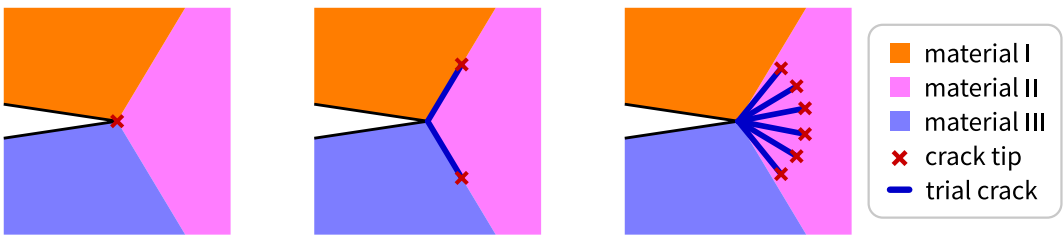

(a) starting crack (b) trial cracks in the interfaces (c) trial cracks in one neighbouring material

Figure 2.2: Multi-material structure composed of three materials and containing a crack tip touching two interfaces (a). The necessary trial cracks to investigate crack propagation in the interface (in this case two) (b) and trial cracks to investigate crack propagation in material II (c).

3 Methods and overview of publications

This work presents concepts to predict failure in steel cable reinforced conveyor belts in order to improve the cyclic strength, which is evaluated at the test rig [15]. To do so, the FEM is used on the global scale to evaluate the stress and strain fields and FM concepts are applied on the local scale for failure assessment to predict debonding and rubber fracture. The FEM modelling on the global scale is illustrated in Fig. 3.1 (a). The bending of the conveyor belt around the drums affects the stress and strain fields. Since modelling the load in the test rig is essential for predicting failure, the bending of the conveyor belt around the drums needs to be captured. Therefore, the test rig set-up is modelled using an endless belt with one splice running on two drums. To get more accurate stress and strain results for the later use of FM to predict failure, a submodelling approach is used. The test rig modelling and submodelling used are described in Paper A. To capture the specific elastic response of the steel cables, various modelling approaches are developed and investigated, as described in Paper B. The failure assessment on the local scale is illustrated in Fig. 3.1 (b). To predict debonding, an energy-based FM concept is used, as described in Paper C. In the 3D case, the prediction of rubber fracture requires high computational effort, since an enormous number of trial cracks is necessary. Therefore, a 2D concept is developed to predict the crack propagation direction more efficiently, as described in Paper D.

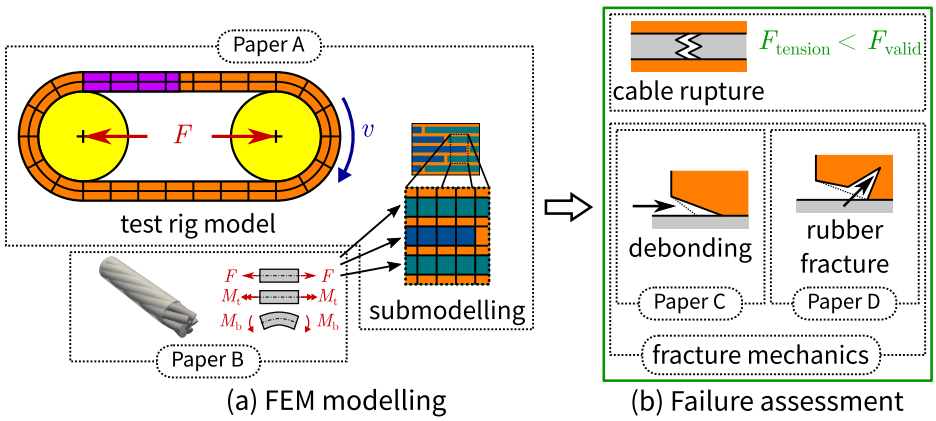

Figure 3.1: FEM modelling of the test rig (a), with steel cable modelling and an introduced submodel. Occurring failure mechanisms in a splice (b). Cable rupture is predicted using a tensile force criterion. Debonding of steel cables and crack propagation in the rubber is predicted using fracture-mechanical concepts.

3.1 Global scale: FEM modelling

This section describes the FEM modelling of the test rig, which is used to determine accurate stress and strain fields for later use to predict failure using FM concepts. It is shown, that bending around the drums of a conveyor belt can have a significant influence on the stress

and strain fields. Also, the mechanical response of the steel cables influences the stress and strain fields. Therefore, several modelling approaches for steel cables are developed and compared to model the mechanical response of a steel cable. Large deviations are obtained by using a solid cylinder instead of a more detailed steel cable model.

3.1.1 Test rig model

The test rig is modelled as an endless belt with one splice running on two drums, see Fig. 3.2. The test rig modelling is described in Paper A. To keep the model as simple as possible, the assembly of the belt and starting up the test rig are not taken into account in the model. The belt is modelled already running, with an initial velocity v. The drums are modelled as rigid bodies with frictional contact between the belt and the drums. In the initial state, the splice is located near the left drum and the regions around the drums are already bent.

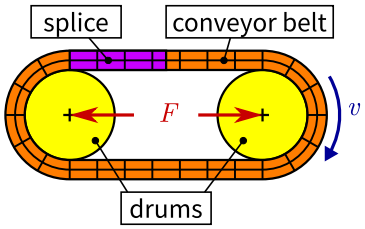

Figure 3.2: Sketch of the FEM test rig model. The test rig is modelled by a belt running on two drums.

The flat manufactured belt is modelled as being bent around the drums, which corresponds to deformation and leads to corresponding initial stresses in the belt. Therefore, stresses for a bent belt are determined in a separate model and applied as initial stresses in the test rig model for both bent regions around the drums, as shown in Fig. 3.3 (a). The element size used to discretise the gap between the cables of a few millimetres and the overall dimensions of the model of several meters results in a huge number of elements. In this model with its huge element count and where contact plays a role, a quasi-static explicit simulation is performed to reduce the computational costs and make the simulation feasible. In the test rig, the oscillating longitudinal force is applied to the drums for several thousands of revolutions of the belt. It is thereby assumed that the stress and strain fields during failure can be assessed by statically applying the maximum oscillating longitudinal force F, as shown in Fig. 3.3 (b). Starting with a running belt, the force is applied smoothly. The maximum force is reached before the splice reaches the right drum. The rubber is modelled with a hyperelastic material model. For the steel cables, a modelling approach is used that captures the tensile and bending stiffness, see Fig. 3.3 (c), as described in Sec. 3.1.2. The steel cables in reality are coated with a zinc layer to provide better steel-rubber bonding. Due to the cutting process, however, there is no zinc layer on the steel cable's ends. Therefore, the modelled steel cables are ideally bonded to the rubber everywhere, except for the steel cable ends.

As a result of applying the Force F and modelling the already running belt using initial stresses in the bent regions unwanted dynamic artefacts occur. Therefore, additional support drums and a damper are introduced to reduce initial oscillations in the running belt, see Fig. 3.3 (d). Once the maximum force has been reached, the contact between the support drums and belt is switched off in the model to avoid an influence on the results. For the later use of FM in the local-scale modelling (Sec. 3.2), more accurate stress and strain fields are necessary. Therefore, a more finely discretised submodel is used in the region of interest, see Fig. 3.3 (e). The displacement results from the test rig model are applied to the outer surfaces of the submodel, except the top surface (which does not contact the drums). The submodel is meshed twice as finely as in the test rig model.

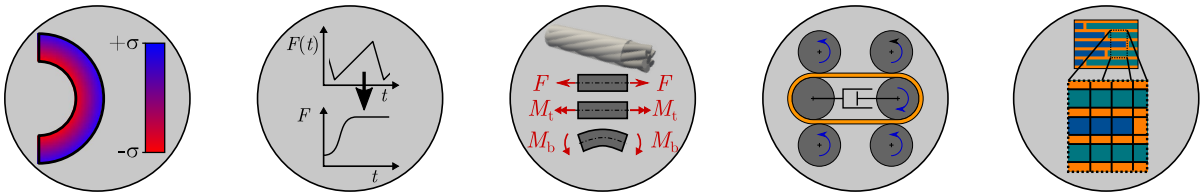

(a) bent region modelling (b) quasi-static (c) steel cable modelling (d) handle dynamic artefacts (e) sub-modelling

Figure 3.3: Modelling features of the test rig model. In the bent region, residual stresses are applied (a). The maximum oscillating load is applied smoothly in a quasi-static state (b). The steel cables are modelled with a suitable modelling approach (c), described in Sec. 3.1.2. The unwanted dynamic artefacts are eliminated by support drums and a damping element (d). A submodel approach is used to get more accurate stress and strain fields (e).

The diameter of the drums of the test rig is $d_{\mathrm{drum}} = 1.25\,\mathrm{m}$. The conveyor belt contains nine steel cables, and seven steel cables in the splice. The maximum principal stress results of the submodel in the most stressed region are plotted in Fig. 3.4 (a). The detail is located in the bent region at $t = 0.8\,\mathrm{s}$. The highest stress occurs at the debonded cable end. The highest maximum principal stresses vs. the simulation time t are plotted for the global model and the submodel in Fig. 3.4 (b). For $t < 0.65\,\mathrm{s}$, the detailed region is located in the straight region between the drums and for $t > 0.65\,\mathrm{s}$, the detailed region is located in the bent region around the drum. In the whole time range, higher maximum principal stresses are obtained in the submodel compared to the global model due to the finer mesh size. More than $17.5\,\%$ and $14.3\,\%$ higher maximum principal stresses are observed in the bent region than in the flat region for the global and submodel, respectively.

The higher stresses in the bent region show the significant influence of bending, which cannot be neglected for predicting failure. Locating the highly stressed regions and a qualitative assessment of different splice laying schemes is possible as long as similar local stress distributions occur. However, the stress singularity at the detached cable end yields higher stresses if a finer mesh size is used. Due to the mesh-dependency of the stress results, the prediction of failure based on stresses is inappropriate. Therefore, FM concepts are used in this work to quantitatively predict failure.

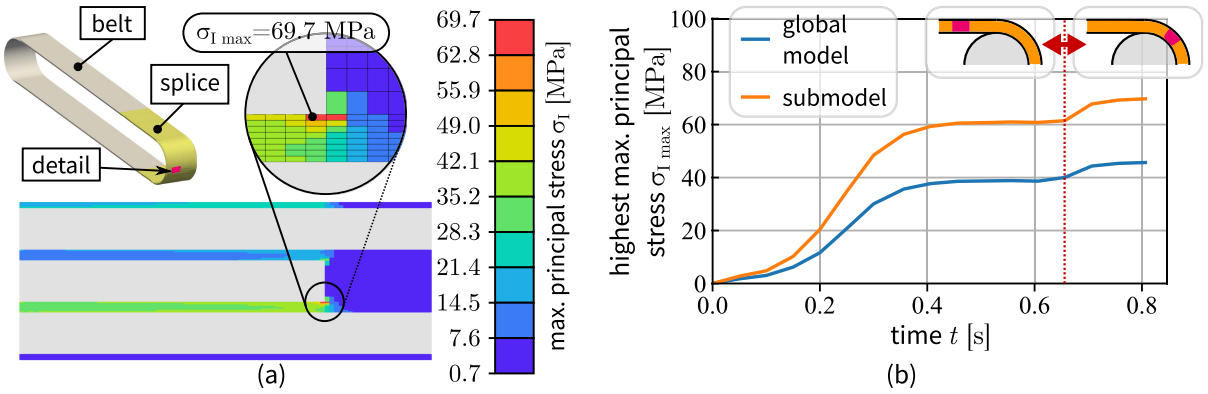

Figure 3.4: Results of the test rig model: Stress field in the submodel of the most stressed region (a), highest maximum principal stress vs. time from the global model and the submodel (b) — the transition between the straight and the bent region at $t = 0.65\,\mathrm{s}$ is marked by a red line.

3.1.2 Steel cable modelling

Steel cables are used as reinforcement in highly loaded conveyor belts. To use a tensile force criterion, as described in [18], with FEM to predict failure, the mechanical response of the steel cable has to be captured in the model. Steel cables show a high tensile stiffness, a low bending stiffness compared to a solid due to their individual steel wires, and a tension-torsion coupling due to the wound structure [19], as shown in Fig. 3.5 (a). Various modelling approaches using common finite elements are investigated in Paper B. The FEM test rig model described in Sec. 3.1.1, uses one of those approaches. The advantage of such approaches is the low computational effort compared to modelling the full steel cable geometry.

In those modelling approaches, it is assumed that the rubberised steel cables can be modelled as homogenised cylinders. By combining solid elements and/or beam elements using elastic material models the mechanical response of a steel cable is modelled. As a reference, a fully-modelled seven-wire rubberised strand is used, see Fig. 3.5 (a). The mechanical response of the modelling approaches and the reference model is characterised using the *Homogenised Stiffness* (HS) values for tension, torsion, bending, and their coupling values, as done by Cartraud and Messager [36]. The parameters of the modelling approaches are fitted to reach the same HS values as the reference model.

To model the mechanical response using beam elements, the beam elements are located on the central axis of the cylindrical solid. The beam elements and the solid elements share the same nodes on the central axis by using beam and solid elements in combination. By using beam elements only (without solid elements), the beam nodes are coupled to the corresponding rubber nodes at the cylinder surface. The tension-torsion coupling is captured using a coupling term that connects the tensile strain to the shear strain in the cylindrical

coordinate system of the steel cable. The approaches are compared with a focus on capturing the HS values of the reference model. For comparison a single cable is used. The tension, torsion, and bending deformation is applied to the cable ends.

The HS values of the approaches normalised to the HS values of the reference model are plotted for three selected cable modelling approaches in Fig. 3.5 (b). For these results, the remaining tension, torsion, or bending deformations that are not fitted are fixed. The solid, solid/beam, and beam approach use solid elements only, a combination of beam and solid elements, and only beam elements, respectively. The beam approach uses an anisotropic material considering the tension-torsion coupling using a coupling term which connects the tensile to the torsional strain. The other two approaches use linear elastic material with cubic symmetry in a cylindrical coordinate system, thereby not considering the tension-torsion coupling. The modelling approaches plotted in Fig. 3.5 (b) show good agreement for tension and torsion HS values. The solid approach as used in [12], [17] overestimates the bending HS value by a factor of nine. In the case of bending, only the solid/beam and the beam approach show good agreement with the reference. The beam approach, which also considers the tension torsion coupling, meets all four HS values on the reference.

As a first approximation, the solid/beam approach is used in the test rig model (Sec. 3.1.1). The parameters are fitted to tensile and bending test data. If tension-torsion coupling is found to be relevant, one of the other modelling approaches could be used (based on appropriate test data).

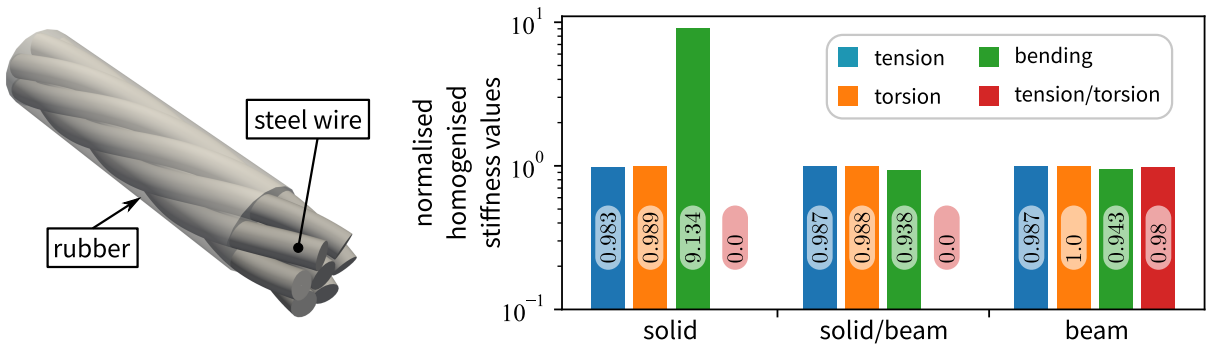

(a) rubberised steel cable

(b) homogenised stiffness values for three cable modelling approaches

Figure 3.5: Rubberised steel cables with seven wires (a). Normalised homogenised stiffness values for solid, solid/beam, and beam approaches (b).

3.2 Local scale: failure assessment

Classical FM concepts are not directly applicable to conveyor belts because conveyor belts contain multiple material interfaces and large strains occur in the rubber. This section describes how FM concepts can be used to predict debonding and crack propagation. To predict rubber

fracture out of the interface for a crack tip located in the interface, the crack propagation direction has to be determined by examining all adjacent materials with trial cracks. To reduce the necessary number of introduced trial cracks, a new concept for homogeneous materials is presented to find the crack propagation direction more efficiently.

An incremental crack propagation concept predicts crack propagation, as shown in Fig. 3.6. It predicts the crack driving force starting from an initial crack. If the crack propagation criterion is met, the crack propagates by a crack increment; otherwise, the load is increased. For further crack propagation, the procedure is repeated.

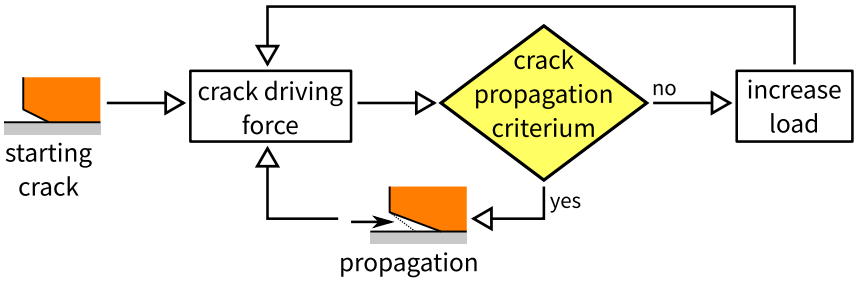

Figure 3.6: Flowchart of the incremental crack propagation.

3.2.1 Debonding

A FM concept is implemented and adapted to predict debonding failure in a fibre pullout test. The application is demonstrated, as presented in Paper C, using an axial-symmetric FEM model, see Fig. 3.7 (a). A glass fibre bundle is embedded in a silicone rubber matrix and pulled against a punch. The starting crack is modelled as a cylindrically debonded fibre bundle. Contact with friction is modelled between punch and specimen and also between the crack flanks. To predict failure, it is assumed that only debonding occurs and no kinking of the crack out of the interface occurs. Also, it is assumed that the fracture toughness of the interface is independent of the occurring mode-mixity at the crack tip. To predict crack propagation, the incremental crack propagation concept is used. The energy release rate is computed by the energy difference between two models with different crack lengths. Furthermore, the dissipated frictional energy is taken into account. The influence of the fracture toughness, crack propagation increment, and friction coefficients are investigated.

The resulting maximum principal stress σ_{I} fields are shown in Fig. 3.7 (a) with a crack length of $a = 4\,\mathrm{mm}$ and an applied displacement of $u = 1\,\mathrm{mm}$. The tensile force F vs. the applied displacement u is plotted in Fig. 3.7 (b) for a fracture toughness of $G_{\mathrm{c}} = 700\,\mathrm{J/m^2}$ and a crack propagation increment of $\Delta a = 1\,\mathrm{mm}$. A crack propagation by one crack propagation increment Δa causes a vertical jump in F. Higher G_{c} values cause crack propagation at higher loads (higher displacements u). A smaller Δa yields a smaller vertical jump in F. Therefore, for an accurate evaluation of F, a small Δa value has to be used. It is observed that in this

model, the frictional dissipation is much smaller than the strain energy. Therefore, frictional dissipation is not considered when computing the energy release rate. However, for a higher friction coefficient, crack propagation occurs slightly earlier, since the stress field is influenced by crack closure in the region close to the punch.

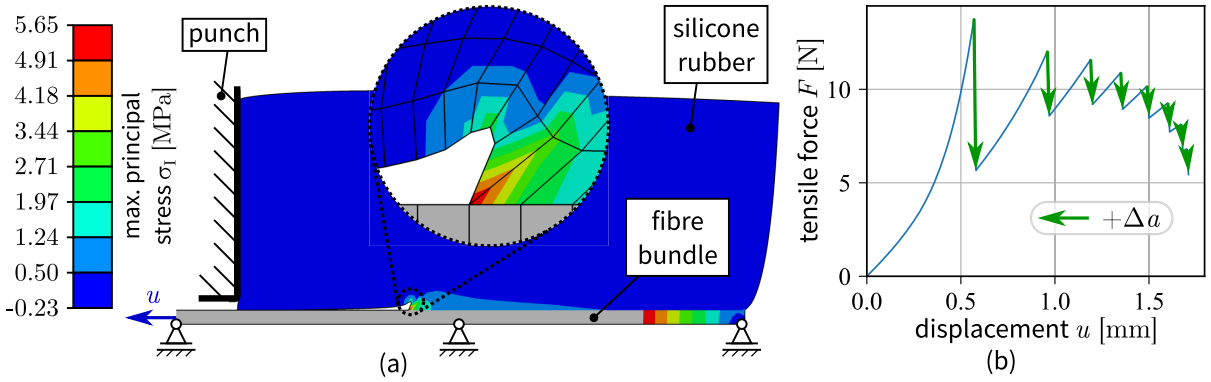

Figure 3.7: Maximum principal stress field of a loaded specimen in a fibre pullout test (a). Tensile force vs. displacement during crack propagation (b), where Δa is the crack propagation increment.

3.2.2 Crack propagation

Crack propagation concepts are used to determine whether or not a crack propagates and to determine the crack propagation direction. In homogeneous materials, these concepts are divided into explicit and implicit crack propagation concepts: Explicit concepts use the current crack to evaluate crack propagation and in implicit concepts, the propagated trial crack is used. To predict crack propagation of a crack kinking out of an interface in multi-material structures, explicit concepts are only applicable to simple cases [33]. Therefore, an implicit concept is more suitable to predict the crack propagation direction in every neighbouring material by trial and error, as done by Oneida *et al.* [34]. This technique requires a high number of trial cracks for every neighbouring material, which results in high computational costs. Therefore, a more efficient concept is developed to evaluate the crack propagation direction in homogeneous materials based on MERR, as presented in Paper D.

The developed 2D concept is based on configurational forces and uses nodal configurational forces $\mathbf{f}$ occurring at the nodes near the trial crack increment containing the crack tip, see Fig. 3.8. To find the propagation direction for MERR, a crack correction angle is computed from the occurring $\mathbf{f}$. The concept takes advantage of the fact that configurational forces can be interpreted as an energy gradient caused by a change in geometry. Based on the configurational forces, an iterative Targeted Angle Correction (TAC) of the trial crack increment (containing the crack tip) is done, which finds the direction of MERR in a targeted manner. To identify the crack propagation direction of MERR using TAC, a permissible angle error is introduced to stop the iterative process. The approach is tested in a three-point bending

model to predict crack paths using incremental crack propagation, where the influence of the permissible angle error is also examined. The accuracy of the concept is evaluated in a simplified model.

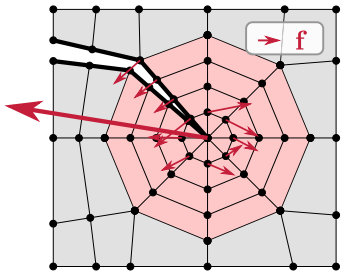

Figure 3.8: Nodal configurational forces $\mathbf{f}$ around the trial crack increment (containing the crack tip) are used to determine the crack correction angle.

Predicted crack paths of a three-point bending plate containing three holes and three initial crack positions are plotted in Fig. 3.9. The crack paths are predicted using an explicit concept based on the crack tip configurational force and the implicit TAC concept for various propagation increments. For crack paths B and C, where also experimental tests from [37] are available, both concepts provide similar results. However, initial crack C shows deviations between the two concepts and the used propagation increment. It is shown that in finding the propagation direction of MERR, implicit concepts are more accurate than explicit ones. However, the curvature of the crack path and the used propagation increment determine the accuracy. The TAC concept is as accurate as the implicit concept using a range of seven trial cracks in finding the propagation direction of MERR and requires approximately 4.7 times less computational effort in the case considered (using a permissible angle error of $\varphi_{\mathrm{err}} = 0.4^{\mathrm{o}}$). Compared to the explicit concept used, which is based on the crack tip configurational force, the TAC concept gives considerably more accurate results but requires only approximately 1.5 times more computational effort.

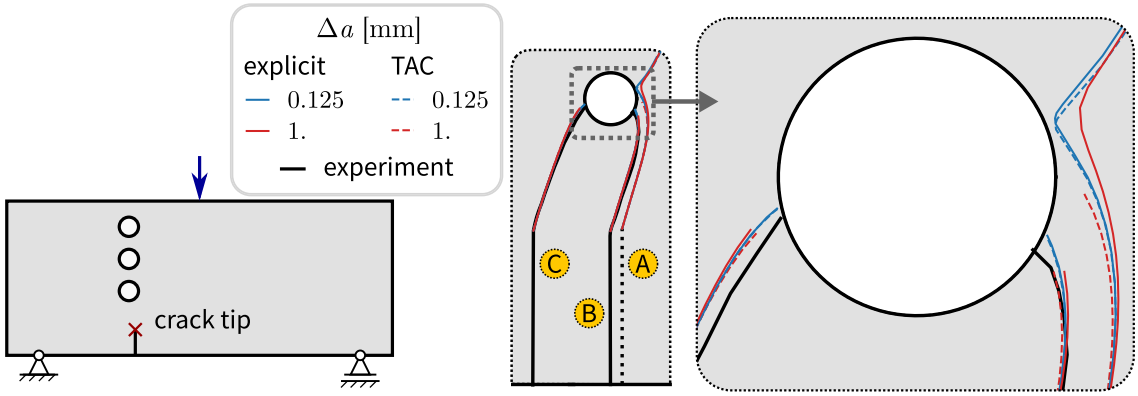

Figure 3.9: Predicted crack paths with the explicit and the TAC concept for various crack propagation increments Δa. The experimental results from [37] are shown as black lines.

4 Conclusions

This work presents concepts to predict failure in conveyor belts. The aim is to increase the prediction quality by using physically-based fracture-mechanical concepts instead of stress-based concepts. Essential elements for the prediction are developed and published in various papers. The developed models and concepts can be connected to predict failure in conveyor belts running on a test rig, as shown in Fig. 4.1: A FEM model of the test rig is developed to capture the stress and strain fields in the conveyor belt. The necessary length scale to capture the mechanical response in the conveyor belt and the length scale where failure occurs differ severely. Therefore, a multi-scale approach is used. The critical part of the conveyor belt is additionally modelled in a submodel. To predict failure, cable rupture and debonding of steel cables are considered. Cable rupture and progressive debonding cause ultimate failure. Additionally, first steps towards modelling rubber fracture and kinking of a crack out of an interface have been taken.

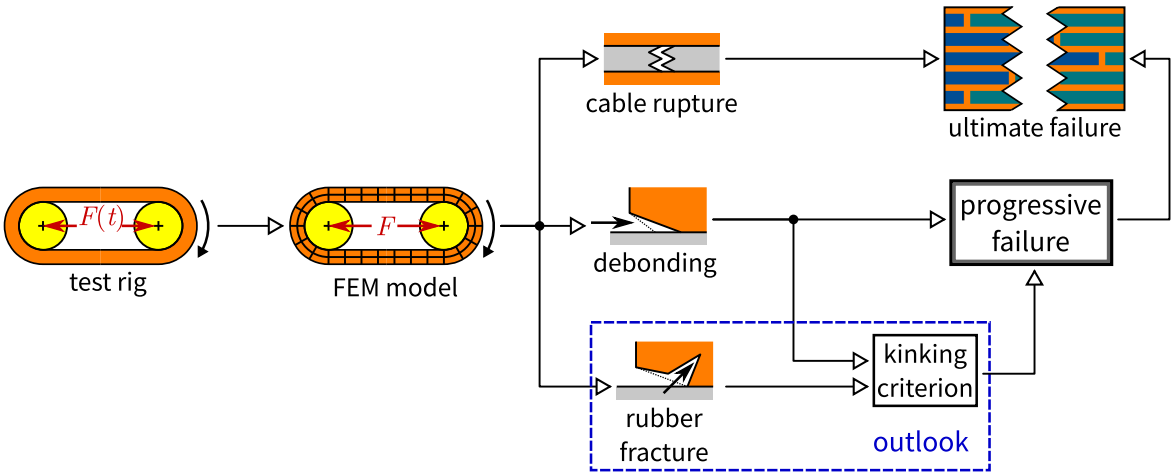

Figure 4.1: Approach to predict failure in conveyor belts: The test rig setup and the developed FEM model are shown. The model assesses failure mechanisms such as cable rupture, debonding, and rubber fracture, which lead to progressive failure and can lead to ultimate failure.

The mechanical response in the conveyor belt running on the test rig is captured in a quasi-static FEM model. The bending around the drums, which can have a significant influence on the stress and strain fields, is taken into account. Also, the simplifications in the steel cable modelling approach influences the stress and strain fields. Various steel cable modelling approaches capturing the mechanical response of steel cables are investigated and compared to a fully-modelled steel cable. The steel cable modelling approach used in the test rig model captures the low bending stiffness compared to the high tensile stiffness of a steel cable. Modelling the belt's bending and the mechanical steel cable response allow for the determination of accurate displacement fields. Cable rupture can thus be assessed more reliably based on the cable forces. However, the prediction of steel cable debonding and rubber fracture

using stresses is limited due to the mesh dependence near stress singularities. Therefore, submodels with smaller mesh size are introduced, where fracture-mechanical concepts can be used.

An energy-based fracture-mechanical concept is used to predict debonding. For a given initial debonding, further debonding can be predicted by introducing a propagated crack. Therefore, the crack-driving force is evaluated and is compared to the interface fracture toughness. This concept can be directly applied to the submodel in the 3D case to predict debonding of the steel cables in a conveyor belt assuming a constant crack propagation increment. The prediction of rubber fracture out of an interface, however, is a big challenge in the 3D case.

To predict crack kinking out of the interface, both debonding and crack kinking have to be considered. In the 3D case, crack kinking results in a huge number of possible crack propagation directions around the debonded steel cable. Doing this by trial and error results in high computational cost. To reduce this computational effort, an efficient concept to find the crack propagation direction in homogeneous 2D materials is developed. This concept determines a crack correction angle for an existing trial crack to meet the crack propagation criterion of maximum energy release rate. Using this 2D concept, the computational effort is significantly reduced compared to using trial and error. In the 3D case, this idea of correcting an existing trial crack around the steel cable to meet the crack propagation criterion can be used as well but needs some assumptions about the crack shape. In future work, the concept will be adapted and applied in the 3D case to predict crack kinking with reduced computational effort.

In summary, this work presents some crucial steps in predicting conveyor belt failure were taken on different length scales. In the future, these steps can be merged to get a multi-scale approach that can predict debonding of steel cable and kinking of cracks in a conveyor belt splice.

5 Literature/References

[1] 'DIN EN ISO 15236-1:2017-03, Steel cord conveyor belts - Part 1: Design, dimensions and mechanical requirements for conveyor belts for general use', Beuth Verlag GmbH, Tech. Rep.

[2] 'DIN EN ISO 15236-2:2017-06, Steel cord conveyor belts - Part 2: Preferred belt types', Beuth Verlag GmbH, Tech. Rep.

[3] 'DIN EN ISO 15236-3:2018-08, Steel cord conveyor belts - Part 3: Special safety requirements for belts for use in underground installations', Beuth Verlag GmbH, Tech. Rep.

[4] 'DIN EN ISO 15236-4:2004-09, Steel cord conveyor belts - Part 4: Vulcanized belt joints', Beuth Verlag GmbH, Tech. Rep.

[5] 'DIN 22101:2011-12, Continuous conveyors - Belt conveyors for loose bulk materials - Basis for calculation and dimensioning', Beuth Verlag GmbH, Tech. Rep.

[6] Fedorko, G. and Ivančo, V., 'Analysis of Force Ratios in Conveyor Belt of Classic Belt Conveyor', *Procedia Engineering*, vol. 48, pp. 123–128, 2012.

[7] Mikušová, N. and Millo, S., 'Modelling of Conveyor Belt Passage by Driving Drum Using Finite Element Methods', *Advances in Science and Technology Research Journal*, vol. 11, no. 4, pp. 239–246, 2017.

[8] Fedorko, G., Ivančo, V., Molnár, V. and Husáková, N., 'Simulation of Interaction of a Pipe Conveyor Belt with Moulding Rolls', *Procedia Engineering*, vol. 48, pp. 129–134, 2012.

[9] Fedorko, G. and Molnar, V., 'Design of a calculation fem model of the test static set-up of pipe conveyor for analysis of contact forces', *Advances in Science and Technology Research Journal*, vol. 11, no. 2, pp. 220–225, 2017.

[10] Fimbinger, E., 'A Methodology for Dynamic Belt Simulation', PhD Thesis, Montanuniversität Leoben, Austria, 2021.

[11] Zaremba, D., Heitzmann, P., Overmeyer, L., Hillerns, L. and Hassel, T., 'Automatable Splicing Method for Steel Cord Conveyor Belts – Evaluation of Water Jetting as a Preparation Process', *Strojniški vestnik - Journal of Mechanical Engineering*, vol. 63, no. 10, pp. 590–596, 2017.

[12] Keller, M., 'Zur Optimierung hochfester Stahlseilgurtverbindungen', PhD Thesis, Universität Hannover, 2001.

[13] Froböse, T., *Verfahren zur Ermittlung der Materialparameter für die Auslegung von Stahlseil-Fördergurtverbindungen mit Hilfe der FEM*, ser. Berichte aus dem ITA 2017, Band 01. Garbsen: PZH Verlag, 2017.

[14] Li, X., Long, X., Jiang, H. and Long, H., 'Influence of different cord pitch on the pullout force of steel cord conveyor belt splice', *Journal of Adhesion Science and Technology*, vol. 32, no. 20, pp. 2268–2281, 2018.

[15] 'DIN 22110-3:2015-04, Testing methods for conveyor belt joints - Part 3: Determination of time strength for conveyor belt joints (dynamical testing method)', Beuth Verlag GmbH, Tech. Rep.

[16] Nordell, L., Qiu, X. and Sethi, V., 'Belt conveyor steel cord splice analysis using finite element methods', *Bulk Solids Handling;(Switzerland)*, vol. 11, no. 4, pp. 863–868, 1991.

[17] Froböse, T., Heitzmann, P., Overmeyer, L. and Wakatsuki, A., 'Entwicklung eines FE-Modells zur Optimierung von Stahlseil-Fördergurtverbindungen', *Logistics Journal: Proceedings*, no. 1, p. 8, 2014.

[18] 'DIN 15020-1:1974-02, Lifting Appliances; Principles Relating to Rope Drives; Calculation and Construction', Beuth Verlag GmbH, Tech. Rep.

[19] Costello, G. A., *Theory of Wire Rope*. Springer Science & Business Media, 1997.

[20] Chen, Z., Yu, Y., Wang, X., Wu, X. and Liu, H., 'Experimental research on bending performance of structural cable', *Construction and Building Materials*, vol. 96, pp. 279–288, 2015.

[21] Utting, W. and Jones, N., 'The response of wire rope strands to axial tensile loads—Part II. Comparison of experimental results and theoretical predictions', *International Journal of Mechanical Sciences*, vol. 29, no. 9, pp. 621–636, 1987.

[22] Bonneric, M., Aubin, V. and Durville, D., 'Finite element simulation of a steel cable - rubber composite under bending loading: Influence of rubber penetration on the stress distribution in wires', *International Journal of Solids and Structures*, vol. 160, pp. 158–167, 2019.

[23] F. Röthemeyer and F. Sommer, Eds., *Kautschuk-Technologie: Werkstoffe - Verarbeitung - Produkte*, 3., neu bearb. und erw. Aufl. München: Hanser, 2013.

[24] A. N. Gent, Ed., *Engineering with rubber: how to design rubber components*, 3rd ed. Munich ; Cincinnati: Hanser Publishers, 2012.

[25] Griffith, A. A., 'VI. The phenomena of rupture and flow in solids', *Philosophical Transactions of the Royal Society of London. Series A, Containing Papers of a Mathematical or Physical Character*, vol. 221, no. 582-593, pp. 163–198, 1921.

[26] Rivlin, R. S. and Thomas, A. G., 'Rupture of rubber. I. Characteristic energy for tearing', *Journal of Polymer Science*, vol. 10, no. 3, pp. 291–318, 1953.

[27] Irwin, G. R., 'Analysis of Stresses and Strains Near the End of a Crack Traversing a Plate', *Journal of Applied Mechanics*, vol. 24, no. 3, pp. 361–364, 1957.

[28] Rice, J. R., 'A Path Independent Integral and the Approximate Analysis of Strain Concentration by Notches and Cracks', *Journal of Applied Mechanics*, vol. 35, no. 2, pp. 379–386, 1968.

[29] Eshelby, J. D., 'The force on an elastic singularity', *Philosophical Transactions of the Royal Society of London. Series A, Mathematical and Physical Sciences*, vol. 244, no. 877, pp. 87–112, 1951.

[30] Sun, X. and Davidson, B. D., 'Numerical evaluation of the effects of friction and geometric nonlinearities on the energy release rate in three- and four-point bend end-notched flexure tests', *Engineering Fracture Mechanics*, vol. 73, no. 10, pp. 1343–1361, 2006.

[31] Brouzoulis, J., Larsson, F. and Runesson, K., 'Strategies for planar crack propagation based on the concept of material forces', *Computational Mechanics*, vol. 47, no. 3, pp. 295–304, 2011.

[32] Hellen, T. K., 'On the method of virtual crack extensions', *International Journal for Numerical Methods in Engineering*, vol. 9, no. 1, pp. 187–207, 1975.

[33] He, M.-Y. and Hutchinson, J. W., 'Kinking of a Crack Out of an Interface', *Journal of Applied Mechanics*, vol. 56, no. 2, pp. 270–278, 1989.

[34] Oneida, E., Meulen, M. van der and Ingraffea, A., 'Method for calculating G, GI, and GII to simulate crack growth in 2D, multiple-material structures', *Engineering Fracture Mechanics*, vol. 140, pp. 106–126, 2015.

[35] Evans, A. G., Rühle, M., Dalgleish, B. J. and Charalambides, P. G., 'The fracture energy of bimaterial interfaces', *Metallurgical Transactions A*, vol. 21, no. 9, pp. 2419–2429, 1990.

[36] Cartraud, P. and Messager, T., 'Computational homogenization of periodic beam-like structures', *International Journal of Solids and Structures*, vol. 43, no. 3-4, pp. 686–696, 2006.

[37] Ingraffea, A. R. and Grigoriu, M., 'Probabilistic fracture mechanics: A validation of predictive capability', Cornell Univ Ithaca Ny Dept OF Structural Engineering, Tech. Rep., 1990, p. 155.

6 Publications

This section contains the publications prepared during the Ph.D. study. A numbered list with the processing status is given in Tab. 6.1. The contribution of the Ph.D. candidate for the key activities during the creation process are listed in Tab. 6.2 for each publication.

Table 6.1: List of Publications.

paper	bibliography	status
A	Frankl, S. M., Pletz, M., Wondracek, A. and Schuecker, C., 'Assessing Failure in Steel Cable-Reinforced Rubber Belts Using Multi-Scale FEM Modelling', *Journal of Composites Science*, vol. 6, no. 2, p. 34, 2022	published
B	Pletz, M., Frankl, S. M. and Schuecker, C., 'Efficient Finite Element Modeling of Steel Cables in Reinforced Rubber', *Journal of Composites Science*, vol. 6, no. 6, p. 152, 2022	published
C	Frankl, S., Pletz, M. and Schuecker, C., 'Incremental finite element delamination model for fibre pull-out tests of elastomer-matrix composites', *Procedia Structural Integrity*, vol. 17, pp. 51–57, 2019	published
D	Frankl, S. M., Pletz, M. and Schuecker, C., 'Improved concept for iterative crack propagation using configurational forces for targeted angle correction', *Engineering Fracture Mechanics*, vol. 266, p. 108 403, 2022	published

Table 6.2: The contribution of the Ph.D. candidate to the publications.

Activity	Paper A	Paper B	Paper C	Paper D
Conceptualisation	60 %	40 %	60 %	60 %
Method development & implementation	100 %	20 %	100 %	100 %
Numerical study	80 %	30 %	80 %	80 %
Writing - Original Draft	80 %	20 %	80 %	80 %
Writing - Review and Editing	0 %	60 %	0 %	0 %

Paper A

Assessing Failure in Steel Cable-Reinforced Rubber Belts Using Multi-Scale FEM Modelling

Authors: Frankl, Siegfried Martin
Pletz, Martin
Wondracek, Alfred
Schuecker, Clara

Journal of Composites Science
DOI: 10.3390/jcs6020034

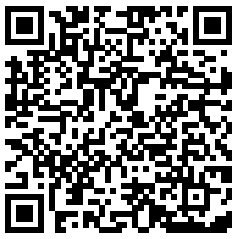

Journal of
Composites Science

MDPI

Article

Assessing Failure in Steel Cable-Reinforced Rubber Belts Using Multi-Scale FEM Modelling

Siegfried Martin Frankl [1], Martin Pletz [1,*], Alfred Wondracek [2] and Clara Schuecker [1]

[1] Designing Plastics and Composite Materials, Department of Polymer Engineering and Science, Montanuniversitaet Leoben, 8700 Leoben, Austria; siegfried.frankl@unileoben.ac.at (S.M.F.); clara.schuecker@unileoben.ac.at (C.S.)
[2] Semperit Technische Produkte Gesellschaft m.b.H., 2632 Wimpassing, Austria; alfred.wondracek@semperitgroup.com
* Correspondence: martin.pletz@unileoben.ac.at

Abstract: This work introduces a finite element model of a steel cable-reinforced conveyor belt to accurately compute stresses in the splice. In the modelled test rig, the belt runs on two drums and is loaded with a cyclic longitudinal force. An explicit solver is used to efficiently handle the high number of elements and contact conditions. This, however, introduces some issues of dynamics in the model, which are subsequently solved: (a) the longitudinal load is applied with a smooth curve and damping is introduced in the beginning of the simulation, (b) residual stresses are applied in regions of the belt that are initially bent around the drums, and (c) supporting drums are introduced at the start of the simulation to hinder oscillations of the belt at low applied forces. To accurately capture the tensile and bending stiffness of the cables, they are modelled by a combination of solid and beam elements. The results show that numerical artefacts can be reduced to an acceptable extent. In the region of highest stresses, the displacements are additionally mapped onto a submodel with a smaller mesh size. The results show that, for the investigated belt, the local maximum principal stresses significantly increase when this region of highest stresses comes into contact with, and is bent by, the drum. Therefore, it is essential to also consider the belt's bending to predict failure in such applications.

Keywords: Finite Element Method; conveyor belts; steel cables; submodelling

Citation: Frankl, S.M.; Pletz, M.; Wondracek, A.; Schuecker, C. Assessing Failure in Steel Cable-Reinforced Rubber Belts Using Multi-Scale FEM Modelling. *J. Compos. Sci.* **2022**, *6*, 34. https://doi.org/10.3390/jcs6020034

Academic Editor: Francesco Tornabene

Received: 22 December 2021
Accepted: 18 January 2022
Published: 20 January 2022

1. Introduction

Conveyor belts are used in a wide range of applications such as supermarkets, logistic centres, and mining. The conveyor belts in mining are reinforced with steel cables to reach the high strengths required. Such conveyor belts can have lengths of several kilometres. They consist of belt segments that are connected on site. In this connection, which is called splice, the steel cables are arranged in a specific laying scheme. The strength of this splice limits the belt's strength in cyclic loading and is thus of great interest to engineers. The splice strength is experimentally determined in a test rig where a conveyor belt with one splice runs on two drums and is cyclically loaded [1], see Figure 1. The failure of the belt can be caused by cable–rubber debonding, tearing of the rubber, and the rupture of cables.

To certify a belt for a tensile force, a certain number of cycles must be reached in the test rig without failure. To better understand the failure mechanisms, some effort has been put into monitoring the evolution of damage during the test [2,3]. This could be an initial debonding of cables from the rubber, which, at higher cycle numbers, leads to the rupture of individual cables, which ultimately leads to failure of the belt. The large variety of belt damage mechanisms has been illustrated in a study of damage due to objects such as rocks falling on a conveyor belt [4]. This complex damage behaviour indicates that it is not trivial to predict this failure which depends on the cable and rubber properties, the splice

geometry, and the debonding strength of the cable–rubber interface [5]. For conveyor belts of lower strength classes, which are reinforced with textiles, Finite Element Method (FEM) models that compute the stress-distribution in belts that are loaded in tension exist [6,7]. The steel cables, on the other hand, pose a challenge in such models due to their complex stiffness: steel cables have high tensile stiffness but very low bending stiffness, and can feature tension/torsion coupling [8]. This can play a role in the failure of splices.

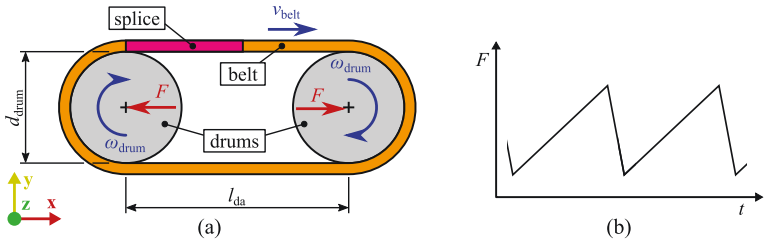

Figure 1. Belt test rig to determine the cyclic strength of a belt splice following [1]: (**a**) Setup of the test rig and (**b**) applied load curve.

Various research groups have developed numerical models to predict the strength of a splice, putting the emphasis on different aspects of the complex conveyor belt system. Nordell et al. [9,10] presented a very detailed FEM model of a splice, which even accounts for the tension/torsion coupling of cables. Similar to Keller [11], they argued that simpler specimens can be designed to show damage behaviour similar to that observed in the belt splice, which can then be used to study the damage behaviour in detail, where the influence of belt-drum contact and bending was also discussed. Another research group introduced similar FEM models to study a range of rubber materials and introduce an automated tool for investigating splice schemes [12,13]. In more recent work, other groups such as Li et al. [14] and Wheatley and Keipour [15] presented similar models, focusing on simplified specimens loaded in tension. None of those models account for bending of the belt on the drums in the test rig. Usually, the splice optimisation is carried out according to evaluated stresses in the FEM models. The bending of the belt, however, can affect the local stress fields in the splice in a nonlinear way. This can shift the damage mechanisms compared to a belt loaded purely in tension.

This work introduces a conveyor belt test rig model that fully accounts for contact and bending of the belt on the two drums. The computed stress fields can be used as an indicator of the belt's strength (Li et al. [16] use a stress-based criterion for damage initiation that agrees well with experimental results of failure). It can, thus, predict the influence of bending on the tested strength of a belt. Note that this work computes static stresses and could be extended towards fatigue models that are based on those stresses, as described by Carraro et al. [17] and Ferdous et al. [18]. Since all steel cables of a belt need to be modelled to capture the stress variations in the splice, a full 3-d model including drums contact is very challenging in terms of computational time. For this reason, a two-scale approach using an explicit full-scale test rig model and a finer-meshed implicit submodel of the region of highest stresses is taken. The models are used to assess whether the bending of the belt at the drums introduces additional stresses in the splice. This work, which is the first full 3-d splice model with bending, can thus answer the question of whether the bending loads are relevant for the mechanical design of conveyor belts. Challenges such as obtaining an initial state of movement and stresses in the belt and coping with initial dynamic artefacts are solved in the explicit model.

2. Methods

In this section, the modelling of the conveyor belt setup and the splice scheme used are explained. Additionally, the setup of the global test rig model and the submodel is presented. The belt is stress-free and flat after production. In the global test rig model, the

initially-bent regions are applied with residual stresses. Furthermore, specific techniques are described to avoid unwanted dynamic effects in the explicit global test rig model.

2.1. Material Models and Splice Geometry

This work uses a simple conveyor belt with nine cables and only one rubber material. This belt, which can be simulated much faster, can be assumed to feature similar effects of the bending to realistic belts. The setup of a conveyor belt is shown in Figure 2a with the longitudinal direction, the out-of plane direction, and the lateral direction, defined as x, y, and z-directions, respectively. Such a steel cable-reinforced conveyor belt can consist of several reinforced and non-reinforced rubber layers. The belt considered in this work is made up of only one rubber material reinforced by parallel steel cables and no additional transverse reinforcement, see Figure 2b. The belt has a total thickness of $h = 42.5\,\text{mm}$ with $h_1 = 16.75\,\text{mm}$ and $h_2 = 25.75\,\text{mm}$. The rubber is modelled as a hyper-elastic material using the Mooney-Rivlin formulation. The strain energy function is given by

$$U = C_{10}(I_1 - 3) + C_{01}(I_2 - 3) + \frac{1}{D}(J - 1)^2, \tag{1}$$

where C_{10}, C_{01}, and D are material parameters, and I_1 and I_2 are the first and second invariant of the left Cauchy—Green deformation tensor, respectively. J is the determinant of the deformation gradient. The material parameters are listed in Table 1. The parameters C_{10} and C_{01} are taken from Froböse et al. [12] for a rubber material with a shear modulus of $G = 1.7\,\text{MPa}$. The rubber density is not given and is assumed as $\rho_{\text{rubber}} = 1000\,\text{kg/m}^3$. To use a typical Poisson's ratio for rubber of ν very close to 0.5 would introduce high-frequency noise in the explicit simulation, as described in [19], suggesting an upper limit of $\nu = 0.495$. Therefore, the parameter D is set to reach a Poisson's ratio of $\nu = 0.485$.

Table 1. Material parameters.

C_{10} [MPa]	C_{01} [MPa]	D [1/MPa]
0.7083	0.1417	0.03565

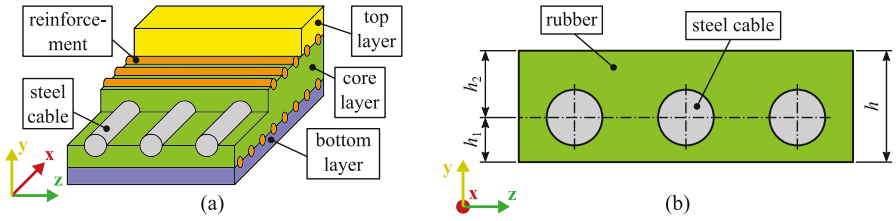

Figure 2. General structure of a conveyor belt with possible rubber layers and reinforcements (**a**) and cross-section of the conveyor belt used in this work (**b**).

Due to their inherent structure, the steel cables cannot be modelled accurately by a simple solid material model. Steel cables feature high tensile stiffness and low bending stiffness compared to a solid material of the same diameter. Also, they can feature a tension/torsion coupling, which requires special modelling in FEM. In this work, the steel cables are modelled so that they reach accurate tensile and bending stiffness. To this end, the volume of the cylindrical steel cables is meshed with solid elements and, in the cable's axis, additional beam elements are introduced. This setup is illustrated in Figure 3. The mechanical response is assumed to be linear elastic. The beam elements share nodes with the solid elements. It should be mentioned that the volume elements are not affected by the rotations of their connected nodes. The steel cables in this work have a radius of $r_{\text{cable}} = 6.75\,\text{mm}$.

A very small radius of the beam is chosen so that the solid elements account for the whole bending stiffness of the cable. To determine the Young's modulus for the solid

elements E_{solid}, a three-point-bending test of a rubberised steel cable with a bending length $l_{\text{bend}} = 110\,\text{mm}$ has been performed. From the linear region at the beginning of the force-displacement curve, a bending stiffness $S_{\text{bend}} = 95\,\frac{\text{N}}{\text{mm}}$ is obtained and yields a Young's modulus for the solid elements as

$$E_{\text{solid}} = \frac{S_{\text{bend}}\, l_{\text{bend}}^3}{12\, r_{\text{cable}}^4\, \pi} = 1615.68\,\text{MPa}. \tag{2}$$

To determine the average Young's modulus of the cable, a tensile test of a single cable with a test length of $l_{\text{tensile}} = 200\,\text{mm}$ has been performed. A tensile stiffness $s_{\text{tensile}} = 25\,\text{kN/mm}$ is obtained from the linear region at the beginning of the force-displacement curve and yields a Young's modulus for the cable:

$$E_{\text{cable}} = \frac{s_{\text{tensile}}\, l_{\text{tensile}}}{r_{\text{vol}}^2\, \pi} = 34{,}931.13\,\text{MPa}. \tag{3}$$

In order to not induce any additional bending stiffness by the beam, the area ratio of the solid and the beam cross-sections is set to $\xi_{\text{volbeam}} = 1000$. This results in a beam radius of $r_{\text{beam}} = 0.214\,\text{mm}$. The Young's modulus of the beam E_{beam} needs to be adjusted to reach the total cable stiffness by the combination of the beam and solid elements. Therefore, E_{beam} has to account for the tensile stiffness that has not been accounted for by the solid elements as

$$E_{\text{beam}} = \xi_{\text{volbeam}}(E_{\text{cable}} - E_{\text{solid}}) = 33{,}300\,\text{GPa}. \tag{4}$$

The density of the steel cable ρ_{cable} is computed from the density of the rubber ρ_{rubber}, the density of steel $\rho_{\text{steel}} = 7850\,\text{kg/m}^3$, and an assumed volume ratio of steel in the rubberised cables $\xi_{\text{st}} = 0.6$. Therefore, the density of the steel cable is given by

$$\rho_{\text{cable}} = \xi_{\text{st}}\,\rho_{\text{steel}} + (1 - \xi_{\text{st}})\rho_{\text{rubber}} = 5110\,\frac{\text{kg}}{\text{m}^3}. \tag{5}$$

The Poisson's ratio of the solid and the beam elements is assumed to be 0.3.

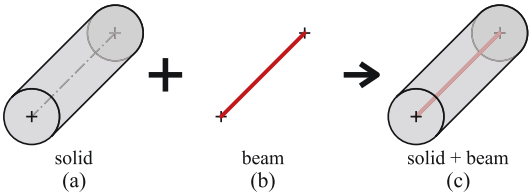

Figure 3. Steel cable modelling: (**a**) Solid elements that account for bending stiffness, (**b**) beam elements that account for tensile stiffness, and (**c**) the combination of solid and beam elements.

The splice scheme used for the splice is shown in Figure 4 and the corresponding parameters of the splice are listed in Table 2. Outside the splice, the steel cables are arranged in parallel with an equal distance between the cable axes of s_{belt}. Within the splice, the steel cables are rearranged to a lateral distance between the cables of s_{splice}. Cubic splines are used to describe the lateral change in the steel cable axes between outer regions and the splice.

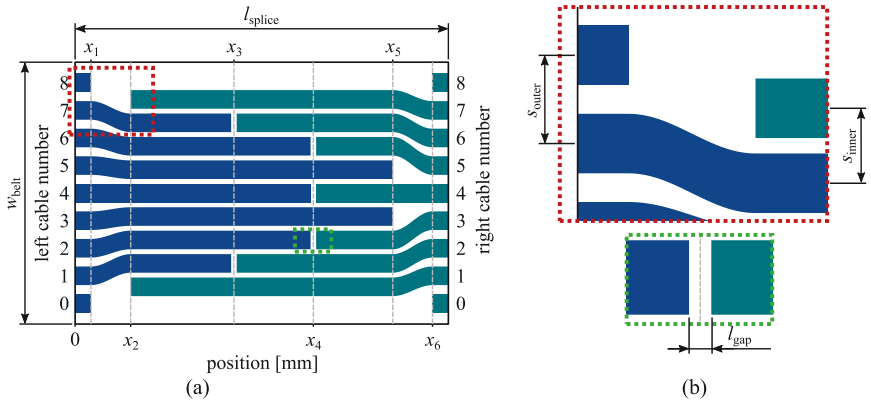

Figure 4. Geometry of the splice: (**a**) full view of the splice and (**b**) closer view of one part of the splice. Note that the lateral cable distance is smaller within the splice compared to outside the splice.

Table 2. Parameters of the splice.

Parameter Name	Symbol	Value	Unit
belt width	w_{belt}	190	mm
splice length	l_{splice}	4.7	m
cable positions	x_i	0.2, 0.7, 2, 3, 4, 4.5	m
outer steel cable spacing	s_{belt}	20	mm
inner steel cable spacing	s_{splice}	17	mm
gap between cable ends	l_{gap}	70	mm

2.2. Test Rig Model

In this section, the global FEM model of the conveyor belt test rig is described. In the test rig [1], the belt is cyclically loaded in tension as it is running on the drums. This work considers the quasi-static case of the conveyor belt running around the drums with a constant applied load F. For reasons of efficiency, an explicit solver is used. This means that dynamic effects in the model are considered as artefacts and have to be reduced to a small extent. To be able to start the simulation with a belt running on the two drums, the bending stresses of the belt on the drums have to be considered. This is reached by the application of residual stresses. Additionally, the application of the load is optimised and additional drums are introduced that avoid belt oscillations in the beginning of the simulation. The model is used to determine stress and strain fields for the conveyor belt running in the test rig. The validity for the quasi-static case is examined. The region of highest stresses in the belt running around the drum is determined and investigated further in a submodel.

2.2.1. Model Setup

The conveyor belt test rig shown in Figure 1 is represented as a quasi-static FEM model. The belt geometry, splice scheme, and materials of the model are taken from above. The left end of the splice is initially positioned right above the centre of the left drum. All model parameters are listed in Table 3. To handle the non-linearities in the material, the contact between the belt and drums and a high number of elements, an explicit solver is used, which is much more efficient for such models. Velocities in the model, thus, have no physical meaning and dynamic effects are considered as artefacts.

The drums are modelled as rigid discrete surfaces with reference points in each of their axes. In the x- and y-axes, the drum's rotation is fixed. The displacement of the drum's reference points is also constrained in y- and in the z-direction. An additional reference point P for applying the tensile load of the belt F is introduced, see Figure 5a. The reference

point P is coupled to the reference points of the left drums P_{ld} and right drum P_{rd} in the x-direction:

$$\begin{aligned} u_x + \eta_c\, u_{ldx} &= 0 \text{ and} \\ u_x - \eta_c\, u_{rdx} &= 0, \end{aligned} \tag{6}$$

with u_x as the displacement of P, u_{ldx} as the displacement of P_{ld}, u_{rdx} as the displacement of P_{rd}, and η_c as the weight factor for the coupling. Since F should be applied in the belt, the weight factor for the coupling is set to $\eta_c = 4$. The contact between the drums and the belt is modelled with penalty contact. The friction coefficient between rubber and steel μ_{rs} for the dry condition is between 0.6 to 1.1 according to Cruz Gómez et al. [20]. Therefore, $\mu_{rs} = 0.8$ is assumed.

Table 3. Parameters of the test rig.

Parameter Name	Symbol	Value	Unit
distance of the drum axes	l_{da}	7	m
diameter of the drums	d_{drum}	1.25	m
velocity of the belt Equation (7)	v_{belt}	6.454	m/s
number of circulations per load cycle [1]	n_{cplc}	18	1
time period of one load cycle [1]	t_{lc}	50	s
angular velocity of the drums Equation (8)	ω_{drum}	9.987	rad/s
point mass of the drum Equation (9)	m_{drum}	1502	kg
moment of inertia of the drums Equation (10)	$I_{z\,drum}$	429	kg m^2
tensile load in the belt Equation (12)	F_{belt}	655.2	kN

The explicit simulation starts with a running belt with the initial velocity of the belt v_{belt}, which can be calculated from the number of circulations per tensile load cycle n_{cplc} and the time period of one load cycle t_{lc}, as defined in [1]:

$$v_{belt} = \frac{n_{cplc}(d_d\,\pi + 2\,l_{da})}{t_{lc}}. \tag{7}$$

Note that this means that the belt is running with the actual speed stated in Table 3, even though the model is developed for a quasi-static analysis. The angular velocity of the drums ω_{drum} that corresponds to the belt speed calculates as

$$\omega_{drum} = \frac{2\,v_{belt}}{d_{drum} + h}, \tag{8}$$

where the neutral axis is assumed to be in the middle of the belt thickness. Since the right drum is the driving drum, this angular velocity is applied to the right drum continuously throughout the simulation and to the left drum as an initial condition only.

A point mass m_{drum} is applied at the reference points of the drums. For the mass, a hollow cylinder of steel with an external diameter of $d_{outer} = d_{drum}$, an internal diameter $d_{inner} = d_{drum} - 2 \cdot 200\,\text{mm}$, and a height of $h_{drum} = w_{belt} + 2 \cdot 50\,\text{mm}$ is assumed. The point mass m_{drum} is then given by

$$m_{drum} = \rho_{steel}\,\pi\,h_{drum}\frac{d_{outer}^2 - d_{inner}^2}{4}. \tag{9}$$

A moment of inertia $I_{z\,drum}$ for rotation in the drum axis is specified for the left drum, which is given for a hollow cylinder by

$$I_{z\,drum} = \frac{1}{2}\,m_{drum}\left(\frac{d_{outer}^2 + d_{inner}^2}{4}\right). \tag{10}$$

The tensile load F is applied smoothly enough and slowly enough so that dynamic effects do not alter the results and, therefore, the displacement caused by the load application increases smoothly. The tensile force on the belt is applied to point P in a way so that oscillations in the belt are minimised: it was discovered that starting with a force $F = F_{\text{belt}}/8$ at $t = 0$ and then using a polynomial with the smooth-step option of Abaqus to increase it to F_{belt} at $t = t_1$ works well, see Figure 5b. Additionally, the reference point P is connected to a damper in the x-direction, which has a damping coefficient d of 100 Ns/mm. The time t_1 is chosen such that the constant applied force is reached before the splice runs into the bent region on the drum:

$$t_1 = \frac{l_{\text{da}} - l_{\text{splice}}}{v_{\text{belt}}} = 0.3564\,\text{s}. \tag{11}$$

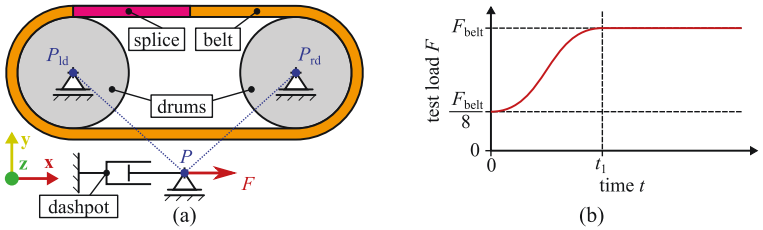

Figure 5. Setup of the conveyor belt test rig model (**a**) and applied test load vs. time curve (**b**).

The applied load is selected to be 60% of the nominal strength per width k_{N} of 7.8 $\frac{\text{kN}}{\text{mm}}$ of such a steel cable-reinforced belt. The width in the nominal strength is taken as the number of cables in the splice n_{sc} (here $n_{\text{sc}} = 7$) times their distance s_{belt}. The force F_{belt} thus calculates as

$$F_{\text{belt}} = 0.6\, n_{\text{sc}}\, s_{\text{belt}}\, k_{\text{N}}. \tag{12}$$

The belt is meshed with a global mesh size of 3 mm. Four elements are used over the gap length of the rubber gaps between cables. Outside the splice region, a mesh size of 10 mm is used along the running direction of the belt. To avoid hour glassing, eight-noded fully-integrated hexahedral elements are used for the volume except for the regions near the steel cable ends, where it is not possible to mesh this geometry change using purely hexahedral elements. Thus, those regions are meshed using six-noded wedge elements with reduced integration and four-noded tetrahedral elements. The beams of the steel cables are modelled using two-noded Thimoshenko beam elements. The cables and the rubber are perfectly connected (shared nodes), except for the end faces of the cables, where an initial debonding is assumed. This is because the necessary surface modification of the steel cables to increase the adhesion to the rubber is not present at the ends that have been cut. The drums are meshed with a global mesh size of 10 mm and four-noded rigid quad elements.

To solve the model, the nonlinear explicit solver of the commercial FEM code Abaqus [19] is used where large deformations are considered. A simulation time of 0.80638 s is sufficient for about 60% of the splice running into the bent region of the drum, and the region of highest stresses is located in the middle of the bent region. Mass scaling is used to achieve a stable time increment of $\Delta t = 1.75 \cdot 10^{-6}$ s with a total change in the model's mass of 4.46%. The test rig model has a total of about 3,250,000 elements and takes 92 h to run on 72 cores.

2.2.2. Applying Initial Stresses in Bent Belt Regions

Whenever the conveyor belt is bent, it contains some bending stresses in the cables and the rubber regions. In FEM models, the geometry is usually considered stress-free at the start of the computation. For the regions of the belt that are initially not straight but are bent around the drums, the stresses that correspond to bending with a curvature of $2/d_{\text{drum}}$ need to be applied as initial stresses. Since the bending stress in a cable-reinforced rubber belt is

not trivial, a small implicit simulation is carried out to obtain those stresses. This model contains the belt in its bent shape and straightens it, where the bent shape corresponds to the shape it will initially have in the test rig model (see Figure 6a,b). The stresses in the cable direction are evaluated and their inverse values are applied element-wise in the initial step of the test rig model. It has been verified that this procedure yields an approximately stress-free state in the segment, see Figure 6c,d.

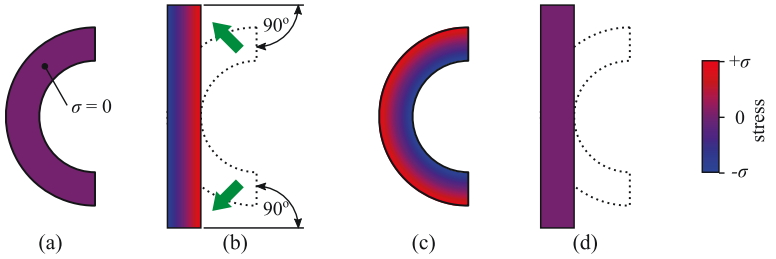

Figure 6. Procedure to determine and apply the residual stresses in the initially bent regions: (**a**) bent belt, (**b**) straightened belt and resulting stress distribution, (**c**) bent belt with applied residual stresses, and (**d**) approximately stress-free belt after straightening.

2.2.3. Avoiding Belt Oscillations Using Support Drums

Due to the internal stresses in the initially bent regions, the belt tends to deform as shown in Figure 7a, particularly if only low tensile forces are applied to the drums. In a dynamic model, this induces initial oscillations. To avoid such oscillations, additional support drums are used, but only during the first phase until the final loading state is reached, see Figure 7b. Note that these drums are only introduced to avoid numerical artefacts and are not part of the test rig. The horizontal distance of the support drum axes l_{sda} is set to 6.8 m, therefore they lie 100 mm closer together than the test rig drums. The diameter of the support drums is the same as the test rig drums, and the vertical distance of the support drum axes w_{sda} is set to 2.585 m. The support drums initially have the same angular velocity ω_{drum} as the test rig drums; however, their rotational velocity is free to change during the simulation. Apart from rotation around the z-axis, where an inertia of $I_{\mathrm{z\,drum}}$ is applied as in the left drum of the test rig, all translations and rotations of the drums are constrained. The support drums use the same mesh and contact conditions to the belt as the test rig drums. Once the maximum applied load is reached at t_1, their contact condition between the support drums and belt is switched off in order to effectively remove them from the simulation.

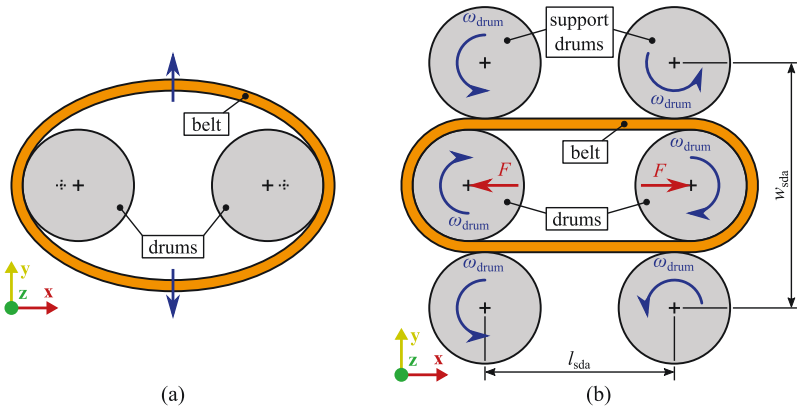

Figure 7. To avoid oscillations with belt deformations schematically shown in (**a**), four support drums are introduced (**b**).

2.3. Submodel

In this work, the region with the highest stresses in the rubber is modelled in the submodel with a finer mesh to investigate this region in more detail. This region is defined in Figure 8, where the same belt geometry and the same material models as the test rig model are used. The submodel length l_{sub} and the submodel width w_{sub} are set to 135 mm and 51.5 mm, respectively. The displacements of the test rig model are mapped to the lateral surfaces and the bottom surface of the submodel, see Figure 8. The displacements are mapped separately for the steel cable and the rubber nodes. The nodes at the steel cable/rubber interface use the displacement field of the cable elements in the global model. To avoid convergence issues, the rotational degree of freedom around the beam axes of the beam nodes belonging to the left lateral surface is fixed.

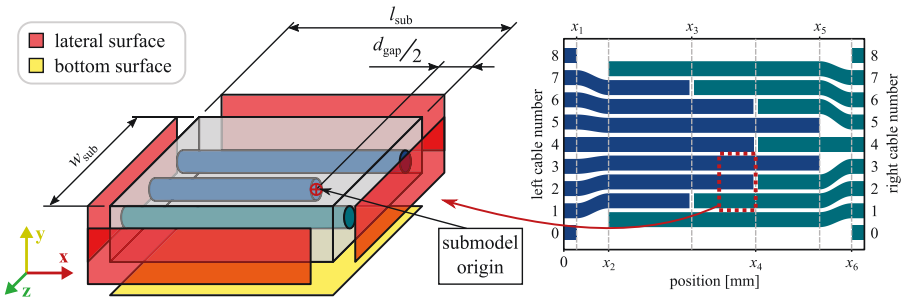

Figure 8. Sketch of the submodel, which is located in the splice. Additionally, the surfaces are defined for boundary conditions.

The submodel uses eight-noded fully-integrated hybrid hexahedral elements and is meshed with a global mesh size of 1.5 mm. Eight elements are used in the rubber gap between the steel cables. The beams of the steel cables are modelled using two-noded Timoshenko beam elements, as in the global model. For computation, the nonlinear implicit solver of the commercial FEM code Abaqus [19] is used, considering large deformations. For verification of the submodelling approach, the stresses of the global model and the submodel are compared to see if the submodelling approach is valid for that case.

3. Results and Discussion

Before showing the results of the test rig model and the submodel, this section starts with an evaluation of the test rig model. It is discussed whether the strategies for avoiding dynamic artefacts have been successful in reaching a quasi-static loading in the model. Figure 9a shows the force applied to point P in the x-direction as well as the computed velocity and displacement at this point as a function of simulation time. After reaching a constant force ($t > 0.3564$ s), a small delay occurs before reaching a displacement plateau. Therefore, the used values for damping and applying the initial tensile force, as well as the used support drums, yield accurate steady-state stress fields for $t > 0.48$ s, where the deviation from the maximum value $u_{max} = 327.5$ mm is less than 1.5%. The residual stresses remaining after straightening the initially bent belt are shown in Figure 9b. Only slight artefacts are visible in the stresses, which confirms that the residual stresses have been applied in a valid manner. The increased stresses in the bent region for $t = 0.05$ s compared to $t = 0$ s occur due to the applied loading at this time in the simulation.

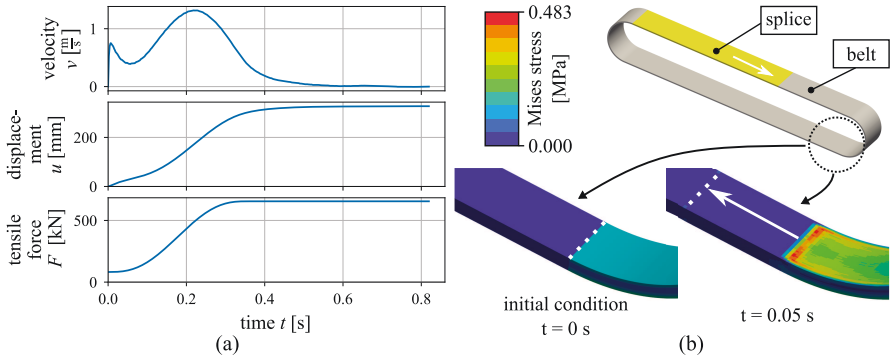

Figure 9. (**a**) Evolution of velocity, displacement, and tensile force in the x-direction of the reference point P and (**b**) validation of the applied residual stress in the initially bent regions of the conveyor belt.

The results of the global model for $t = 0.806$ s are shown in Figure 10. The maximum principal stress σ_I is plotted for the plane of the steel cable centre axes in Figure 10a, where σ_I is computed at the element centre. A small schema shows the position of the splice at the time of the stress evaluation. The highest maximum principal stress $\sigma_{\mathrm{I}\,\max}$ occurs at the cable end of the third and seventh cable from the left-hand side, counted from the bottom. These regions feature $\sigma_{\mathrm{I}\,\max}$ in all time steps. One of these regions is plotted in more detail and is indicated by a red frame. This region's stress field is plotted for $t = 0.556$ s, when it lies in the flat part of the test rig, in Figure 10b. The $\sigma_{\mathrm{I}\,\max}$ occur at the cable end since, in the model, the cable end face is detached from the rubber. This means that, at the front surface, all nodes except the outer nodes are duplicated. Here, $\sigma_{\mathrm{I}\,\max}$ occurs at the bottom of the cable due to shear load between a cable from the left and the right-hand side of the splice. The influence of bending at the drums can be seen in Figure 10c, where the same region is plotted for $t = 0.806$ s, where it lies in the bent region of the belt. In the flat and in the bent region $\sigma_{\mathrm{I}\,\max}$, values of 38.9 MPa and 45.7 MPa are reached, respectively. This indicates that the bending of a belt in the test rig can have a significant influence on arising stresses and is not negligible. It is obvious that the mesh in Figure 10 only roughly approximates the stress field; therefore, a study with a finer mesh is relevant.

The results of the submodel are shown in Figure 11, where the same times and regions as in Figures 10b,c are plotted. Due to the finer-meshed submodel, the stress field can be approximated better and the σ_I are higher. For the flat and the bent region $\sigma_{\mathrm{I}\,\max}$, values of 61.0 MPa and 69.7 MPa are obtained, respectively. In the submodel, the σ_I values at locations which are not close to the stress concentrations at the cable ends are similar to the σ_I values in the global model. This indicates the validity of this submodel.

The $\sigma_{\mathrm{I}\,\max}$ results of the global model and submodel are plotted over time in Figure 12. For $t < 0.65$ s, the investigated region is located in the flat region, and for $t > 0.65$ s, the investigated region is located in the bent region of the test rig. The σ_I values in the belt in the bent case are higher than in the flat case by 17.5% and 14.3% in the global model and the submodel, respectively. For $t < 0.65$ s, first a pronounced increase in $\sigma_{\mathrm{I}\,\max}$ occurs due to bending, followed by a slight increase in both models. This slight increase at the end of the curve can be observed more clearly in the submodel.

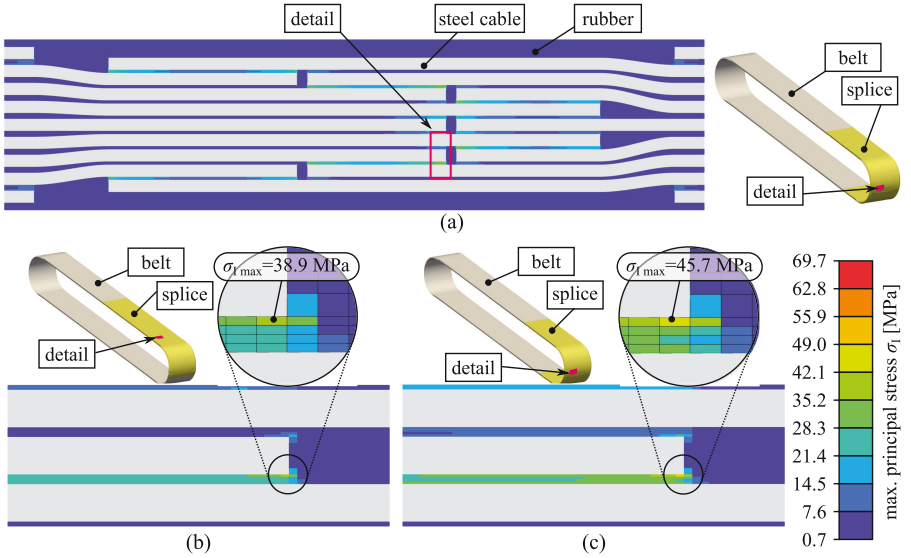

Figure 10. Stress results of the splice determined in the global model: (**a**) Top view of the splice with a general view where the splice location is shown, (**b**) detail of the splice for straight condition, and (**c**) detail for the splice for bent condition.

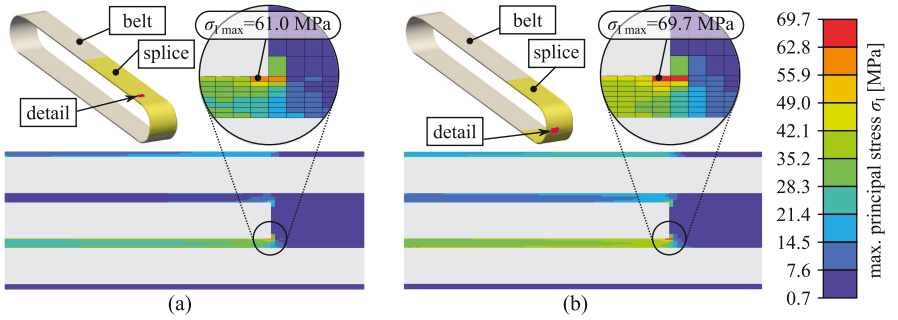

Figure 11. Stress results of the splice determined in the submodel: (**a**) Detail of the splice for straight condition, and (**b**) detail for the splice for bent condition.

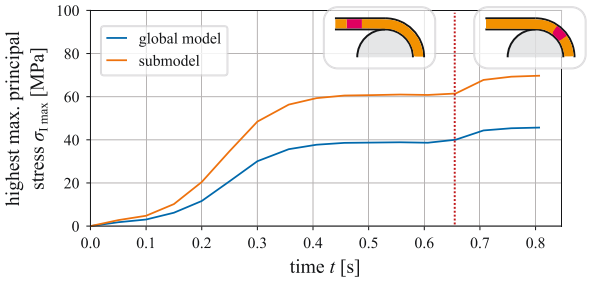

Figure 12. Time series of highest maximum principal stress values evaluated in the test rig model and the submodel. At $t = 0.65$ s, the point of highest stress runs into the bent region of the belt.

4. Conclusions

This work introduces a modelling approach using FEM to predict the stress and strain fields of a conveyor belt in a test rig, where the influence of the bending of the belt around the test rig drums is also considered. It is shown how a quasi-static loading can be achieved

for an explicit FEM-simulation using suitable modelling techniques such as smooth load application with damping and added support drums. A computational cost of 3.8 days using 72 CPUs on a cluster is obtained for the investigated seven-cable splice belt. This means that larger belts with more steel cables can also be computed in an acceptable time frame. Existing conveyor belt models from the literature only consider tensile loading of the belt, therefore one key question addressed in this work is how much the stresses are influenced by the bending. The test rig model and an additional submodel of the region of highest stresses show that

- The region of highest stresses in the used splice scheme occurs at two cable ends due to shear stresses to the neighbouring cables;
- The test rig model computes by 17.5% higher maximum principal stresses while the critical position of the splice is bent at the drums compared to in the flat region;
- The submodel, where eight instead of four elements are used between the steel cables, computes higher stresses than the global model. The maximum principal stresses reach 14.3% higher values in the bent region than in the flat region.

The developed modelling approach shows a significant influence of bending on the local rubber stresses in the used test rig setup. Therefore, the influence of bending is essential for further fatigue modelling, where accurate stress fields are required. The submodel illustrates how, at a smaller scale, more accurate fracture mechanic concepts such as damage criteria can be used. Other researchers and engineers can benefit from this work by seeing the significance of bending loads on splices and being presented with a modelling approach that can compute this.

Author Contributions: Conceptualization, S.M.F., M.P. and C.S.; methodology, S.M.F. and M.P.; software, S.M.F.; validation, S.M.F.; formal analysis, S.M.F.; investigation, S.M.F.; resources, S.M.F., M.P., A.W. and C.S.; data curation, S.M.F.; writing—original draft preparation, S.M.F. and M.P.; writing—review and editing, S.M.F., M.P., A.W. and C.S.; visualization, S.M.F.; supervision, C.S.; project administration, M.P. and A.W.; funding acquisition, C.S. and M.P. All authors have read and agreed to the published version of the manuscript.

Funding: This research was supported by the Austrian Research Promotion Agency (FFG) within the "BRIDGE" framework as part of the project "Entwicklung einer Methodik zur Vorhersage des Versagens in elastomeren Gurten mittels Finite Elemente Simulation", grant agreement 864702.

Data Availability Statement: The data presented in this study are available on request from the corresponding author. The data is not publicly available due to size of the FEM result files.

Conflicts of Interest: The authors declare no conflict of interest.

References

1. *DIN 22110-3:2015-04, Prüfverfahren für Fördergurtverbindungen_- Teil_3: Ermittlung der Zeitfestigkeit für Fördergurtverbindungen (Dynamisches Prüfverfahren)*; Technical Report; Beuth Verlag GmbH: Berlin, Germany, 2015 . [CrossRef]
2. Kirjanów-Błażej, A.; Jurdziak, L.; Burduk, R.; Błażej, R. Forecast of the remaining lifetime of steel cord conveyor belts based on regression methods in damage analysis identified by subsequent DiagBelt scans. *Eng. Fail. Anal.* **2019**, *100*, 119–126. [CrossRef]
3. Kozłowski, T.; Wodecki, J.; Zimroz, R.; Błażej, R.; Hardygóra, M. A Diagnostics of Conveyor Belt Splices. *Appl. Sci.* **2020**, *10*, 6259. [CrossRef]
4. Fedorko, G.; Molnar, V.; Marasova, D.; Grincova, A.; Dovica, M.; Zivcak, J.; Toth, T.; Husakova, N. Failure analysis of belt conveyor damage caused by the falling material. Part II: Application of computer metrotomography. *Eng. Fail. Anal.* **2013**, *34*, 431–442. [CrossRef]
5. Bonneric, M.; Aubin, V.; Durville, D. Finite element simulation of a steel cable -rubber composite under bending loading: Influence of rubber penetration on the stress distribution in wires. *Int. J. Solids Struct.* **2019**, *160*, 158–167. [CrossRef]
6. Heitzmann, P.; Froböse, T.; Wakatsuki, A.; Overmeyer, L. *Optimierung von Textil-Fördergurtverbindungen Mittels Finite Elemente Methode (FEM)*; Medium: application/pdf; Wissenschaftliche Gesellschaft für Technische Logistik, Rostock-Warnemünde: Chemnitz, Germany, 2016; Volume 2016. [CrossRef]
7. Bajda, M.; Błażej, R.; Hardygóra, M. Impact of Selected Parameters on the Fatigue Strength of Splices on Multiply Textile Conveyor Belts. *IOP Conf. Ser. Earth Environ. Sci.* **2016**, *44*, 052021. [CrossRef]
8. Costello, G.A. *Theory of Wire Rope*; Mechanical Engineering Series; Springer: New York, NY, USA, 1997. [CrossRef]

9. Nordell, L.; Qiu, X.; Sethi, V. Belt conveyor steel cord splice analysis using finite element methods. *Bulk Solids Handl.* **1991**, *11*, 863–868.
10. Nordell, L. Steel cord belt and splice construction: Modernizing their specifications, improving their economics. *Bulk Solids Handl.* **1993**, *13*, *685–693* .
11. Keller, M. Zur Optimierung Hochfester Stahlseilgurtverbindungen. Ph.D. Thesis, Universität Hannover, Hannover, Germany, 2001.
12. Froböse, T.; Heitzmann, P.; Overmeyer, L.; Wakatsuki, A. *Entwicklung eines FE-Modells zur Optimierung von Stahlseil-Fördergurtverbindungen*; Medium: Application/pdf; Wissenschaftliche Gesellschaft für Technische Logistik, Rostock-Warnemünde: Chemnitz, Germany, 2014; Volume 2014. [CrossRef]
13. Froböse, T. *Verfahren zur Ermittlung der Materialparameter für die Auslegung von Stahlseil-Fördergurtverbindungen mit Hilfe der FEM*; Number 2017, Band 01 in Berichte aus dem ITA; PZH Verlag: Hanover, Germany, 2017.
14. Li, X.; Long, X.; Shen, Z.; Miao, C. Analysis of Strength Factors of Steel Cord Conveyor Belt Splices Based on the FEM. *Adv. Mater. Sci. Eng.* **2019**, *2019*, 1–9. [CrossRef]
15. Wheatley, G.; Keipour, S. FEA of Conveyor Belt Splice Cord End Conditions. *UPB Sci. Bull. Ser. D Mech. Eng.* **2021**, *83, 205–216*.
16. Li, X.G.; Long, X.Y.; Jiang, H.Q.; Long, H.B. Finite element simulation and experimental verification of steel cord extraction of steel cord conveyor belt splice. In Proceedings of the IOP Conference Series: Materials Science and Engineering, Kitakyushu City, Japan, 10–13 April 2018; Volume 369, p. 012025. [CrossRef]
17. Carraro, P.; Maragoni, L.; Quaresimin, M. Prediction of the crack density evolution in multidirectional laminates under fatigue loadings. *Compos. Sci. Technol.* **2017**, *145*, 24–39. [CrossRef]
18. Ferdous, W.; Manalo, A.; Yu, P.; Salih, C.; Abousnina, R.; Heyer, T.; Schubel, P. Tensile Fatigue Behavior of Polyester and Vinyl Ester Based GFRP Laminates—A Comparative Evaluation. *Polymers* **2021**, *13*, 386. [CrossRef] [PubMed]
19. *ABAQUS Version 2020 User's Manual*; Dassault Systèmes Simulia Corp.: Providence, RI, USA, 2020.
20. Cruz Gómez, M.; Gallardo-Hernández, E.; Vite Torres, M.; Peña Bautista, A. Rubber steel friction in contaminated contacts. *Wear* **2013**, *302*, 1421–1425. [CrossRef]

Paper B

Efficient Finite Element Modeling of Steel Cables in Reinforced Rubber

Authors: Pletz, Martin
Frankl, Siegfried Martin
Schuecker, Clara

Journal of Composites Science
DOI: 10.3390/jcs6060152

Journal of
Composites Science

MDPI

Article

Efficient Finite Element Modeling of Steel Cables in Reinforced Rubber

Martin Pletz *, Siegfried Martin Frankl and Clara Schuecker

Designing Plastics and Composite Materials, Department of Polymer Engineering and Science, Montanuniversitaet Leoben, 8700 Leoben, Austria; siegfried.frankl@unileoben.ac.at (S.M.F.); clara.schuecker@unileoben.ac.at (C.S.)
* Correspondence: martin.pletz@unileoben.ac.at

Abstract: Spiral steel cables feature complex deformation behavior due to their wound geometry. In applications where the cables are used to reinforce rubber components, modeling the cables is not trivial, because the cable's outer surface must be connected to the surrounding rubber material. There are several options for modeling steel cables using beam and/or solid elements for the cable. So far, no study that lists and evaluates the performance of such approaches can be found in the literature. This work investigates such modeling options for a simple seven-wire strand that is regarded as a cable. The setup, parameter calibration, and implementation of the approaches are described. The accuracy of the obtained deformation behavior is assessed for a three-cable specimen using a reference model that features the full geometry of the wires in the three cables. It is shown that a beam approach with anisotropic beam material gives the most accurate stiffness results. The results of the three-cable specimen model indicate that such a complex cable model is quite relevant for the specimen's deformation. However, there is no single approach that is well suited for all applications. The beam with anisotropic material behavior is well suited if the necessary simplifications in modeling the cable–rubber interface can be accepted. The present work thus provides a guide not only for calibrating but also for selecting the cable-modeling approach. It is shown how such modeling approaches can be used in commercial FE software for applications such as conveyor belts.

Keywords: finite element modeling; homogenization methods; steel cables; steel-cable-reinforced rubber

Citation: Pletz, M.; Frankl, S.M.; Schuecker, C. Efficient Finite Element Modeling of Steel Cables in Reinforced Rubber. *J. Compos. Sci.* **2022**, *6*, 152. https://doi.org/10.3390/jcs6060152

Academic Editor: Stelios K. Georgantzinos

Received: 3 March 2022
Accepted: 20 May 2022
Published: 24 May 2022

1. Introduction

Steel cables are an indispensable part of the infrastructure and many engineering applications because they reliably provide high strengths with low bending stiffness. They consist of individual steel wires that are wound into strands, which in turn are wound to form the cable. Since cables consist of many parallel thin wires, their tensile stiffness is very high, whereas the bending and compressive stiffness are low. Because of this helical topology of spiral cables, there is a coupling of tensile deformation and torsional deformation of the cable (see Figure 1). Steel cables have many design options in terms of steel grade and cable geometry. Much work has been done on computing the influence of those parameters on the cable stiffness, accounting for the trajectories of the individual wires and contact between them. Many analytical and semi-analytical solutions have been developed and are listed in the review papers by Utting and Jones [1], Cardou and Jolicoeur [2], and the works of Costello [3] and Feyrer [4]. For standard cable types, good agreement of existing cable models with experiments can be reached. Effects like wire–wire friction can be captured. Hysteresis effects, the nonlinearity of the cable stiffness, and cable failure have been studied as well. Most of the work of such cable models is setting up the geometry, particularly for a non-straight cable; see Wang et al. [5]. Recently, the finite element method (FEM) has become widely used for modeling the mechanical response of cables: Jiang et al. [6] modeled a seven-wire strand using cyclic symmetry, and Foti and de Luca di

Roseto [7] investigated the elastic–plastic effects of the wires. Furthermore, FEM provides a basis for newly developed simplified models; see Chen et al. [8] and Cao and Wu [9].

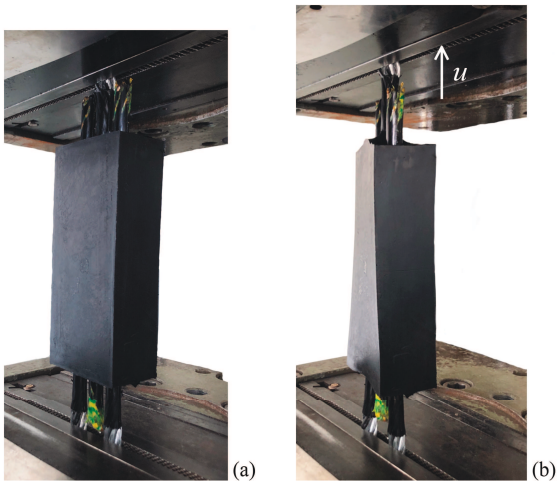

Figure 1. A three-cable specimen: (**a**) unloaded and (**b**) vertically loaded with a twist due to a tension/torsion coupling of the cables.

Many of the mathematical cable models refer to tests of a seven-wire strand reported by Utting and Jones [10], who reported a distinct tension/torsion coupling. When testing cables, the constraints of the cable ends influence the test results. The cable ends can be free, clamped, or even welded together. This effect of the cable ends was studied by Chen et al. [11] for thick cables, and they showed that in cable tests and FEM simulations of cables, much care must be put into applying the loads.

Modeling steel cables in reinforced rubber on the one hand requires capturing the influence of the rubber penetrating the cable (see Bonneric et al. [12]). On the other hand, the outer surface of the cable needs to be connected to the rubber. This interface between cable and rubber is crucial for the failure of cable-reinforced rubber components, as modeled by Frankl et al. [13].

Cable-reinforced rubber components can be conveyor belts, for example; see Nordell [14], Fedorko et al. [15], and Frankl et al. [16]. Obtaining the stiffness of cables that are used in rubber components requires tests on cables that have been penetrated by rubber (rubberized cables). How to separately capture tensile, bending, and torsion stiffness and the tension/torsion coupling of the cable that is embedded in rubber is a big challenge. Nordell et al. [17] stated that they developed a special element in the commercial FEM code ANSYS based on principles described by Costello [3], but did not give any details about this element.

In the present work, a variety of such cable modeling approaches is evaluated for their use in rubber components using the commercial FEM code Abaqus [18]. Those efficient modeling approaches use solid elements, beam elements, or a combination of both. In some of those modeling approaches, an anisotropic material model is used to mimic the tension/torsion coupling of the cable. To not have to deal with uncertainties of tests, the results of a fully modeled rubberized cable are taken as the reference to evaluate the accuracy of these modeling approaches. In this reference model, all wires and the surrounding rubber are modeled with a linear elastic and a hyperelastic material model, respectively. This model is called a full-geometry model, in contrast to the efficient models that account for wires and rubber in a way such that the overall cable stiffness is captured.

To keep the computational cost low, a seven-wire rubberized strand is used as the cable. For this cable, the homogenized stiffness matrix is computed from a full-geometry

J. Compos. Sci. **2022**, 6, 152 3 of 20

simulation similar to what was reported by Cartraud and Messager [19]. The various cable-modeling approaches are then calibrated and their ability to capture the homogenized stiffness components of the full-geometry model is evaluated. Then, the modeling approaches are evaluated in a simple rubber shear specimen containing three cables. The loads applied in these specimens are similar to those in conveyor belts; see Nordell et al. [17]. The full-geometry version of the three-cable specimen is used as a reference, and the stiffness, deformation, and strains in the specimen are used to assess the performance of the efficient models.

2. Methods

This section introduces the homogenized cable stiffness S_{ij} and a range of efficient modeling approaches that attempt to mimic this stiffness matrix S_{ij}. The cables are regarded as linear elastic throughout this study. For typical cable loads, this is a good approximation despite the nonlinear elastic response of the rubber. This section further describes the setup of the single-cable FEM model that computes the S_{ij} matrix for a seven-wire rubberized strand and is used to calibrate and evaluate efficient cable-modeling approaches. Additionally, a FEM model of a three-cable specimen is introduced, which is used to evaluate the performance of the efficient cable models.

2.1. Cable Stiffness

Figure 2 illustrates the loads (normal load F_x, twist moment M_x, and flexural moment M_b) and corresponding deformations (longitudinal strain ε_x, twist per length φ_x, and curvature κ) of a cable, which is drawn as a cylinder. Longitudinal shear deformation is not considered and the elastic bending response is considered to be independent of the bending direction.

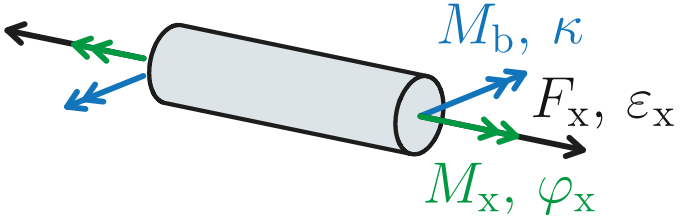

Figure 2. Definition of the loads and strains of a cable.

Since we regard small deformations, the stiffnesses in tension and compression and the stiffness for positive and negative twist are assumed to be the same. The elastic behavior of the cable can then be described by a stiffness matrix $\mathbf{S}$ (or S_{ij}) that couples the loads and deformations as

$$\begin{pmatrix} F_\mathrm{x} \\ M_\mathrm{x} \\ M_\mathrm{b} \end{pmatrix} = \begin{pmatrix} \frac{\partial F_\mathrm{x}}{\partial \varepsilon_\mathrm{x}} & \frac{\partial F_\mathrm{x}}{\partial \varphi_\mathrm{x}} & \frac{\partial F_\mathrm{x}}{\partial \kappa} \\ \frac{\partial M_\mathrm{x}}{\partial \varepsilon_\mathrm{x}} & \frac{\partial M_\mathrm{x}}{\partial \varphi_\mathrm{x}} & \frac{\partial M_\mathrm{x}}{\partial \kappa} \\ \frac{\partial M_\mathrm{b}}{\partial \varepsilon_\mathrm{x}} & \frac{\partial M_\mathrm{b}}{\partial \varphi_\mathrm{x}} & \frac{\partial M_\mathrm{b}}{\partial \kappa} \end{pmatrix} \begin{pmatrix} \varepsilon_x \\ \varphi_\mathrm{x} \\ \kappa \end{pmatrix} = \mathbf{S} \begin{pmatrix} \varepsilon_\mathrm{x} \\ \varphi_\mathrm{x} \\ \kappa \end{pmatrix} \tag{1}$$

with $\mathbf{S}$ defined as

$$\mathbf{S} = \begin{pmatrix} S_{\mathrm{xx}} & S_{\mathrm{x}\varphi} & S_{\mathrm{xb}} \\ S_{\varphi\mathrm{x}} & S_{\varphi\varphi} & S_{\varphi\mathrm{b}} \\ S_{\mathrm{bx}} & S_{\mathrm{b}\varphi} & S_{\mathrm{bb}} \end{pmatrix} \tag{2}$$

Inverting the stiffness matrix **S** yields the compliance matrix **C** (or C_{ij}). Similar to the definition of Young's modulus, we define stiffness parameters of the cable E_{xx}, $E_{x\varphi}$, ..., which correspond to the inverse of the components of **C**:

$$\begin{pmatrix} \varepsilon_x \\ \varphi_x \\ \kappa \end{pmatrix} = \mathbf{S}^{-1} \begin{pmatrix} F_x \\ M_x \\ M_b \end{pmatrix} = \begin{pmatrix} \frac{1}{E_{xx}} & \frac{1}{E_{x\varphi}} & \frac{1}{E_{xb}} \\ \frac{1}{E_{\varphi x}} & \frac{1}{E_{\varphi\varphi}} & \frac{1}{E_{\varphi b}} \\ \frac{1}{E_{bx}} & \frac{1}{E_{b\varphi}} & \frac{1}{E_{bb}} \end{pmatrix} \begin{pmatrix} F_x \\ M_x \\ M_b \end{pmatrix} \tag{3}$$

If all non-diagonal terms vanish (all terms except S_{xx}, $S_{\varphi\varphi}$, and S_{bb} are zero), the values E_{xx}, $E_{\varphi\varphi}$, and E_{bb} are the same as S_{xx}, $S_{\varphi\varphi}$, and S_{bb}, respectively. If this is not the case, it means that S_{xx} is the longitudinal stiffness that is observed when twist and bending strains are constrained during loading. On the other hand, E_{xx} corresponds to the longitudinal stiffness when twist and bending are free (M_x and M_b are zero).

Let us assume that we have a cable that has off-diagonal terms, which means that tension, twist, and bending are coupled. When we use an efficient cable model that cannot account for those coupling terms, we can fit either S_{xx}, $S_{\varphi\varphi}$, and S_{bb} or E_{xx}, $E_{\varphi\varphi}$, and E_{bb}. In the first case, the modeled cable has the same stiffness as the real cable when all other strains are set to zero during loading. For tension, this means that torsion φ_x and curvature κ are constrained during loading. When fitting E_{xx}, $E_{\varphi\varphi}$, and E_{bb}, the efficient cable model shows the same stiffness as the real cable during loading in one direction when strains in the other directions are unconstrained.

For an FEM model of a cable, the cable's stiffness matrix can be obtained by applying three orthogonal strain vectors similar to [19]. The stiffness matrix can be built from the resulting load vectors. If the applied strains $\varepsilon_{x,0}$, $\varphi_{x,0}$, and κ_0 are set to 1, the resulting load vectors constitute the columns of the stiffness matrix. Otherwise, the terms of the stiffness matrix must first be divided by the applied strain.

$$\begin{pmatrix} \varepsilon_x \\ \varphi_x \\ \kappa \end{pmatrix} = \begin{pmatrix} \varepsilon_{x,0} \\ 0 \\ 0 \end{pmatrix}, \begin{pmatrix} 0 \\ \varphi_{x,0} \\ 0 \end{pmatrix}, \begin{pmatrix} 0 \\ 0 \\ \kappa_0 \end{pmatrix} \tag{4}$$

2.2. Cable-Modeling Approaches

The cables can be modeled either by using solid elements that share nodes with the surrounding rubber, by using a beam that is coupled in some way to the corresponding rubber nodes, or with a combination of solid and beam elements (see Figure 3). The nodes of the beam in the solid/beam approach cannot transmit rotation since a direct nodal connection is used and the solid element nodes do not have rotational degrees of freedom. Each option requires a specific calibration of material parameters. These parameters are not physical but selected such that the whole modeled cable captures the target elastic response.

Our efficient cable-modeling approaches aim to reach S_{xx}, $S_{\varphi\varphi}$, $S_{x\varphi}$, and S_{bb} as closely as possible (Section 3.1 will show that S_{xb} and $S_{\varphi b}$ can generally be neglected). Some simplified approaches are also investigated that do not account for the coupling term $S_{x\varphi}$.

The first challenge is to independently capture the tensile and bending stiffness. This can be done in the following ways:

(a) Solid elements: Use a material that has different tensile and compressive stiffness.
(b) Beam elements: Set the radius of the beam such that S_{xx} and S_{bb} fit the target values.

Solid/beam approach: The whole bending stiffness is captured by the solid elements, whereas beam elements are used to capture the tensile stiffness that is not captured by the solid elements; see [16]. The beam elements have a very small cross-section such that the high tensile stiffness does not affect the overall bending stiffness.

J. Compos. Sci. **2022**, 6, 152 5 of 20

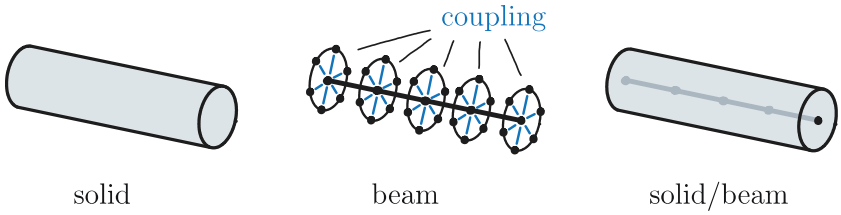

Figure 3. The three modeling approaches used for the cables: solid, beam, and a combination of both.

In the following, the cable-modeling approaches are presented and their material parameters are derived. For a linear elastic material model with cubic symmetry, the Young's modulus E, the shear modulus G, and the Poisson's ratio ν can be selected independently. For all models with linear elastic material, ν is set to zero in order to avoid unphysical effects in the cable deformation.

To account for the tension/torsion coupling of the cable, the linear elastic cubic material can be extended to a special kind of anisotropy that couples $\gamma_{\varphi z}$ and ε_{zz} in the cylindrical coordinate system of the cable:

$$\begin{pmatrix} \sigma_{xx} \\ \sigma_{yy} \\ \sigma_{zz} \\ \tau_{xy} \\ \tau_{xz} \\ \tau_{yz} \end{pmatrix} = \begin{pmatrix} E_{11} & 0 & 0 & E_K & 0 & 0 \\ 0 & E_{11} & 0 & 0 & 0 & 0 \\ 0 & 0 & E_{11} & 0 & 0 & 0 \\ E_K & 0 & 0 & G_{11} & 0 & 0 \\ 0 & 0 & 0 & 0 & G_{11} & 0 \\ 0 & 0 & 0 & 0 & 0 & G_{11} \end{pmatrix} \begin{pmatrix} \varepsilon_{xx} \\ \varepsilon_{yy} \\ \varepsilon_{zz} \\ \gamma_{xy} \\ \gamma_{xz} \\ \gamma_{yz} \end{pmatrix}, \quad \text{if } E_K = 0: \begin{cases} E_{11} = E \\ G_{11} = G \end{cases} \tag{5}$$

The parameter E_K accounts for the coupling of $\gamma_{\varphi z}$ and ε_{zz}. Whereas E_{11} and G_{11} are taken from the analytical calculations, E_K is calibrated to reach the target $S_{x\varphi}$ value of the efficient cable model. If E_K is set to zero, the coupling vanishes and the model corresponds to cubic material symmetry, with independent values of E and G, and the Poisson's ratio is set to zero, as in the cubic approach. This linear elastic material model is suited for both solid elements and beam elements. Alternatively, a hyperelastic material model with anisotropic stiffness is used in the solid models. This hyperelastic modeling approach can account for both the tension/torsion coupling and the tensile and bending stiffness and is introduced in the next section.

The material parameters of the homogenization approaches can be calculated analytically or calibrated using FEM models. The analytical calculations are based on the equations for a beam with circular cross-section and radius R. The tensile stiffness S_{xx}, torsional stiffness $S_{\varphi\varphi}$, and bending stiffness S_{bb} of the beam can be written as

$$S_{xx} = E\,A \quad \text{with } A = \pi\,R^2 \tag{6}$$

$$S_{\varphi\varphi} = G\,I_P \quad \text{with } I_P = 0.5\,\pi\,R^4 \tag{7}$$

$$S_{bend} = E\,I \quad \text{with } I = 0.25\,\pi\,R^4 \tag{8}$$

The elastic material parameters for the beam, solid, and solid/beam approaches are derived in the following. There, the S_{ij} components are written in the equations. To fit E_{ij} with the homogenized cable (see Section 2.1 for details), the S_{ij} terms in the formulas can be replaced by the corresponding E_{ij} terms, which then, of course, yields the corresponding stiffness for unconstrained loading.

2.2.1. Solid Approaches

There are two types of solid element approaches, where the material model is (a) linear elastic (with either cubic or anisotropic material symmetry) or (b) hyperelastic with anisotropic material response using the Holzapfel–Gasser–Ogden (HGO) formulation.

For linear elastic material, the Young's modulus and shear modulus of the material can be computed directly from the target values of tensile stiffness S_{xx} and torsional stiffness $S_{\varphi\varphi}$ as

$$E = \frac{S_{xx}}{A} \tag{9}$$

$$G = \frac{S_{\varphi\varphi}}{I_P} \tag{10}$$

This approach results in a bending stiffness S_{bend} that can be computed using the cable radius R by

$$S_{bend} = E\frac{\pi R^4}{4} = S_{bb} \tag{11}$$

This means that for the solid approach with cubic material, the axial stiffness S_{xx} and the torsional stiffness $S_{\varphi\varphi}$ can be made to fit while the bending stiffness is too high. The tension/torsion coupling can be captured when the anisotropic linear elastic material is chosen and the previously introduced coupling term E_K is calibrated.

The solid approach can account for S_{xx}, $S_{\varphi\varphi}$, S_{bb}, and $S_{x\varphi}$ when a material model with anisotropic behavior and a difference in its tensile and compressive stiffness is used. One such model is the Holzapfel–Gasser–Ogden (HGO) material model [20,21], which considers a hyperelastic matrix material model with fiber reinforcements. The HGO matrix uses the neo-Hookean model parameter C_{10}; the parameters k_1 and k_2 define the stiffness of the reinforcements. The parameter κ defines the level of dispersion of the fiber directions and lies between 0 for uniaxial orientation and 1/3 for evenly distributed fiber orientations. In the HGO model, the reinforcements only increase the stiffness of the material in the fiber direction under tension, but not under compression. It thus provides the possibility to reach a lower bending stiffness with solid elements, in contrast to the linear elastic anisotropic modeling approach. For this modeling approach, κ is set to zero to model uniaxial reinforcement. The parameter k_2 is an additional parameter to account for nonlinear effects and is set to $k_2 = 1$ in this work. The parameter D of the HGO model is set to zero, which is equivalent to incompressible material behavior. This deviates from the linear elastic cable models where ν is set to 0. Since, compared to the rubber, there are only small deformations in the cables, this inconsistency is expected to have a negligible effect on deformations and stresses. Within this HGO approach, the cable is modeled by solid elements and the orientation of the reinforcements is defined to be wound similar to the strands in a cable with a helix angle α_{HGO}. Note that this α_{HGO} of the HGO model approach can differ from the actual helix angle of the cable since it is calibrated to fit the stiffness components of the cable. The fitting parameters of the HGO approach, therefore, are this helix angle α_{HGO}, the material stiffness parameters of the matrix C_{10}, and the stiffness parameter of the reinforcements k_1.

2.2.2. Beam Approaches

When the cable is modeled using beam elements, the beam radius r can be used to also fit the bending stiffness of the cable. To that end, the equations for S_{xx} and S_{bb} can be formulated for the two unknowns, E and r:

$$S_{xx} = E\, r^2 \pi \tag{12}$$

$$S_{bb} = E\frac{\pi\, r^4}{4} \tag{13}$$

After eliminating r by inserting Equation (12) into Equation (13), the Young's modulus can be written as

$$E = \frac{S_{xx}^2}{4\,\pi\, S_{bb}} \tag{14}$$

This expression for E can be inserted into Equation (12) to yield the beam radius r:

$$r = \sqrt{\frac{S_{xx}}{\pi E}} \tag{15}$$

Using Equation (10), the shear modulus of the beam can be calculated from the radius r and the desired $S_{\varphi\varphi}$ as

$$G = \frac{S_{\varphi\varphi}}{I_P} = \frac{2\,S_{\varphi\varphi}}{\pi\,r^4} \tag{16}$$

This means that the beam approach can capture S_{xx}, $S_{\varphi\varphi}$, and S_{bb} by adjusting E, G, and r. Furthermore, $S_{x\varphi}$ can be captured using a calibrated E_K of the linear elastic material model.

2.2.3. Solid/Beam Approaches

For a combination of solid and beam elements, the Young's modulus of the solid elements E_s is calculated from the bending stiffness:

$$E_s = \frac{S_{bb}}{I} \tag{17}$$

The shear modulus follows directly from the torsional stiffness; see Equation (10).

A beam radius r_b is applied to the beam elements, which is a factor of 1000 smaller than the actual cable radius. Thus, the contribution of the beam elements to the torsional and bending stiffness can be neglected. The Young's modulus for the beam elements is chosen such that the combination of solid stiffness and beam stiffness add up to the desired longitudinal stiffness S_{xx}:

$$E_b = \frac{S_{xx} - E_s\,A}{\pi\,r_b^2} \tag{18}$$

2.3. Single Cable Models

In this section, two kinds of single cable models are introduced. The first is a model with fully modeled steel wires and rubber. This model is used to obtain the cable stiffness matrix S_{ij}, which serves as a reference for the other models. The modeling with steel wires and rubber is referred to as full geometry in the following. The second kind of single cable models are the efficient cable models, which are set up to mimic the reference stiffness S_{ij} using solid elements, beam elements, or a combination of both.

The load definition and the computation of the stiffness are the same for the full-geometry cable model and the efficient single cable models. At the center of the two ends of the modeled cable, reference points are defined. All nodes of the two end surfaces (or end nodes in the case of the beam models) are rigidly coupled to the corresponding reference point. The load is applied at the right-side reference point while the left-side reference point is completely fixed. This constraint of the radial displacements introduces an additional stiffness to the model. It thus must be checked whether the modeled cable length L_{cable} is long enough for the influence of these end effects to vanish. The models are analyzed using the implicit nonlinear solver of Simulia Abaqus [18].

2.3.1. Full-Geometry Single-Cable Model

The full-geometry cable model uses a seven-wire rubberized strand as a very simple example of a cable. The strand geometry is defined in Figure 4 and Table 1. It is adapted from [7], but to provide a good-quality mesh [12], the rubber gap between the middle wire and the outer wires is increased. The steel of the wires is modeled linear elastically using a Young's modulus as given in [7], E = 188 GPa, and Poisson's ratio ν = 0.3; the helix angle α of the strand is 11.8°. A perfect bond between the rubber and the steel wires is modeled (they share the same nodes in the interface) such that there can be no debonding or friction. The rubber is modeled as a Mooney–Rivlin hyperelastic material model with its parameters C_{10},

C_{01}, and d_1 taken from [22] as 0. MPa, 0. MPa, and 0. MPa, respectively. The full-geometry single-cable model uses two meshing options: (a) bilinear hexahedral elements with hybrid formulation (C3D8H) for the rubber elements and reduced integration (C3D8R) for the steel elements and (b) quadratic tetrahedral elements with hybrid formulation (C3D10H) both for rubber and steel elements.

The strand length L_{strand} of a cable is the axial distance at which one wire is completely wound around the cable axis. This length L_{strand} depends on the helix angle α and the distance between the cable axis and the axis of the wire. In the case of the seven-wire strand used, the strand length of the six outer wires is calculated as

$$L_{\text{strand}} = (r_{\text{i}} + r_{\text{o}} + d)\,\frac{2\,\pi}{\tan(\alpha)} = 118.8\ \text{mm} \tag{19}$$

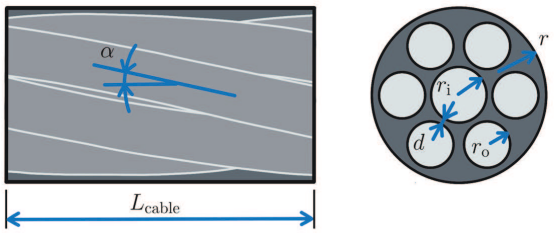

Figure 4. The geometry of the full-geometry single-cable model with its key parameters.

Table 1. Geometric parameters of the seven-wire strand.

Parameter Name	Value
Radius r (mm)	6
inner radius r_{i} (mm)	1.95
outer radius r_{o} (mm)	1.75
gap d (mm)	0.25
winding angle α (°)	11.8

The wires in the strand can be wound in two directions, referred to as the z-type and the s-type, where z is wound like a right-hand screw and s like a left-hand screw. All single cable models use the z-type (see Figure 4) and for the efficient models of s-cables needed in the tree-cable specimen, $S_{\text{x}\varphi}$ of the z-type cable is multiplied by -1.

2.3.2. Efficient Single-Cable Models

As stated in Section 2.2, the efficient cable models can be divided into approaches that use cubic material models and approaches that use some kind of anisotropic material response. The latter can be implemented using a linear elastic or hyperelastic material model to account for the tension/torsion coupling of the cables. For both the cubic and anisotropic approaches, cable models consisting of beam elements, solid elements, or both solid and beam elements can be set up. Table 2 defines the combinations of elements and material models used in this study.

Table 2. Options of the efficient modeling approaches in terms of elements and material models used.

	Linear Elastic		Hyperelastic
Approach	**Cubic (E, G, ν = 0)**	**Anisotropic (E, G, E_K)**	**HGO (C_{10}, k_1, α_{HGO})**
Solid	x	x	x
Beam	x	x	-
Solid/beam	x	-	-

The grey areas in Table 2 indicate the combinations that had not been implemented. The hyperelastic material model is used for solid elements only. The solid/beam does not use anisotropic solid material because there, the solid elements represent only a small part of the cable's tensile stiffness. This means that the tension/torsion coupling could not be achieved. The solid/beam approach does not use anisotropic material for the beam because the beam rotation cannot be transmitted through the nodes they share with the solid elements.

The parameters for the efficient cable models (E_K for the anisotropic solid and beam models and all parameters of the HGO model) are derived as described in Section 2.2. The calibration procedure of those parameters uses a Nelder–Mead algorithm [23]. For the length of the efficient single-cable models, 40% of the strand length (40% of 118.8 mm) have proven to be sufficient and the global mesh size is set to 1 mm. In the longitudinal direction, the length of the elements is set to 3 mm. For the anisotropic approaches that can feature tension/torsion coupling, S_{ij} components are used to obtain the model parameters. Note that for the solid and beam model, E_K is calibrated to best fit S_{couple}. With the solid HGO approach, all four S_{ij} components are used for the calibration. Although more increments are needed for convergence in the HGO approach, the resulting force and moment curves are approximately linear within the modeled load range. To ensure that the minimum found for the HGO approach in the calibration procedure is not a local one, three starting points of the C_{10}, k_1, and α_{HGO} parameters are evaluated: 600 MPa, 10,000 MPa, 5°; 600 MPa, 26,500 MPa, 11°; and 500 MPa, 10,000 MPa, 20°. They all yield approximately the same results as those stated in Section 3.2. The efficient single cable models are meshed by bilinear hexahedral elements with hybrid formulation (C3D8H) for the solid regions and linear beam elements (B31) for the beams.

2.4. Model of the Three-Cable Specimen

The cable modeling approaches are assessed using an FEM model of a three-cable shear specimen. The geometry and boundary conditions of the specimen are defined in Figure 5. The corresponding geometry parameters are defined in Table 3.

All nodes on the left faces of the two outer cables are fully constrained. Similar to the single-cable models, the right face nodes of the central cable are rigidly connected to a reference point that is used to apply the displacement load of 10 mm in the x-direction. During loading, all other displacements of the reference point except the rotation around the x-axis are constrained. When the center cable is pulled in the positive x-direction, the load is transferred through the rubber to the outer cables that are fixed on the left side. The cables are modeled as defined for the full-geometry cable model or the efficient cable models. The rubber properties defined in Section 2.3.1 are taken for the rubber region.

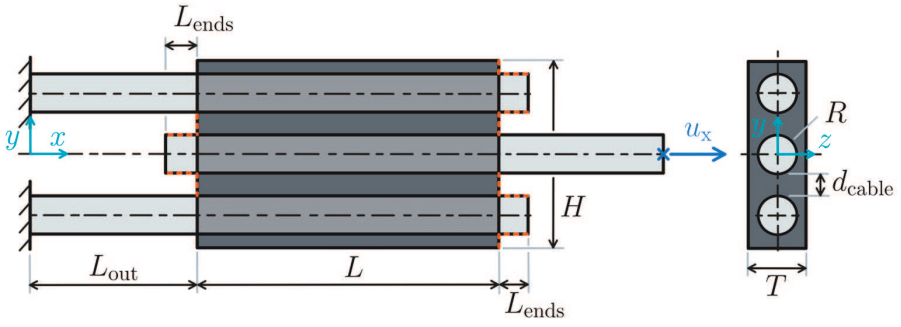

Figure 5. The geometry of the three-cable specimen. Contact is defined in the orange-dashed regions.

The orange-dashed lines in Figure 5 mark regions that can come into contact when the specimen is loaded. This contact is defined using a penalty algorithm and frictionless behavior. For the model with full geometry, quadratic hybrid tetrahedral elements (C3D10H) with a typical edge length of 1.25 mm are used. This model contains about

620,000 elements. The efficient cable models use bilinear hybrid hexahedral elements and reduced integration with a typical element edge length of about 1 mm and a swept mesh along the x-axis. In the sweeping direction, the element edge length is set to 3 mm. This swept mesh is important for the beam-type modeling approach, where the rubber nodes that lie on the outer cable surface are rigidly connected to the beam node that has the same x-coordinate, as illustrated in Figure 3. The models with solid and solid/beam approaches use about 77,000 elements and the beam approach models contain about 33,000 elements. The same element types as stated in Section 2.3.2 are used.

Table 3. Geometry parameters of the three-cable model.

Parameter Name	Value
length L (mm)	100
height H (mm)	62
depth T (mm)	20
outer cable length L_{out} (mm)	100
cable end length L_{ends} (mm)	10
cable distance d_{cable} (mm)	8

Several combinations of s-type and z-type cables are possible in the specimens. Here, the setup with bottom, central, and top cable s, z, and s is used, respectively. For this szs setup, the outer cables and the center cable want to rotate in opposite directions. Note that for a cable-reinforced component with a large number of parallel cables, the component will not be as free to twist as the three-cable specimen, and the stresses will be affected by the cable's tension/torsion coupling.

3. Results and Discussion

In this section, results are presented first for a single cable using the full-geometry and efficient modeling techniques. Afterward, results of three-cable specimen models are presented. The cable-modeling approaches are evaluated using the three-cable models in terms of the specimen's stiffness, deformation field, and strain fields in the rubber.

3.1. Full-Geometry Single-Cable Model

The full-geometry model of the seven-wire strand is used to obtain the components of the stiffness matrix that are used to evaluate the efficient cable models. Here, we look into the nonlinearity of the overall stiffness response of the full model and the influence of element type, mesh size, and cable length on the cable's stiffness, which is relevant for the full-geometry three-cable specimen of Section 3.3. The length of the modeled cable is quantified as a fraction of the strand length (the axial distance so that the outer wires are completely wound around the cable axis, as described in more detail in Section 2.3.1) and denoted as relative cable length.

To show the nonlinearity in the cable stiffness, two load cases are studied. A cable load ($\varepsilon_{x,0}$, $\varphi_{x,0}$, κ_0) of (5%, 0,0) and (0, 0, 10/m) is applied in load case A and load case B, respectively. Figure 6 shows the axial force F_x, the torsional moment M_x, and the bending moment M_b of the cable over the longitudinal strain ε_x (load case A, Figure 6a) and over the curvature κ (load case B, Figure 6b). For a mesh size of 0.5 mm and a relative cable length of 0.8, the F_x and M_x plots are approximately linear, whereas the M_b curve shows a slight nonlinearity towards higher curvatures.

The influence of cable length and mesh size are investigated for applied loads of $\varepsilon_x = 0.5\%$, $\varphi_x = 2$ rad/m, and $\kappa = 1/m$, which are applied individually. The longitudinal strain of 0.5% corresponds to a maximum Mises stress of $\sigma_{mises} = 960$ MPa in the central wire and a total force of $F_x = 60$ kN. We here assume that those loads cover the relevant range for the intended applications and that nonlinear effects that occur at higher loads can

be neglected. The stiffness parameters are evaluated as secant stiffnesses of the loading curves and are plotted over the cable length and mesh size in Figure 7. The range and units of the individual stiffness parameters S_{xx}, $S_{\varphi\varphi}$, S_{bb}, $S_{x\varphi}$, and $S_{\varphi x}$ are quite different. To better visualize the dependency of those parameters on the cable length and mesh size, they are plotted relative to their respective most accurate values (such as those obtained for either highest cable length or smallest mesh size, as explained in the following).

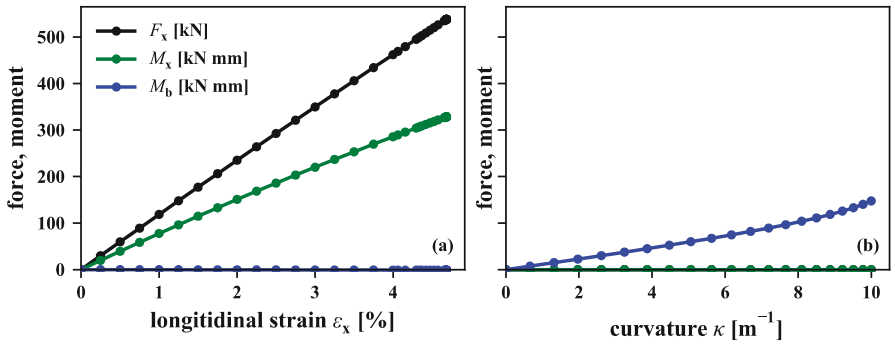

Figure 6. Tensile force, torsional moment, and bending moment plotted over (**a**) the longitudinal strain ε_x and (**b**) the curvature κ of the seven-wire strand model for a mesh size of 0.5 mm and a relative cable length of 0.8.

In Figure 7a, the cable length is varied for linear hexahedral elements with reduced integration and a fixed mesh size of 0.5 mm. The relative cable length of 1.4 is assumed to give the most accurate results, so those S_{ij} components are used to normalize the respective results of the other models. As expected, the rigid connection from the cable ends to their corresponding reference points introduces numerical artifacts that increase the evaluated S_{ij} components for smaller cable lengths. The bending stiffness S_{bb} is particularly sensitive to these cable end effects.

The element type and mesh size are varied in Figure 7b for a constant relative cable length of 1.2, since this is the length for which the stiffness parameters have already reached a plateau, as shown in Figure 7a. The results for the smallest mesh size of the quadratic tetrahedral elements (0.75 mm) are used to normalize S_{ij}. The curves for bilinear hexahedral and quadratic tetrahedral elements show that the finer the mesh size, the higher the computed stiffness components. For the hexahedral elements, no clear plateau of S_{ij} components is reached for the finest mesh size of 0.3 mm. This indicates that bilinear hexahedral elements would need to be much finer to accurately compute the cable's stiffness. The quadratic tetrahedral element results show a plateau at a mesh size of about 1 mm. Similar to the cable length study, the bending stiffness S_{bb} is most sensitive to the mesh size. The 1.25 mm mesh with quadratic tetrahedral elements (see the pictogram in Figure 7b) yields acceptable computation times and quite accurate results: The stiffness parameters are up to 4% lower than for a mesh size of 0.75 mm. Therefore, in the bigger three-cable specimen models with full geometry, quadratic tetrahedral elements with a mesh size of 1.25 mm are used.

Table 4 lists the model size, necessary RAM, and computation time for the full-geometry single-cable models of Figure 7. To keep the table short, only model parameters of the maximum and minimum cable length (length study) and mesh size (mesh study) are listed. For bilinear hexahedral elements, no mesh convergence is reached at a mesh size of 0.3 mm with computation times of 20 min. The finest quadratic tetrahedral element results took about 5 min to compute.

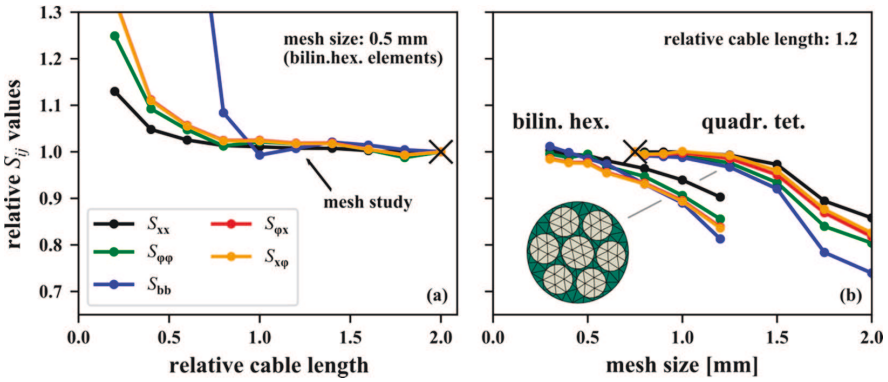

Figure 7. Relative stiffness components of the strand model with (**a**) varied cable length using bilinear hexahedral elements with a mesh size of 0.5 mm and (**b**) varied mesh size with both bilinear hexahedral and quadratic tetrahedral elements for a relative cable length of 1.2.

Table 4. Information on the model size, necessary RAM to load the full stiffness matrix, and computation time (four cores of a six-core Intel Xeon E5-1650 v3 @ 3.5 GHz workstation with 128 GB RAM) for the full-geometry single-cable model (tensile load case) with varied element type, relative cable length, and mesh size.

Mesh Type	Relative Length	Mesh Size (mm)	Nodes	Elements	Degrees of Freedom	Necessary RAM (MB)	Computation Time
Hex.	0.2/2	0.5	14,427/158,021	10,162/109,965	40,397/396,291	240/3985	0:07 min/4:54 min
Hex.	1.4	0.3/1.2	474,907/14,352	344,606/8744	1,203,365/35,068	19,867/205	20:19 min/0:08 min
Tet.	1.4	0.75/2	40,509/36,660	26,702/14,304	100,875/82,882	738/442	4:56 min/0:43 min

The finest mesh size of the tetrahedral elements is assumed overall to give sufficiently accurate S_{ij} components. Those S_{ij} components for the quadratic tetrahedral elements with a mesh size of 0.75 mm and a relative cable length of 1.2 are therefore extracted. The efficient cable models are set up to fit these components:

$$\begin{pmatrix} S_{xx} & S_{x\varphi} & S_{xb} \\ S_{\varphi x} & S_{\varphi\varphi} & S_{\varphi b} \\ S_{bx} & S_{b\varphi} & S_{bb} \end{pmatrix} = \begin{pmatrix} 11,793.2\ \text{kN} & 7,746.3\ \text{kN mm} & 0 \\ 7941.3\ \text{kN mm} & 15,593.5\ \text{kN mm}^2 & 0 \\ 0.5\ \text{kN mm} & -0.7\ \text{kN mm}^2 & 10,837.4\ \text{kN mm}^2 \end{pmatrix}. \tag{20}$$

Since the matrix is nearly symmetrical, we make it symmetrical by setting S_{bx} and $S_{b\varphi}$, which are much smaller than the other components, to zero and introduce a parameter S_{couple} that we use in the following for both $S_{x\varphi}$ and $S_{\varphi x}$:

$$S_{xb} = S_{bx} = S_{\varphi b} = S_{b\varphi} = 0 \tag{21}$$

$$S_{couple} = \frac{S_{x\varphi} + S_{\varphi x}}{2} \equiv S'_{x\varphi} = S'_{\varphi x} \tag{22}$$

This simplification results in only four S_{ij} parameters that should be reached in the efficient cable models; see Table 5. Inverting the simplified S_{ij} matrix yields E_{ij}. As mentioned in Section 2.1, the cubic modeling approaches can be fitted based on either S_{ij} or E_{ij}.

Table 5. Stiffness parameters S_{ij} and E_{ij} from the full cable model with quadratic tetrahedral elements (mesh size of 0.75 mm) and cable length per strand length of 1.2.

S_{xx}	11,793	kN	E_{xx}	7848	kN
$S_{\varphi\varphi}$	15,594	kN mm^2	$E_{\varphi\varphi}$	10,376	kN mm^2
S_{couple}	7843	kN mm	E_{couple}	−15,601	kN mm
S_{bb}	10,837	kN mm^2	E_{bb}	10,837	kN mm^2

3.2. Efficient Single-Cable Models

The cable-modeling approaches introduced in Section 2.2 are set up as described in Section 2.3. Table 6 lists the parameters that are either calculated analytically or calibrated using the cable FEM models. To obtain the model parameters, the stiffness parameter S_{ij} or E_{ij} are used. For the approaches that do not have a tension/torsion coupling, the parameters are calculated once with S_{ij} and once with E_{ij}.

Table 6. Material and geometry parameters for the efficient cable models from analytical calculation or calibration by FEM models.

	Fit Towards	***E* (GPa)**	***G* (GPa)**	**E_K * (GPa)**	
Solid	E_{ij}	69.39	5.097	-	
	S_{ij}	104.3	7.660	17.32	
	Fit towards	C_{10} * (GPa)	k_1 * (GPa)	k ** [1]	α_{HGO} * (°)
Solid, HGO	S_{ij}	0.7581	26.47	0.0	14.08
	Fit towards	E (GPa)	G (GPa)	r (mm)	E_K * (MPa)
Beam	E_{ij}	452.2	216.6	2.35	-
	S_{ij}	1021	735.1	1.917	531.5
Solid/beam	Fit towards	E_{solid} (GPa)	G_{solid} (GPa)	r_{beam} ** (mm)	E_{beam} (GPa)
	E_{ij}	10.65	5.097	0.006	58,740,000
	S_{ij}	10.65	7.660	0.006	93,628,000

* Calibrated to fit S_{ij}. ** Chosen values.

Figure 8 shows the components of S_{ij} and E_{ij} obtained for the cubic modeling approaches. The diagrams use a logarithmic scale with relative values normalized to the target S_{ij} or E_{ij} values stated in Table 5. Figure 8a,b show the stiffness values for cable model parameters calculated to fit S_{ij}. As expected, the stiffness parameters obtained for S_{ij} plotted in Figure 8a fit well to the target values, except for the bending stiffness in the solid approach, which is too high by a factor of 9. The fit of the beam and solid/beam approaches is equally good. The E_{ij} components for the same efficient cable models, however, are about 53% higher than the components of the full-geometry model. When the cable models are calibrated to E_{ij} (see Figure 8c,d), the E_{ij} components fit well, but components of S_{ij} are lower by about 36%. This shows that for a cable that has tension/torsion coupling ($S_{x\varphi} \neq 0$), an efficient cable model with cubic material can fit either S_{ij} or E_{ij} but not both at the same time. S_{xx} corresponds to the stiffness in tension with constrained torsion and E_{xx} to tension with free torsion. When using such a cable model with cubic material, the

model's parameters should be calculated depending on the application of the model. If the application is unknown, an intermediate stiffness of S_{ij} and E_{ij} should be used for the models.

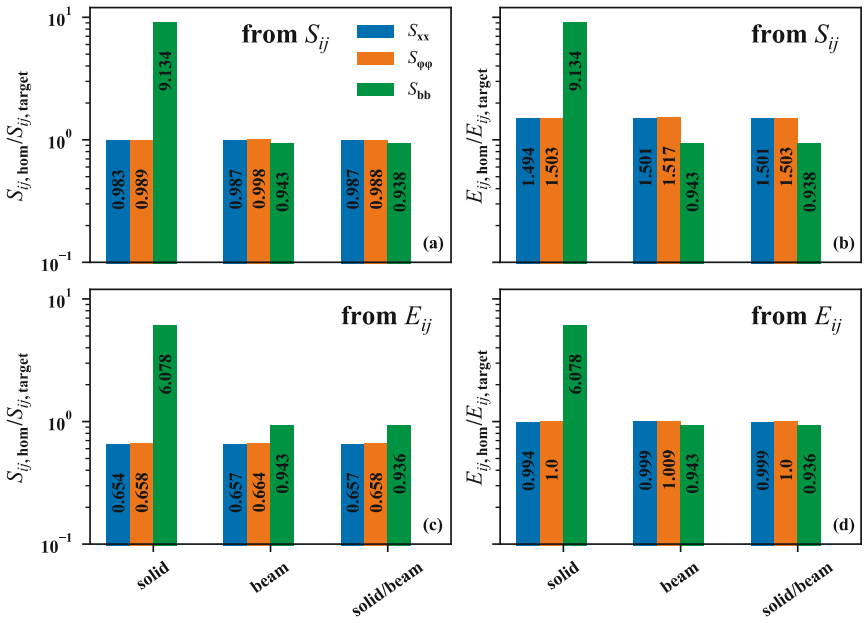

Figure 8. Components of S_{ij} and E_{ij} relative to their target values for varying cable-modeling approaches without anisotropic material behavior. The parameters of the models are calibrated to (**a**,**b**) fit S_{ij} or (**c**,**d**) fit E_{ij}.

Three efficient cable-modeling approaches that can account for the tension/torsion coupling are investigated, and their S_{ij} and E_{ij} components are plotted in Figure 9. Similar to the cubic approaches, the bending stiffness of the solid approach is too high by a factor of 7.8. The solid, solid–HGO, and beam approaches can capture S_{ij} well; see Figure 9a. The largest differences are observed for $S_{x\varphi}$ in the solid–HGO approach, which is 22% higher than the target value. Note that due to having only three calibration parameters in the HGO approach, the four independent stiffness parameters cannot all be fitted at the same time. Other HGO parameters such as D, k_2, and κ could be fitted as well but do not help to improve the accuracy of S_{ij}.

The components of the E_{ij} matrix of the solid and the beam approach in Figure 9b fit well to the target E_{ij} components, except for the E_{bb} of the linear elastic solid approach. For the solid–HGO approach, only the E_{bb} component fits well, whereas the other E_{ij} terms are lower by 46% to 60%. This is due to an amplification of the deviation of the S_{ij} components since the S_{ij} matrix is inverted to calculate E_{ij}. Furthermore, the convergence in the simulations with the solid HGO approach is bad, which requires many more iterations in the FEM simulation. The solid approach can therefore be used for applications where bending does not play a role, and the beam approach can be used in all cases where inaccuracies related to the coupling of the beam nodes to the rubber are acceptable—for example, because the rubber/cable interface is not of special interest in the model.

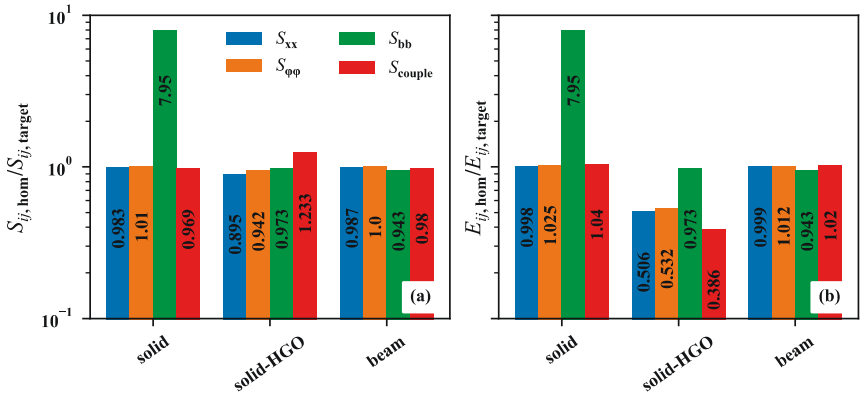

Figure 9. The three anisotropic efficient cable-modeling approaches with their relative stiffness values in terms of (**a**) S_{ij} and (**b**) E_{ij}. Note that the parameters of the efficient models were calculated or fit to reach S_{ij}.

3.3. Three-Cable Models

The three-cable shear specimens of the szs-type with efficiently modeled cables are now evaluated in terms of stiffness, deformation fields, and stress fields, and compared to the full-geometry results. The rubber between the outer and the central cable is sheared, and the forces in the cables causes them to rotate in opposite directions, which is only slightly hindered by the rubber.

3.3.1. Stiffness of the Three-Cable Specimens

Figure 10 shows the longitudinal force F_x and the end rotation of the central cable φ_x versus the end displacement u_x. The dashed black line and the solid lines illustrate the response of the full-geometry and efficient approaches, respectively. A linear relation of both F_x and φ_x with respect to u_x can be seen.

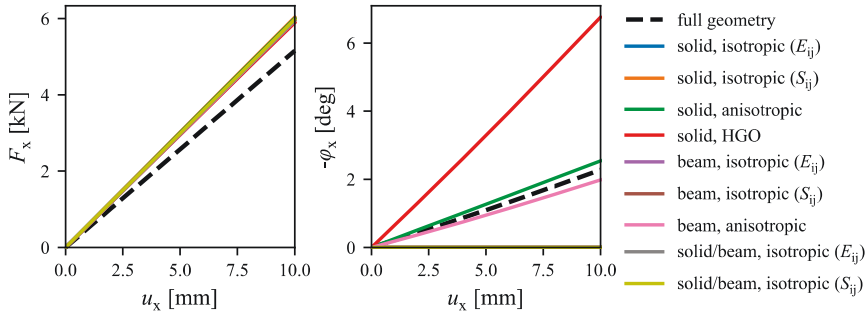

Figure 10. Force–displacement and end rotation–displacement plots of the three-cable szs-type specimen with free end rotation φ_x.

There is good agreement between the F_x curves of all the efficient cable-modeling approaches, but they all lie above the F_x of the model with full geometry by about 14%. This can partly be explained by the non-uniform strain fields in the full-geometry model. Furthermore, the results in Section 3.1 show that the mesh of the full-geometry three-cable model can underestimate the cable stiffness by up to 4%, which can also contribute to this difference. In addition, the full-geometry model has a layer of rubber around the wires that can be sheared (see Figure 4, where the gap from the six outer wires to the surface of the whole cable can be written as $r - r_i - 2\,r_o - d = 0.3$ mm). In the efficient models, this outer gap is assigned the same material properties as the rest of the cable, which is much

stiffer than the rubber. When an efficient model is fitted to test data, the cable radius thus should be set to not include this layer of rubber to avoid this overestimation of stiffness in a rubber component. The end rotations of the central cable φ_x, plotted in Figure 10, are zero for all cubic modeling approaches since those models do not account for tension/torsion coupling. The anisotropic beam and anisotropic solid approaches show a good agreement with the full-geometry approach, whereas the solid–HGO approach overestimates the end rotation by about 150%.

The model size in terms of number of nodes, number of elements, degrees of freedom, necessary RAM to load the full stiffness matrix, and computation time are listed in Table 7 for all approaches in the three-cable model. There is a substantial difference in model size and computation time between the full-geometry approach and the efficient approaches, with the full-geometry model requiring about 50 GB of RAM to load the full stiffness matrix and a computation time of 4:35 h. The efficient three-cable models, on the other hand, need less than 2 GB of RAM and compute in about 2 min.

Table 7. Information on the model size, necessary RAM to load the full stiffness matrix, and computation time (four cores of a six-core Intel Xeon E5-1650 v3 @ 3.5 GHz workstation with 128 GB RAM) with varied model setup of the three-cable models.

	Nodes	Elements	Degrees of Freedom	Necessary RAM (MB)	Comp. Time
Full geometry	1,528,220	641,279	3,282,099	50,509	4:35 h
Solid	165,198	77,642	338,343	1953	2:16 min
Beam	74,053	33,990	165,081	843	0:46 min
Solid/beam	166,056	78,071	393,630	1961	1:45 min

3.3.2. Deformations of the Three-Cable Specimens

The tension/torsion coupling of the cables can cause a twisting of the specimen. One key result variable of this twist is the difference of the out-of-plane displacement u_z, which is plotted in Figure 11. If u_z is the same above and below the central cable, there is no twist—the displacement is merely a result of the Poisson effect in the rubber (especially the peaks at the right-hand side, which can be seen most clearly in Figure 11e). Otherwise, a twisting of the specimen occurs, which can be assessed by the u_z displacement at the top and bottom surface. Since such behavior can only be described by the anisotropic cable-modeling approaches, only one of the cubic approaches (solid/beam, fitted to S_{ij}) is shown for reference.

For the full-geometry model of Figure 11a, there is a distinct difference in the u_z fields above and below the central cable: On the top and the bottom of the specimen, a u_z of 0.7 mm and -0.7 mm is computed, respectively. Note that the highest values of u_z at the top face occur at about 60% along the length of the rubber block in the specimen. The results for the cubic cable-modeling approach (see Figure 11e) show a completely symmetric u_z field with respect to the xy-plane. The anisotropic solid approach in Figure 11b shows the same trend as the full-geometry model, but with a less pronounced twist of the specimen. The solid–HGO approach in Figure 11c, on the other hand, drastically overestimates the out-of-plane displacement of the specimen with u_z on the top and bottom of the specimen of 1.7 mm and -1.7 mm, respectively. The best agreement with the full-geometry model is obtained by the anisotropic beam approach of Figure 11d: The u_z fields are only slightly different above and below the center cable, with the top and bottom maximum values of u_z occurring on the right end of the rubber block.

The poor performance of the HGO model can be explained by the unwanted coupling factors inherent to this approach. In addition, the HGO approach requires the highest computational effort for a convergence of the simulation. The better fit of the anisotropic beam approach compared to the anisotropic solid approach can only be attributed to their difference in bending stiffness: Since the twisting of the specimen is associated with a

bending deformation of the cables, the excessive bending stiffness of the solid approach affects these results.

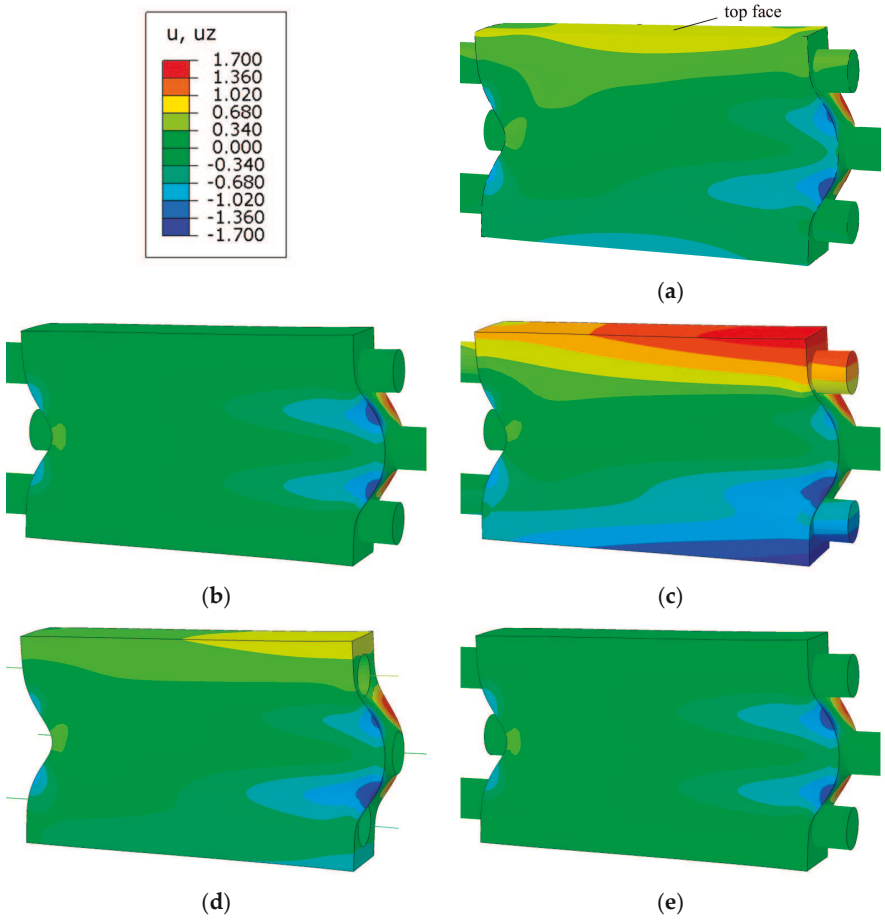

Figure 11. Contour plots of the out-of-plane displacements u_z in mm for (**a**) the full-geometry model and the four efficient cable-modeling approaches (**b**) solid, anisotropic, (**c**) solid, HGO, (**d**) beam, anisotropic, and (**e**) solid/beam, cubic (fit to S_{ij}) of the three-cable szs-type specimen with free end rotation.

3.3.3. Stresses in the Three-Cable Specimens

In many cases of reinforced rubber components, cable/rubber debonding and rubber failure is more relevant than deformations. Thus, the stresses in the rubber are evaluated in the following. It is assumed that the maximum principal stress σ_I is the best indicator for rubber failure. Figure 12 shows σ_I for the full-geometry model and various efficient modeling approaches. The specimen is cut in the plane of the cable axes. The main load of the rubber is shear between the central cable and the outer cables. These shear stresses, however, are not uniform and feature surface effects near the free surfaces at both ends of the rubber block (points A, A′, B, and B′): The highest σ_I occurs at the junction of the center cable and the rubber on the right-hand side of the specimen (point A and point A′). Those maximum values of σ_I amount to 12.54 MPa, 9.74 MPa, 9.87 MPa, 10.17 MPa, and 9.11 MPa for the full-geometry, solid–anisotropic, solid–HGO, beam–anisotropic, and solid/beam (fitted to S_{ij}) approach, respectively. The junction of cable and rubber material imposes a singularity. This means that those stresses depend on the mesh size in the model, which must be accounted for in failure predictions. For relative comparisons like geometric

studies with similar mesh, such results can be used nonetheless. There are also high stresses at the junction of the outer cables and the rubber on the left-hand side of the specimen (point B and point B′).

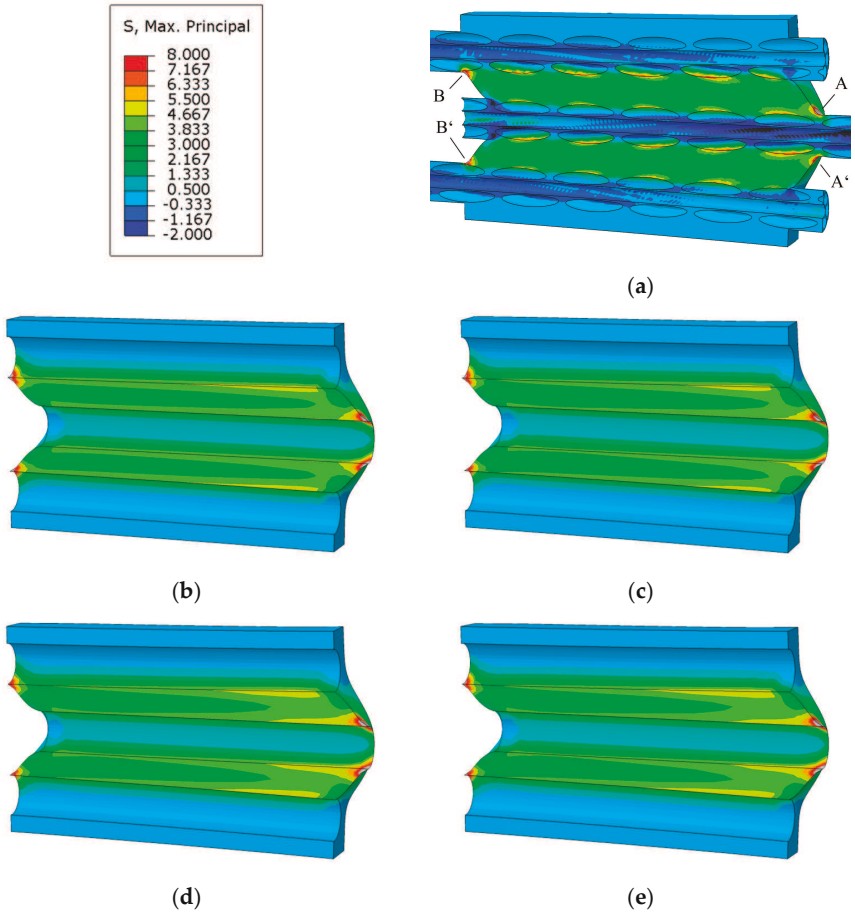

Figure 12. Contour plots of the maximum principal stress σ_I (MPa) for (**a**) the full-geometry model and the four efficient cable-modeling approaches (**b**) solid, anisotropic, (**c**) solid, HGO, (**d**) beam, anisotropic, and (**e**) solid/beam, cubic (fit to S_{ij}). The three-cable szs-type specimens are cut in the plane defined by z = 0.

The stress field in the full-geometry model shown in Figure 12a shows additional peaks where the cable wires reach farthest into the space between the center cable and the outer cables. This effect introduces another parameter to the model: If such a region coincides with the surface of the rubber block (is close to point A or A′), the stresses will be considerably higher. This effect is not studied here but should be considered when predicting the failure of cable–rubber specimens.

The stress fields in the models with efficiently modeled cables are more uniform. The stresses generally increase towards the right side of the specimen. Similar to the full-geometry approach, the highest maximum principal stresses occur at points A and A′. The highest maximum principal stress σ_I in the solid/beam approach (see Figure 12e) of 9.11 MPa is lower than that of the other modeling approaches (9.87 MPa to 10.17 MPa). This can be explained by the very low Young‘s modulus of the solid elements in the solid/beam approach, which leads to a shear deformation between the beam and the cable surface. The differences in the highest computed σ_I of the varying cable-modeling approaches are rather

low, indicating that for such three-cable specimens, a stress-based failure assessment is not sensitive to the selection of the modeling approach. There is a slight increase in the σ_I peaks due to the coupling term. For example, the beam approach computes maximum σ_I = 10.17 MPa in the anisotropic approach and $\sigma_I = 10.02$ MPa in the cubic approach.

4. Conclusions

A variety of approaches for efficiently modeling the elastic response of a steel cable in a reinforced rubber component is introduced and evaluated both as a single cable and in a three-cable shear specimen. The aim is to reach an accurate representation of the high tensile stiffness, the high torsional stiffness, the low bending stiffness, and the tension/torsion coupling of steel cables. The modeling approaches considered consist of beam elements, solid elements, or a combination of both. In addition to an approach with linear elastic material behavior and cubic material symmetry, a special kind of anisotropic linear elastic material model is selected and fitted to capture the tension/torsion coupling. Furthermore, an approach using an anisotropic hyperelastic material model (HGO) is evaluated. The cable-modeling approaches are able to model the target stiffness of the cable to a varying extent:

- Solid linear elastic approaches: The bending stiffness is too high, but the other stiffness components are captured.
- Solid approach with anisotropic hyperelastic material: Only three parameters are available to fit four independent stiffness parameters. Not all four of them can be calibrated accurately at the same time. At least one of them differs up to 20% from the target value.
- Beam approach: All components of the target stiffness can be captured. However, the beam nodes are rigidly coupled to the rubber nodes at the cable surface, which is only valid if the cable is considerably stiffer than the rubber.
- Solid/beam approach: The tension/torsion coupling could be implemented in the beams, but the beam rotations would need to be coupled to the solid nodes. This coupling would induce numerical artifacts and is thus not implemented. Furthermore, the solid elements in the solid/beam approach have a very low Young's modulus that can lead to unphysical shear deformations inside the cable.

From those observations, the best modeling approach can be selected for a given application. The key questions for this selection is whether the cables experience a bending deformation and whether the tension/torsion coupling plays an important role in the model's application. Generally, the anisotropic beam approach is easy to calibrate and can capture the stiffness of the cable well. Inaccuracies introduced by the coupling of rubber nodes to the beam may not be acceptable, like in applications where evaluations at the rubber/cable interface require solid elements in the cable. In this case, the solid approach can be used if the cable bending is not relevant or the solid/beam approach if the tension/torsion coupling can be neglected. If both bending and tension/torsion coupling need to be captured, the HGO approach can be used, but it is associated with considerable discrepancies of all components of the stiffness matrix.

This work shows how to calculate and calibrate the geometric and material parameters of all cable modeling approaches and how to implement them. There is no approach that is suited for all possible applications, such as conveyor belts, hydraulic hoses, or tires. The modeling approach should be selected with care based on the type of loads the cables are exposed to in the application.

Author Contributions: Conceptualization, M.P., S.M.F. and C.S.; methodology, S.M.F. and M.P.; software, M.P.; validation, M.P.; formal analysis, M.P.; investigation, M.P. and S.M.F.; resources, M.P.; data curation, M.P.; writing—original draft preparation, M.P.; writing—review and editing, M.P., S.M.F. and C.S.; visualization, M.P.; supervision, C.S.; project administration, M.P.; funding acquisition, C.S. and M.P. All authors have read and agreed to the published version of the manuscript.

Funding: This research was supported by the Austrian Research Promotion Agency (FFG) within the BRIDGE framework as part of the project "Entwicklung einer Methodik zur Vorhersage des Versagens in elastomeren Gurten mittels Finite Elemente Simulation," grant agreement.

Institutional Review Board Statement: Not applicable.

Informed Consent Statement: Not applicable.

Data Availability Statement: The methods for modeling cables are derived and evaluated independently of the FEM software used so other researchers can implement them into the FEM software they are using. Thus, no additional data need to be provided.

Conflicts of Interest: The authors declare no conflict of interest.

References

1. Utting, W.S.; Jones, N. A Survey of Literature on the Behaviour of Wire Ropes. *Wire Ind.* **1984**, *51*, 623–629.
2. Cardou, A.; Jolicoeur, C. Mechanical Models of Helical Strands. *Appl. Mech. Rev.* **1997**, *50*, 1–14. [CrossRef]
3. Costello, G.A. *Theory of Wire Rope*; Mechanical Engineering Series; Springer: New York, NY, USA, 1997; ISBN 978-1-4612-7361-5.
4. Feyrer, K. Wire Ropes Under Tensile Load. In *Wire Ropes*; Springer: Berlin/Heidelberg, Germany, 2015; pp. 59–177. ISBN 978-3-642-54995-3.
5. Wang, X.-Y.; Meng, X.-B.; Wang, J.-X.; Sun, Y.-H.; Gao, K. Mathematical Modeling and Geometric Analysis for Wire Rope Strands. *Appl. Math. Model.* **2015**, *39*, 1019–1032. [CrossRef]
6. Jiang, W.G.; Yao, M.S.; Walton, J.M. A Concise Finite Element Model for Simple Straight Wire Rope Strand. *Int. J. Mech. Sci.* **1999**, *41*, 143–161. [CrossRef]
7. Foti, F.; de Luca di Roseto, A. Analytical and Finite Element Modelling of the Elastic–Plastic Behaviour of Metallic Strands under Axial–Torsional Loads. *Int. J. Mech. Sci.* **2016**, *115–116*, 202–214. [CrossRef]
8. Chen, Y.; Meng, F.; Gong, X. Full Contact Analysis of Wire Rope Strand Subjected to Varying Loads Based on Semi-Analytical Method. *Int. J. Solids Struct.* **2017**, *117*, 51–66. [CrossRef]
9. Cao, X.; Wu, W. The Establishment of a Mechanics Model of Multi-Strand Wire Rope Subjected to Bending Load with Finite Element Simulation and Experimental Verification. *Int. J. Mech. Sci.* **2018**, *142–143*, 289–303. [CrossRef]
10. Utting, W.S.; Jones, N. The Response of Wire Rope Strands to Axial Tensile Loads—Part II. Comparison of Experimental Results and Theoretical Predictions. *Int. J. Mech. Sci.* **1987**, *29*, 621–636. [CrossRef]
11. Chen, Z.; Yu, Y.; Wang, X.; Wu, X.; Liu, H. Experimental Research on Bending Performance of Structural Cable. *Constr. Build. Mater.* **2015**, *96*, 279–288. [CrossRef]
12. Bonneric, M.; Aubin, V.; Durville, D. Finite Element Simulation of a Steel Cable-Rubber Composite under Bending Loading: Influence of Rubber Penetration on the Stress Distribution in Wires. *Int. J. Solids Struct.* **2019**, *160*, 158–167. [CrossRef]
13. Frankl, S.; Pletz, M.; Schuecker, C. Incremental Finite Element Delamination Model for Fibre Pull-out Tests of Elastomer-Matrix Composites. *Procedia Struct. Integr.* **2019**, *17*, 51–57. [CrossRef]
14. Nordell, L.K. Steel Cord Belt and Splice Construction. *Bulk Solids Handl.* **1993**, *13*, 685–693.
15. Fedorko, G.; Molnar, V.; Dovica, M.; Toth, T.; Fabianova, J. Failure Analysis of Irreversible Changes in the Construction of the Damaged Rubber Hoses. *Eng. Fail. Anal.* **2015**, *58*, 31–43. [CrossRef]
16. Frankl, S.M.; Pletz, M.; Wondracek, A.; Schuecker, C. Assessing Failure in Steel Cable-Reinforced Rubber Belts Using Multi-Scale FEM Modelling. *J. Compos. Sci.* **2022**, *6*, 34. [CrossRef]
17. Nordell, L.; Qiu, X.; Sethi, V. Belt Conveyor Steel Cord Splice Analysis. *Bulk Solids Handl.* **1991**, *11*, 863–868.
18. Abaqus. *Dassault Systèmes*; Simulia: Johnston, RI, USA, 2020.
19. Cartraud, P.; Messager, T. Computational Homogenization of Periodic Beam-like Structures. *Int. J. Solids Struct.* **2006**, *43*, 686–696. [CrossRef]
20. Holzapfel, G.A.; Gasser, T.C.; Ogden, R.W. A New Constitutive Framework for Arterial Wall Mechanics and a Comparative Study of Material Models. *J. Elast. Phys. Sci. Solids* **2000**, *61*, 1–48. [CrossRef]
21. Gasser, T.C.; Ogden, R.W.; Holzapfel, G.A. Hyperelastic Modelling of Arterial Layers with Distributed Collagen Fibre Orientations. *J. R. Soc. Interface* **2006**, *3*, 15–35. [CrossRef] [PubMed]
22. Froböse, T.; Overmeyer, L.; Poll, G. *Verfahren zur Ermittlung der Materialparameter für die Auslegung von Stahlseil-Fördergurtverbindungen mit Hilfe der FEM*; Berichte aus dem ITA; PZH Verlag: Garbsen, Germany, 2017; ISBN 978-3-95900-153-3.
23. Gao, F.; Han, L. Implementing the Nelder-Mead Simplex Algorithm with Adaptive Parameters. *Comput. Optim. Appl.* **2012**, *51*, 259–277. [CrossRef]

Paper C

Incremental finite element delamination model for fibre pull-out tests of elastomer-matrix composites

Authors: Frankl, Siegfried Martin
Pletz, Martin
Schuecker, Clara

Procedia Structural Integrity
DOI: 10.1016/j.prostr.2019.08.008

Available online at www.sciencedirect.com

ScienceDirect

Procedia Structural Integrity 17 (2019) 51–57

Structural Integrity Procedia

www.elsevier.com/locate/procedia

ICSI 2019 The 3rd International Conference on Structural Integrity

Incremental finite element delamination model for fibre pull-out tests of elastomer-matrix composites

Siegfried Frankl*, Martin Pletz, Clara Schuecker

Department of Polymer Engineering and Science, Otto Gloeckel-Str. 2, 8700 Leoben, Austria

Abstract

A finite element model is introduced to predict the delamination behaviour of a fibre pull-out test of an elastomer-matrix composite in an incremental approach. A displacement load is monotonically increased and stable crack growth is predicted. The finite element model uses energy differences of models with two different crack lengths to compute the energy release rate of the delamination crack. Parametric studies have been performed to determine the necessary element size and crack size increments, and investigate the effect of friction.

Peer-review under responsibility of the ICSI 2019 organizers.

Keywords: delaminations; fracture mechanics; elastomers; pull-out test; finite element method

1. Introduction

Fibre-reinforced rubber materials are used in various applications such as soft robotics, tires, conveyor belts and hydraulic hoses. While the fibres provide high strength and stiffness in fibre directions, the rubber can allow for high flexibility in other directions. Compared to classical carbon-fibre reinforced polymer laminates, the stiffness difference between fibre and matrix is considerably higher for rubber-based composites. This puts high demands on the fibre-matrix interface, as described for conveyor belts by Fedorko et al. (2014) and for hydraulic hoses by Fedorko et al. (2015).

* Corresponding author. Tel.: +43-3842-402-2505.
E-mail address: siegfried.frankl@unileoben.ac.at

2452-3216
Peer-review under responsibility of the ICSI 2019 organizers.
10.1016/j.prostr.2019.08.008

There are various test methods to measure interfacial strength, such as a simple test for a single fibre described in Hampe et al. (1995) and Zhandarov et al. (2018) but also for fibre bundles, as described in Beter et al. (2019). All those tests feature highly non-uniform interfacial stress fields. Calculating the *interfacial strength* by dividing reached forces by interface area thus does not capture the physics of the problem. To treat the problem, a fracture mechanics approach is more realistic, by using a model that accounts for the stress fields and a delamination crack.

This work proposes a finite element model for such a fibre pull-out test regarding the energy release rate of an interfacial crack and introducing a methodology for an incremental fibre-matrix delamination. The setup of the model is based on the pull-out test of Beter et al. (2019). There, a fibre bundle is pulled out of a rectangular rubber block which is held by a specimen holder. The load is applied as a monotonically increasing displacement, causing a stable crack growth with increasing applied displacement.

2. Modeling

2.1. Fibre pull-out model

An implicit finite element (FE) model for the test setup of the fibre bundle pull-out test from Beter et al. (2019) is developed using the commercial FE code ABAQUS (2014). The test is modelled as an axial symmetric model as shown in Fig. 1, where the geometric parameters of the model are defined. As indicated, the left end of the fibre is pulled horizontally to the left with a displacement u, causing the rubber part to contact the rigid punch, which is fixed in all directions. There can be an initial delamination between fibre bundle and rubber part with the delamination length a. Between the punch, the rubber part and the crack faces, contact is modelled with a penalty formulation. The tangential contact uses a Coulomb friction law with a friction coefficient of μ_1 and μ_2 for punch-rubber and crack faces contact, respectively. The deformable bodies use four-node axisymmetric quadrilateral elements with hybrid formulation. The model uses nonlinear geometry to account for geometric and material nonlinearities.

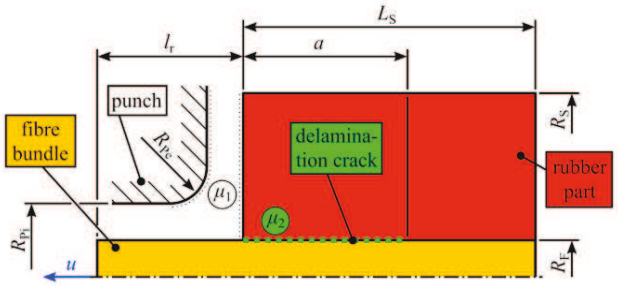

Fig. 1: Setup of the axial-symmetric fibre pull-out model.

The fibre bundle and the rubber part are modelled as one part with shared nodes but different material models. The fibre bundle uses homogenized isotropic material properties with linear elastic behaviour. As in Beter et al. (2019), an E-glass fibre bundle with the classification EC9-68x5t0 of CS Interglas AG is used, a Young's modulus is taken from the corresponding datasheet as 33 GPa. For the homogenized fibre bundle, a Poisson's ratio of 0.3 is assumed. A hyperelastic material model with the Yeoh-form is used to describe the deformation of rubber part, which in Beter et al. (2019) consists of silicone rubber. The Yeoh parameters are fitted to a uniaxial test curve for a similar silicone rubber material from Hoffmann (2012) in ABAQUS, setting the Poisson's ratio for the fit to 0.4. Those Yeoh parameters are given in Table 1.

Table 2 shows the parameters chosen in the model to represent the geometry of the test from Beter et al. (2019). Concerning the friction coefficients and the fracture energy of the interface, typical values are assumed. In addition, the two friction coefficients were assumed to be the same. These parameters are used as values in the model, some of which will be varied in the results section.

Table 1: Yeoh parameters for the rubber part

C_{10} [MPa]	C_{20} [MPa]	C_{30} [MPa]	D_1 [1/MPa]	D_2 [1/MPa]	D_3 [1/MPa]
0.2365	5.778E-02	7.316E-02	0.906	0	0

Table 2. Model parameters

Description	Symbol	Value	Unit
Fibre radius	R_F	0.25	mm
Outer radius silicone part	R_S	4	mm
Length silicone part	L_S	10	mm
Length to retrain	l_r	5	mm
Punch inner radius	R_Pi	0.4	mm
Punch edge radius	R_Pe	0.1	mm
Friction coeff. rubber / punch	μ_1	0.5	1
Friction coeff. crack faces	μ_2		
Mesh size	m	0.1	mm
Initial crack length	a_0	0.25	mm
Fracture energy	G_c	500	J/m^2

2.2. Evaluation of energy release rate

At interfaces and for delamination cracks, the classical *K*-concept with a stress intensity factor is not valid. However, the more general energy release rate concept can be used. The energy release rate G is defined as the change of the energy which is released through crack growth (change of crack face area A_crack) of an existing crack. This energy release rate G consists of the external work W_e, the strain energy U (negative) and the frictional dissipation W_f (negative) as used by Sun and Davidson (2006):

$$G = \frac{\partial}{\partial A_\mathrm{crack}} [W_\mathrm{e} - (U + W_\mathrm{f})] \tag{1}$$

The derivative can be replaced by a finite difference, where $\Delta U = U(a+\Delta a) - U(a)$ and similar for W_e and W_f. If the same displacement is applied for both crack lengths, the change in the external work W_e becomes zero and G can be written with $\Delta A_\mathrm{crack} = 2\pi R_\mathrm{f} \Delta a$ as:

$$G = -\frac{1}{4\pi R_F} \left[\frac{\Delta U}{\Delta a} + \frac{\Delta W_f}{\Delta a}\right] \tag{2}$$

The values needed for $U(a)$, $U(a+\Delta a)$, $W_\mathrm{f}(a)$ and $W_\mathrm{f}(a+\Delta a)$ are determined from FE models with according crack lengths. This assumes that running the model with a crack length of $a+\Delta a$ yields the same energies as a model that has initially a crack length of a and then the crack is extended by Δa. This path-independency is not necessarily valid if friction is not negligible in the model. This simplification will be discussed in section 3.1, where typical values of U and W_f are shown. When the computed energy release rate G reaches its critical value, the fracture energy G_c, the crack propagates and keeps propagating until G of the growing crack drops below G_c or full separation is reached.

2.3. Incremental crack propagation model

To predict the growth of the delamination crack, an incremental crack propagation model is introduced. It uses the FE model described in section 2.1 and the evaluation of the G values described in section 2.2. The model starts with an existing initial crack with the length $a = a_0$. Then, the displacement u is applied stepwise in Δu increments

and after each Δu, the energy release rate G is computed according to equation 2 from the FE model of the current displacement load u for the current crack length a as well as $a + \Delta a$. The crack propagates by Δa if the G value is higher than G_c. The model checks for further crack propagation, until $G < G_c$ or the maximum crack length a_{max} is reached. Then, the model runs for $u + \Delta u$ with the updated crack length.

Fig. 2a shows this procedure by plotting the strain energy plus the frictional dissipation ($U + W_f$) over the displacement u. Applying an initial displacement Δu, the difference between the $U + W_f$ curves for the crack lengths a_0 and $a_0 + \Delta a$ is used to compute G according to equation 2. Since G is below G_c, the crack is not extended and u is increased by Δu. For a value of $u = 2\Delta u$, G is computed in a similar way and is above G_c. The crack thus grows by Δa, but G for $a + \Delta a$, is too small for the crack to grow another Δa. So u is increased again, and it takes three Δu steps until the crack grows again by Δa. These Δu and Δa steps are shown in Fig. 2b. Fig. 2c shows the resulting force-displacement curve.

This concept can also be employed with more complex crack growth criteria or even competing crack growth.

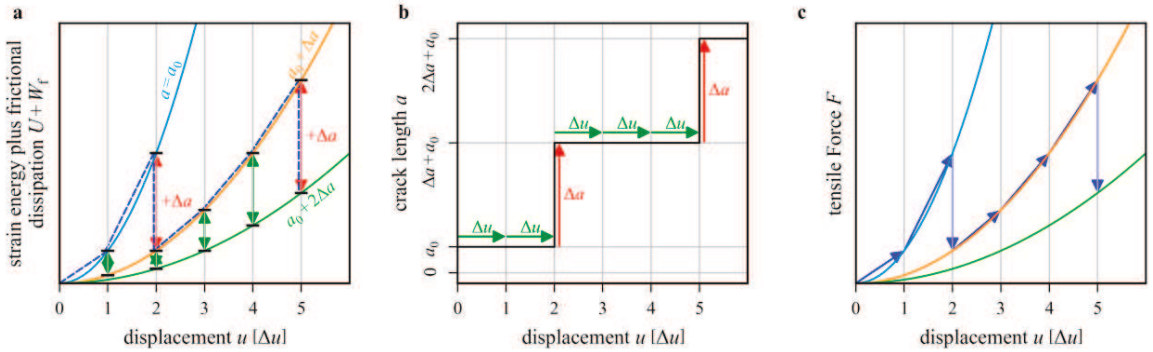

Fig. 2: Scheme of the iterative concept with (a) the strain energy U and the frictional dissipation W_f, (b) the crack length a and (c) the tensile force F plotted over the applied displacement u.

3. Results and discussion

3.1. Study of necessary mesh size in FE model

Fig. 3 shows a contour plot of the von-Mises stress, σ_{mis}, in the model with a crack length of $a = 4$ mm, an applied displacement of $u = 0.4$ mm and a mesh size of $m = 0.1$ mm. The end of the fibre bundle is pulled to the left, and the rubber part is pressed against the rigid punch. Severe deformations can be seen at the crack tip, with maximum σ_{mis} values of 8.5 MPa. These maximum stresses of course highly depend on the mesh-size. Close to the rigid punch, the crack faces are pressed together.

For computing stiffness and energies, it must be ensured that the mesh size has no influence on the energy output of the simulation. To investigate this, the mesh size m is varied between 0.025 mm and 0.6 mm in 8 steps with a logarithmic distribution. In general, the necessary mesh size has to be derived for all crack lengths. In this section, three representative crack lengths of $a = 0.25$ mm, 1 mm and 4 mm are used. For the simulations, the parameters from Table 2 are used and a displacement at the fibre bundle end of $u = 0.4$ mm is applied.

Fig. 4 shows how the external work W_e, the strain energy U, the frictional dissipation W_f, and the tensile force F change with varied mesh size m. Since those values strongly depend on the crack length, they are shown in a normalized way, i.e. divided by their value for an m value of 0.025 mm. Table 3 shows their absolute values for all three crack lengths. It can be seen that the W_f value lays two orders of magnitudes below W_e and U. As mentioned in section 2.2, the path-dependence of the crack opening is not regarded in the model, i.e. the W_f values might not be very accurate. This is indicated in the W_f results, since W_f with a value of 2.09 mJ for a crack length of 4 mm is smaller than $W_f = 6.22$ mJ for a crack length of 1 mm. These unrealistic changes, however, are considerably smaller

than the changes in the U values between different crack lengths and therefore do not alter the predictions about crack growth and in the following, the W_f value is disregarded in the computation of G.

A mesh size of 0.1 mm is chosen for the following models, because U and F reached already the same values as for smaller m. The m value of 0.1 mm is indicated in Fig. 3 with a red, dashed line.

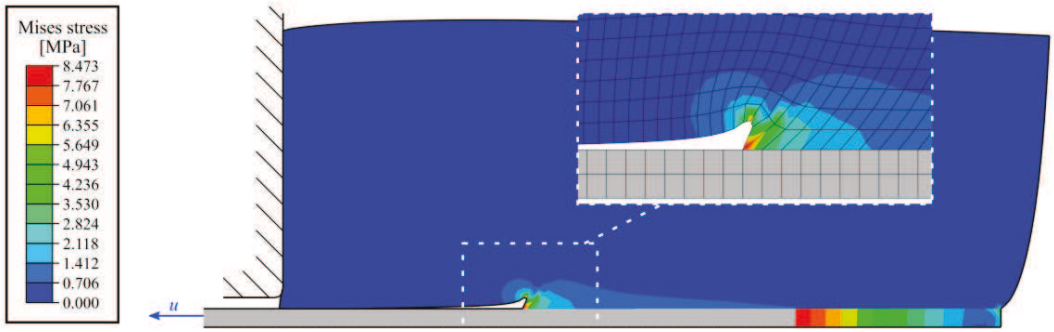

Fig. 3: Contour plot of the von-Mises stresses σ_{mis} in the model with a crack length of 4 mm, an applied displacement of 0.4 mm and a mesh size of 0.1 mm. The stress limits are chosen to see the maximum σ_{mis} of 8.5 MPa in the rubber. Grey regions have σ_{mis} values above 8.5 MPa.

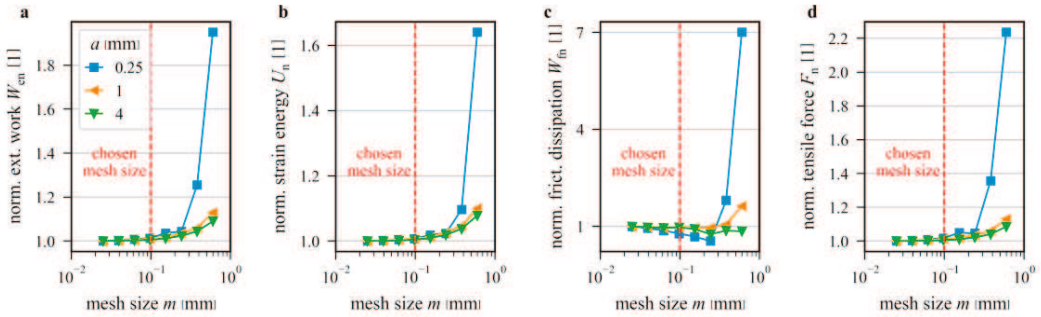

Fig. 4: Results of the normalized values of (a) the external work W_e, (b) the strain energy U, (c) the frictional dissipation W_f and (d) the tensile force F plotted over the mesh size m. The suitable mesh size is chosen as 0.1 mm and denoted in the figers with a dashed red line.

Table 3: Energies and forces for the calculation with the mesh size of 0.1 mm and a displacement load of 0.4 mm

Crack length a [mm]	External work W_e [J]	Strain energy U [J]	Frictional dissipation W_f [J]	Tensile force F [N]
0.25	9.866E-04	9.826E-04	2.262E-06	5.986
1	7.319E-04	7.243E-04	6.221E-06	3.824
4	4.254E-04	4.231E-04	2.087E-06	2.167

3.2. Incremental crack propagation model

3.2.1. Effect of crack growth increment Δa

Every time a crack is propagated by Δa, there is a kink in the energy-displacement and also force-displacement curve. Choosing smaller Δa values obviously increases the number of those kinks and makes the curve smoother. To investigate the influence of crack length increment Δa, two values of Δa = 0.5 mm and Δa = 1 mm and the model parameters from Table 2 are used to propagate a delamination crack with an initial crack length a_0 of 0.25 mm. The main interest of these models is to see if lower Δa values also shift the crack propagation curves.

Fig. 5 shows results of (a) the strain energy U, (b) the crack length a, and (c) the tensile Force F over displacement u for the two different Δa values up to a crack length of 9 mm. A smaller Δa brings better resolved

results but has no influence on the trend of the curves. However, there is a clear dependency of the maximum tensile forces F on Δa, so for an accurate calculation of maximum F values, Δa has to be chosen even smaller than 0.5 mm.

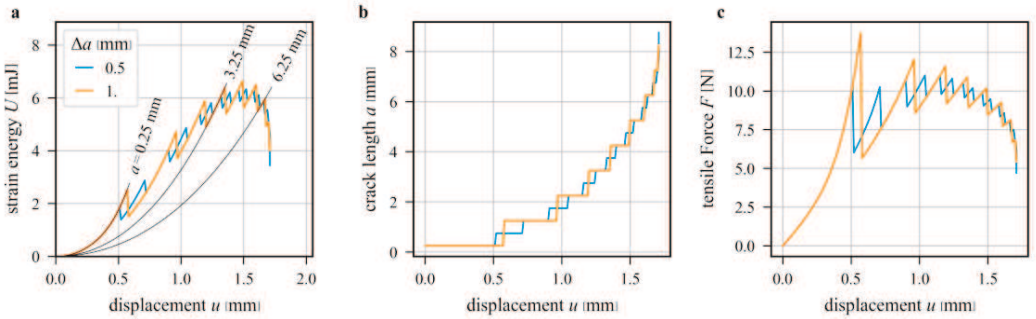

Fig. 5: Results for the incremental crack propagation model with different crack length increments Δa showing (a) the strain energy U, (b) the crack length a and (c) the tensile force F plotted over the applied displacement u.

3.2.2. Effect of fracture energy

To examine the effects of a change in fracture energy on the crack propagation model results, three fracture energy G_c values of 300 J/m^2, 500 J/m^2 and 700 J/m^2 are used in the simulations with a crack increment of 1 mm.

Fig. 6 shows results of (a) the strain energy U, (b) the crack length a and (c) the tensile Force F over the displacement u for the three G_c values up to a crack length of 9 mm. Obviously, higher G_c values shift the crack growth towards higher energy values and higher displacements u. In addition, higher force values are reached, and force-displacement curves from Fig. 6c could be compared to test curves to estimate G_c values for the rubber-fibre bundle interface.

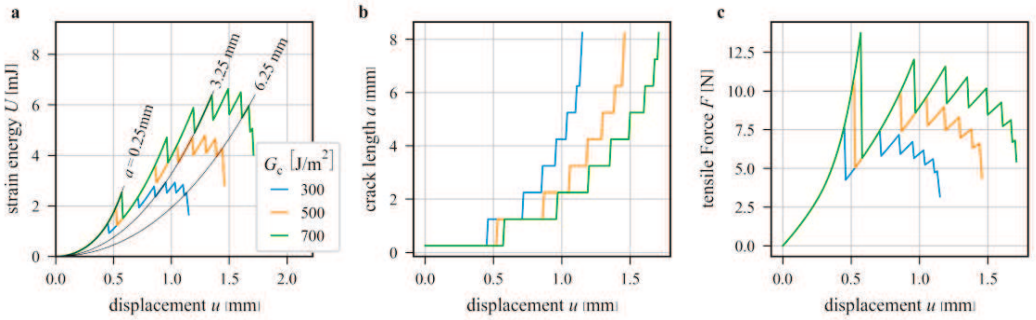

Fig. 6: Results for the incremental crack propagation model with different fracture energies G_c showing (a) the strain energy U, (b) the crack length a and (c) the tensile force F plotted over the applied displacement u.

3.2.3. Effect of friction coefficients

In section 3.1, it has already been stated that the frictional dissipation W_f is much smaller than the strain energy U and was therefore not regarded in the computation of the energy release rate G. To investigate how the friction influences the strain energy in the model and thus the G values, the incremental crack propagation model is calculated with the default parameters from Table 2 with the friction coefficient μ ($\mu_1 = \mu_2$) set to 0.3, 0.5 and 0.7. For the fracture energy G_c, a value of 700 J/m^2 is chosen. The initial crack length is 0.25 mm.

Fig. 7 shows the results of the incremental crack propagation model for the three friction coefficients. A slight shift to earlier crack propagation is seen for higher friction coefficients. This is because the crack is closed in the region close to the punch (see Fig. 3), where different friction coefficients can influence stress fields.

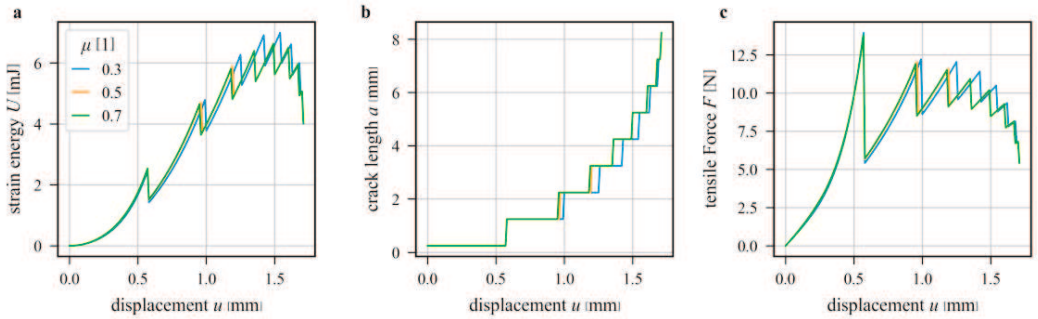

Fig. 7: Results for the incremental crack propagation model with different friction coefficients μ_1, μ_2 showing (a) the strain energy U, (b) the crack length a and (c) the tensile force F plotted over the applied displacement u.

4. Conclusions

A model for predicting incremental crack growth of a fibre bundle pulled out of a rubber block was developed. The energy release rate G for a delamination crack is computed from energetic consideration of two models with different crack lengths. A mesh size that is sufficiently small for an accurate computation of G values has been identified. Computation times for that mesh size amount to about 2 minutes on a common desktop computer. From looking at the energy values, the contribution of the frictional dissipation for the calculation of G can be disregarded.

For the incremental crack propagation model, previously run finite element models with various crack lengths were used to predict how the crack propagates with an applied displacement load. Depending on geometric parameters, material properties and fracture energy G_c, force-displacement curves can be computed for the fibre pull-out test. In future work, the G_c values will be fitted to test curves and the method for computing delamination crack growth can be extended to realistic applications with more complex geometry and competing damage modes, for example the possibility for the crack to deflect into the rubber part.

Acknowledgements

The funding of the research by the Austrian Research Promotion Agency, FFG, through the Project BeltSim within the Bridge 1 program is gratefully acknowledged.

References

Abaqus (Ed.), 2014. ABAQUS Theory Guide, 6.14, Dassault Systèms, Providence, RI, USA.

Beter, J., Schrittesser, B., Fuchs Peter, 2019. Investigation of adhesion properties in load coupling applications for flexible composites. 12th International Conference on Composite Science and Technology, Sorrento, Italy.

Fedorko, G., Molnar, V., Dovica, M., Toth, T., Fabianova, J., 2015. Failure analysis of irreversible changes in the construction of the damaged rubber hoses. Engineering Failure Analysis 58, 31–43.

Fedorko, G., Molnar, V., Grincova, A., Dovica, M., Toth, T., Husakova, N., Taraba, V., Kelemen, M., 2014. Failure analysis of irreversible changes in the construction of rubber–textile conveyor belt damaged by sharp-edge material impact. Engineering Failure Analysis 39, 135–148.

Hampe, A., Kalinka, G., Meretz, S., Schulz, E., 1995. An advanced equipment for single-fibre pull-out test designed to monitor the fracture process. Composites 26, 40–46.

Hoffmann, J., 2012. Charakterisierung faserverstärkter Elastomere für formvariable Strukturflächen. Dissertation, München, 165 pp.

Sun, X., Davidson, B.D., 2006. Numerical evaluation of the effects of friction and geometric nonlinearities on the energy release rate in three- and four-point bend end-notched flexure tests. Engineering Fracture Mechanics 73, 1343–1361.

Zhandarov, S., Mäder, E., Scheffler, C., Kalinka, G., Poitzsch, C., Fliescher, S., 2018. Investigation of interfacial strength parameters in polymer matrix composites: Compatibility and reproducibility. Advanced Industrial and Engineering Polymer Research 1, 82–92.

Paper D

Improved concept for iterative crack propagation using configurational forces for targeted angle correction

Authors: Frankl, Siegfried Martin
Pletz, Martin
Schuecker, Clara

Engineering Fracture Mechanics
DOI: 10.1016/j.engfracmech.2022.108403

Engineering Fracture Mechanics 266 (2022) 108403

Contents lists available at ScienceDirect

Engineering Fracture Mechanics

journal homepage: www.elsevier.com/locate/engfracmech

Improved concept for iterative crack propagation using configurational forces for targeted angle correction

Siegfried Martin Frankl, Martin Pletz *, Clara Schuecker

Designing Plastics and Composite Materials, Department of Polymer Engineering and Science, Montanuniversitaet Leoben, Austria

ARTICLE INFO

MSC:
00-01
99-00

Keywords:
Fracture mechanics
Configurational forces
Incremental crack propagation
Finite element method

ABSTRACT

In many applications, fracture mechanics is indispensable in predicting structural failure. In this paper, a concept for predicting discrete crack paths according to the criterion of maximum energy release rate, which uses the finite element method, is presented. Within existing approaches to determine the incremental crack propagation direction, on the one hand, the information of the current crack is used in explicit approaches, leading to inaccuracies. On the other hand, the information of introduced virtual cracks can be used in implicit approaches, with the required number of virtual cracks determining the computational effort. This work introduces a 2D concept for quasi-static crack propagation in elastic materials and that uses configurational forces to estimate an angle error of a virtual crack increment; the concept uses this angle error in an iterative crack correction. The concept is evaluated using a simplified model for one crack propagation increment and a three-point bending model that contains holes for predicting crack paths in combination with the incremental crack propagation method. The results are compared with those of existing explicit and implicit crack propagation direction concepts, as well as experimental results. It is shown that the presented concept fulfils the concept for maximum energy release rate as accurately as a computationally expensive implicit concept, while the computational effort of the proposed concept is close to fast explicit concepts.

1. Introduction

Fracture mechanics can be used to understand, predict, and prevent failure of components by evaluating whether and in which direction the crack propagates; the main concepts for crack growth are based on Griffith [2], Irwin [3], and Rice [4]. To assess whether a crack is propagating, a crack-driving force is computed in various ways and compared with the resistance of the material against crack growth. Additionally, there are concepts to predict the crack propagation direction, such as the maximum tangential stress concept of Erdogan and Sih [5], the maximum shear stress concept proposed by Otsuka et al. [6], and the Maximum Energy Release Rate (MERR) concept as a generalisation of the Griffith concept. Also, the assumption for crack propagation in the direction of pure mode I loading at the crack tip is used, which is supported by numerous experiments, see, for example, Broberg [7]. Some concepts like the vector J-Integral used by Ma and Korsunsky [8] and the configurational forces concept introduced by Eshelby [9] compute the crack driving force as a vector, which allows for predicting the crack propagation direction. The validity of crack propagation direction concepts depends on the application (load situation and material properties). Repeated crack propagation yields the crack path. Hence, the use of a suitable concept to predict a crack path is of great importance.

Many scientists have numerically determined crack paths using the Finite Element Method (FEM). One option of doing so is incremental crack propagation, where a crack path consists of a series of straight crack increments. The available concepts that

* Corresponding author.
E-mail address: martin.pletz@unileoben.ac.at (M. Pletz).

https://doi.org/10.1016/j.engfracmech.2022.108403
Received 3 September 2021; Received in revised form 19 January 2022; Accepted 16 March 2022
Available online 26 March 2022

Nomenclature

a	Crack length
Δa	Crack increment length
$\mathbf{C}$	Eshelby stress tensor
c_x, c_y	x and y coordinates of the crack
D	Hole diameter
d_c	Radius of rigid coupling
E	Young's modulus
ΔE	Strain energy change due to crack propagation
E_{glob}	Global energy
$\mathbf{f}$	Configurational force
f_x, f_y	x and y component of the vector $\mathbf{f}$
$\mathbf{f}^j$	Nodal configurational force of node j
$\mathbf{f}_{tip}$	Crack tip configurational force
$f_{tip}^{\parallel}$, $f_{tip}^{\perp}$	Parallel and perpendicular component of the crack tip configurational force $\mathbf{f}_{tip}$
G	Evaluated energy release rate
G_c	Critical energy release rate
H, h_1, h_2	Height
$\mathbf{k}$	Geometry change vector
n_c	Number of virtual cracks
n_{epr}	Number of elements per element row
n_{er}	Number of circular element rows
P^j	Arbitrary FEM node
$\mathbf{p}^j$	Position vector of node P^j
p_x^j, p_y^j	x and y component of the vector $\mathbf{p}^j$
$\tilde{\mathbf{p}}^j$	Rotated position vector of P^j
R_Ω	Radius of the evaluation region
$\mathbf{t}$	Crack propagation vector
t	Thickness of the plate
u	Vertical displacement
Δu	Displacement increment
u_i	Displacement for step i
W, w_1, w_2	Width
x_c, y_c	x and y coordinates of the local coordinate system
α	Angle of the starting crack
ν	Poisson's ratio
φ	Crack angle of the virtual crack
φ_c	Crack correction angle
φ_{err}	Permitted angle error
φ_p	Crack propagation angle
$\tilde{\varphi}$	Rotation angle of the virtual crack
Ω	Volume
Ω_{TAC}	Volume for the TAC concept

use only the information of the current crack to predict crack growth are commonly referred to as *explicit concepts*. Alternatively, the information of introduced virtual cracks can be used to predict crack growth in *implicit concepts*. This means that the crack is extended by a virtual crack increment in the model, and the results of this virtual crack are used to evaluate energy release rates and crack propagation directions. Hellen [10] found the direction of MERR by introducing various virtual crack extensions (implicit concept). Ma and Korsunsky [8] used the vector J-Integral in an explicit concept to find the direction of MERR. In recent decades, the configurational forces concept has been used to predict crack propagation [11]. Configurational forces are suitable for predicting crack paths because of their definition as an energy gradient because of a geometry change and are generally applicable due to their material-independent formulation. The configurational force vector at the crack tip of the current crack is used in explicit concepts for computing the crack propagation direction and energy release rate [12–14], which also works for elastic–plastic materials [15–17]. Implicit concepts use the configurational force vector of the crack tip of virtual cracks [13,18,19], where hyperelastic and

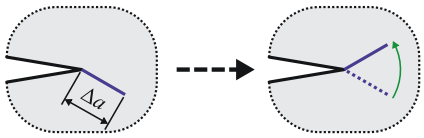

Fig. 1. Correction of the direction of the virtual crack increment, whereby the virtual crack consists of the current crack that is propagated by a crack increment Δa.

viscoelastic material behaviour can also be considered. A comparison between explicit and implicit concepts is given by Brouzoulis et al. [13], where the implicit configurational force-based concept converges towards the solution of the MERR determined by Hellen [10]. The explicit configurational force-based concept is very efficient, but it lacks in accuracy compared with the solution for using MERR for large crack increments. Implicit concepts are more accurate, but they lack in efficiency because of the number of computations necessary for one crack propagation. No work has been found by the authors so far aims at keeping the accuracy of the implicit concepts while improving the efficiency of crack path prediction.

In the current paper, the configurational forces occurring at an introduced virtual crack are used to estimate the direction error of the virtual crack increment for repeated direction correction, which we refer to the Targeted Angle Correction (TAC) concept. To compute the direction error from configurational forces, the change in strain energy is derived for a rotation of the virtual crack increment. The direction of the virtual crack increment is iteratively corrected to determine the crack propagation direction for MERR. The TAC concept is used in a simplified and three-point bending model. In the simplified model, a single crack propagation is investigated, where the TAC response is examined and compared with other explicit and implicit propagation concepts for a wide range of crack angles. The crack paths are examined in the three-point bending model. The crack path results of the TAC concept are compared with other explicit and implicit crack propagation concepts and are validated through experimental results.

2. Methods

To predict a crack path, it is necessary to evaluate the crack propagation direction at every crack tip position of a growing crack. In this section, some existing concepts for predicting the crack propagation direction are explained, which are used for comparison purposes in the current work, and a new concept is presented. In the new TAC concept, the *current* crack is propagated by a crack increment Δa to give the *virtual* crack, which is similar to an iterative concept. The virtual crack direction can then be corrected to fulfil the crack propagation criterion of MERR using the concept of configurational forces (see Fig. 1). The TAC concept is implemented in FEM, where the concept is examined and evaluated in two FEM models.

2.1. Crack propagation concepts

To predict the crack propagation direction for an existing crack, various concepts from the literature can be used. These concepts can be divided into two groups: (a) explicit concepts that use information of the *current crack* and (b) implicit concepts where the crack is virtually propagated (*virtual crack*); this information is used to predict the crack propagation direction. Implicit concepts find the crack propagation direction either by testing a set of predefined propagation directions or through repeated correction of the crack propagation direction. The TAC concept proposed in the current work is one of the latter.

2.1.1. Explicit crack propagation

Explicit crack propagation concepts use the current crack to evaluate the crack propagation direction. The configurational force at the crack tip, $\mathbf{f}_{\text{tip}}$, is used as the crack-driving force that determines the crack propagation direction, as in Guo and Li [14]. Fig. 2(a) and (c) illustrate the concept of configurational force-based explicit crack propagation based on $\mathbf{f}_{\text{tip}}$ of the current crack. The crack is propagated in the opposite direction of $\mathbf{f}_{\text{tip}}$. The crack propagation angle φ_{p}, as defined in Fig. 2(c), is given by

$$\varphi_{\text{p}} = \arctan\left(\frac{f_{\text{tip,y}}}{f_{\text{tip,x}}}\right), \tag{1}$$

where $f_{\text{tip,x}}$ and $f_{\text{tip,y}}$ are the components of $\mathbf{f}_{\text{tip}}$ in the x and y directions, respectively. The configurational force $\mathbf{f}$ states that moving the evaluated region in the opposite direction of $\mathbf{f}$ gives the highest energy dissipation. However, the geometry resulting from moving the evaluation region does not properly model a propagating crack, as shown in Fig. 2(b). Using $\mathbf{f}$ for the crack propagation in the explicit concept, as illustrated in Fig. 2(c), then implies that the physical meaning of configurational forces is captured only in an approximated way. To avoid this issue, the TAC concept is introduced in Section 2.2.

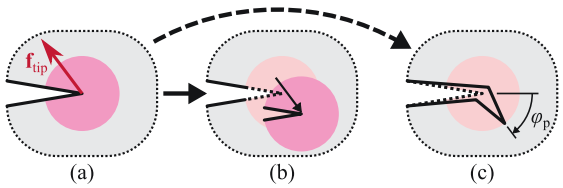

Fig. 2. (a) Crack tip with the configurational force $\mathbf{f}_{tip}$, (b) physical meaning of the $\mathbf{f}_{tip}$, and (c) crack propagation in the opposite direction of the configurational force $\mathbf{f}_{tip}$.

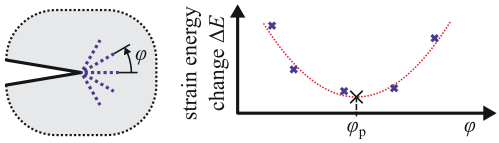

Fig. 3. Range of virtual cracks with the crack angle φ and their associated strain energy change ΔE. The minimum of interpolated ΔE is marked by x and yields the predicted angle of crack propagation.

2.1.2. Implicit crack propagation

With explicit crack propagation concepts the current crack is used to evaluate the crack propagation direction, implicit concepts use virtual cracks for an evaluation of the crack propagation direction. In this section, two existing approaches are presented. The crack propagation criterion of MERR follows the principle of maximum energy dissipation [20,21]. This thermodynamics-based criterion means that the crack propagates in the direction in which the strain energy change due to crack growth, ΔE, has a minimum [10] (see Fig. 3). The strain energy change ΔE is given by

$$\Delta E = E^{\text{virt}}_{\text{glob}} - E^{0}_{\text{glob}}, \tag{2}$$

where E^{0}_{glob} is the strain energy of the whole model before crack propagation and $E^{\text{virt}}_{\text{glob}}$ is the strain energy of the whole model after virtual crack propagation. In this work, it is assumed that only one minimum of ΔE exists. The crack propagation direction can be found by introducing a range of virtual cracks and evaluating ΔE for them. The crack propagation direction is determined by selecting the most suitable virtual crack or by performing an interpolation of the ΔE values for different angles of the virtual crack increment, as shown in Fig. 3. In the current work, the propagation direction for MERR is found by introducing n_c virtual cracks in a range of equidistant angles of the virtual crack increment φ_i. For each virtual crack, the ΔE_i is computed and interpolated using a quadratic polynomial to find the minimum value that gives the crack propagation direction φ_p. The polynomial is fitted using the least squares method. Additionally, instead of minimising ΔE, the absolute value of the perpendicular component of the configurational force of the crack tip, $|f^{\perp}_{tip}|$ can be minimised. A vanishing $|f^{\perp}_{tip}|$ yields pure mode-I loading at the crack tip [13].

Alternatively, the crack propagation direction can be found by an iterative approach, where starting from a current crack, a virtual crack is introduced. The initial virtual crack direction is evaluated from the configurational force at the current crack tip. The angle of this virtual crack is iteratively corrected by the crack correction angle φ_c, as shown in Fig. 4. The information of previous virtual cracks or introduced additional virtual cracks are used to determine φ_c. With each iteration, the direction of the virtual crack increment approaches the crack propagation direction φ_p based on the crack propagation concept, and the correction angle φ_c decreases. The crack propagation direction φ_p is found if φ_c becomes zero and the current crack is updated by the virtual crack. Due to the numerical effects caused by using FEM, φ_c cannot become completely zero, so a permitted angle error φ_{err} is introduced. Özenç et al. [19] presented such an iterative approach, where additional virtual cracks are introduced in each increment to form a gradient that is used in an Newton–Raphson approach to find the crack propagation direction. A more efficient way to compute the crack correction angle is introduced in the next section.

2.2. Targeted angle correction (TAC) concept

In this section, the iterative implicit TAC crack propagation concept is introduced, where the crack correction angle φ_c is computed in a more efficient way. By using a constant length of the virtual crack increment Δa, φ_c can be computed from configurational forces without the need to introduce additional virtual cracks to form a gradient. The crack correction angle φ_c can be used to assess the latest virtual crack propagation direction and to quantitatively correct the angle of the virtual crack increment (see Fig. 4).

To determine the crack correction angle φ_c from configurational forces, the physical meaning of a configurational force is considered. The configurational force evaluated in a circular region around the crack tip is shown in Fig. 5(a). The configurational force can be understood as an energy gradient due to a geometry change. For a decrease in the strain energy, the geometry enclosed by the region has to move in the opposite direction of the configurational force (see Fig. 5(b)). As mentioned before, the resulting

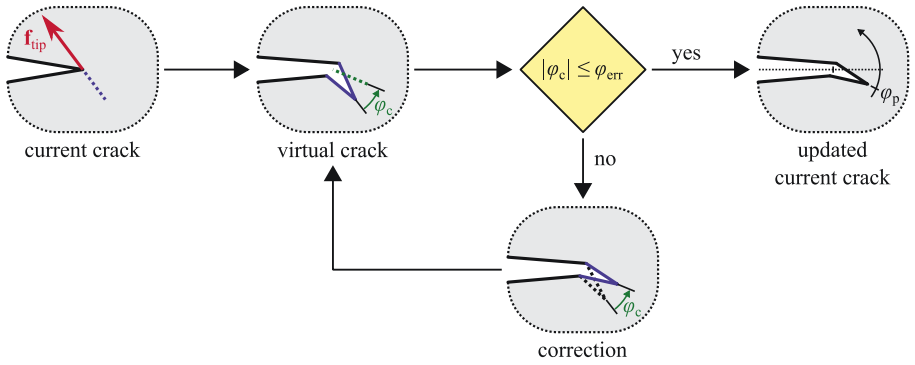

Fig. 4. Flowchart of the algorithm for an increment of crack growth with iterative crack correction. Starting from the current crack with the crack driving force $\mathbf{f}_{tip}$, a virtual crack is introduced. For the virtual crack, the correction angle φ_c is computed. If the absolute of φ_c is larger than the permitted angle error φ_{err}, the crack propagation direction is corrected and a new virtual crack is introduced. Otherwise, the virtual crack is regarded as the updated current crack.

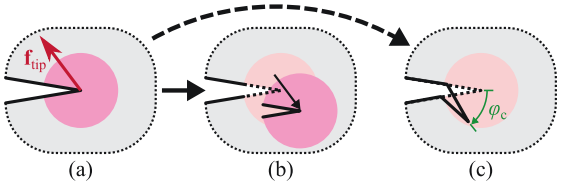

Fig. 5. (a) Crack tip with the configurational force $\mathbf{f}_{tip}$, (b) physical meaning of the $\mathbf{f}_{tip}$, and (c) crack correction because of the crack correction angle φ_c.

geometry does not make sense for a propagating crack. To avoid this issue, a crack correction is introduced (see Fig. 5(c)). This evaluation approach based on configurational forces is introduced below, where the crack correction angle φ_c is derived.

This work uses nodal configurational forces, which are evaluated in an FEM mesh. The configurational force $\mathbf{f}$ is given by

$$\mathbf{f} = -\operatorname{div}\mathbf{C}, \tag{3}$$

where $\mathbf{C}$ is the Eshelby stress tensor [9]. The nodal configurational forces are determined as described in Section 2.3.1. Because of the formulation used, a nodal configurational force vector is computed at all nodes, not only at the crack tip. Nonzero nodal configurational forces also occur at the nodes of the crack faces (see Fig. 7), which appear as reaction forces because of the constrained boundary in the reference configuration. As a consequence of the law of conservation, the nodal configurational forces inside a homogeneous material are zero, except for discretisation effects.

Fig. 6 shows a virtual crack with its local coordinate system (x_c, y_c). The origin of this coordinate system lies at the current crack tip, and the x_c axis is orientated in the direction of the virtual crack increment, where $\mathbf{t}$ is the crack propagation vector from the current crack tip to the virtual crack tip. For one arbitrary node P^j with its position vector $\mathbf{p}^j$, the nodal configurational force vector $\mathbf{f}^j$ is drawn in Fig. 6. For a sufficiently fine mesh, the change of strain energy ΔE can be approximated as a sum of the nodal contributions in the volume Ω

$$\Delta E = \sum_{j\in\Omega} \left(\mathbf{f}^j\right)^{\mathrm{T}} \mathbf{k}^j, \tag{4}$$

where $\mathbf{k}^j$ is the geometry change vector. The volume Ω includes all geometries that are changed (region of the virtual crack increment) and excludes all geometries that remain constant (such as the current crack flanks).

To compute the crack correction angle φ_c, ΔE is written as a function of the change of the angle of the virtual crack increment $\tilde{\varphi}$. The rotated position vector $\tilde{\mathbf{p}}^j$ is defined as $\mathbf{p}^j$ rotated by $\tilde{\varphi}$. Therefore, the geometry change vector $\mathbf{k}^j = \tilde{\mathbf{p}}^j - \mathbf{p}^j$ for a constant crack increment Δa is given by

$$\mathbf{k}^j = \begin{bmatrix} \cos\tilde{\varphi} & -\sin\tilde{\varphi} \\ \sin\tilde{\varphi} & \cos\tilde{\varphi} \end{bmatrix} \mathbf{p}^j - \mathbf{p}^j = \begin{bmatrix} \cos\tilde{\varphi} - 1 & -\sin\tilde{\varphi} \\ \sin\tilde{\varphi} & \cos\tilde{\varphi} - 1 \end{bmatrix} \mathbf{p}^j. \tag{5}$$

To find the minimum of ΔE, Eq. (5) is inserted in Eq. (4) and derived by $\tilde{\varphi}$:

$$\frac{\partial \Delta E}{\partial \tilde{\varphi}} = \sum_{i\in\Omega} \left(\mathbf{f}^j\right)^{\mathrm{T}} \begin{bmatrix} -\sin\tilde{\varphi} & -\cos\tilde{\varphi} \\ \cos\tilde{\varphi} & -\sin\tilde{\varphi} \end{bmatrix} \mathbf{p}^j. \tag{6}$$

When Eq. (6) is set to zero, $\tilde{\varphi}$ equals the crack correction angle φ_c:

$$\sum_{j\in\Omega} -\mathrm{p}_x^j \mathrm{f}_x^j \sin\varphi_c - \mathrm{p}_y^j \mathrm{f}_x^j \cos\varphi_c + \mathrm{p}_x^j \mathrm{f}_y^j \cos\varphi_c - \mathrm{p}_y^j \mathrm{f}_y^j \sin\varphi_c = 0, \tag{7}$$

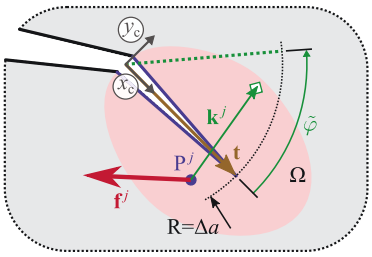

Fig. 6. Virtual crack increment (blue lines) with a length of Δa. The origin of the coordinate system is defined at the start of the virtual crack increment, and x_c is defined in the direction of the virtual crack increment. For one arbitrary FEM node P^j, the nodal configurational force $\mathbf{f}^j$ is drawn. The vector $\mathbf{k}^j$ defines the change of the node point position because of a rotation of the virtual crack increment by an angle $\tilde{\varphi}$ in the local coordinate system. The volume Ω only includes the geometry changed by the rotation.

where the subscripts x and y mark the components of the vectors $\mathbf{p}^i$ and $\mathbf{f}^i$, respectively. Because φ_c is constant over the whole volume Ω, Eq. (7) can be rearranged as follows:

$$\frac{\sin\varphi_c}{\cos\varphi_c} = \frac{\sum\limits_{j\in\Omega} \mathrm{p}_x^j\,\mathrm{f}_y^j - \mathrm{p}_y^j\,\mathrm{f}_x^j}{\sum\limits_{j\in\Omega} \mathrm{p}_x^j\,\mathrm{f}_x^j + \mathrm{p}_y^j\,\mathrm{f}_y^j} = \frac{\sum\limits_{j\in\Omega} \left(\mathbf{p}^j\right)^{\mathrm{T}} \begin{bmatrix} 0 & 1 \\ -1 & 0 \end{bmatrix} \mathbf{f}^j}{\sum\limits_{j\in\Omega} \left(\mathbf{p}^j\right)^{\mathrm{T}} \mathbf{f}^j}\,. \tag{8}$$

The crack correction angle φ_c results from Eq. (8) as

$$\varphi_c = \arctan\left(\frac{\sum\limits_{j\in\Omega} \left(\mathbf{p}^j\right)^{\mathrm{T}} \begin{bmatrix} 0 & 1 \\ -1 & 0 \end{bmatrix} \mathbf{f}^j}{\sum\limits_{j\in\Omega} \left(\mathbf{p}^j\right)^{\mathrm{T}} \mathbf{f}^j} \right). \tag{9}$$

To speed up the convergence of the TAC concept, the results of previous virtual cracks can also be used. In the following, the *regula falsi* method is used if a previous virtual crack was introduced. The new angle of the virtual crack increment is then given by

$$\varphi_{i+1} = \varphi_i - \frac{\varphi_i - \varphi_{i-1}}{\varphi_{c\,i} - \varphi_{c\,i-1}} \varphi_{c\,i}\,, \tag{10}$$

where $i+1$ is the new virtual crack, i is the current virtual crack, and $i-1$ is the previous virtual crack.

2.3. FEM implementation

The above concepts are employed in combination with FEM simulations. Thus, the configurational forces are evaluated in a discrete FEM mesh in order to compute the configurational force of the crack tip as a volume integral and the crack correction angle using the TAC concept. To predict a crack path, the incremental crack propagation method is used in conjunction with the respective crack propagation concept. The incremental crack propagation is implemented as a Python script that controls the whole procedure. FEM models are prepared in Abaqus using Python, and nodal configurational forces are evaluated using *C* code.

2.3.1. Configurational forces in FEM

This section describes how the configurational forces are evaluated in FEM. The key step in this evaluation is transferring continuous formulations into the discrete formulations of FEM. Nodal configurational forces are evaluated in a postprocessing procedure according to Mueller and Maugin [22] and Mueller et al. [23] by transforming Eq. (3) into a weak, discretised formulation, in which the volume integral is numerically solved in the associated nodal volume. This is implemented in the *C* programming language based on the shape functions of the element types used. These routines are called from the main Python script.

The nodal configurational forces, $\mathbf{f}^j$, in a FEM mesh in the region of a crack tip are shown in Fig. 7. Per definition, configurational forces occur at outer surfaces, material inhomogeneities, cracks, dislocations, vacancies, and voids. Because of the discretisation in FEM, however, nonzero nodal configurational forces $\mathbf{f}^j$ also appear at some nodes apart from the crack tip. Because those $\mathbf{f}^j$ influence the crack driving force, a region Ω is used to obtain the configurational force of the crack tip $\mathbf{f}_{\mathrm{tip}}$. Region Ω is defined by the number of element rings around the crack tip. The nodal configurational forces $\mathbf{f}^j$ of all the nodes belonging to the element rows are summed up to give $\mathbf{f}_{\mathrm{tip}}$ as

$$\mathbf{f}_{\mathrm{tip}} = \sum_{j\in\Omega} \mathbf{f}^j. \tag{11}$$

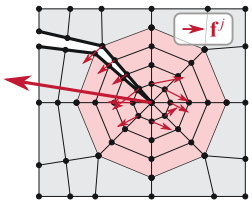

Fig. 7. Mesh of the region of the virtual crack increment with nodal configurational forces $\mathbf{f}^j$. The volume around the crack tip is divided into circular volumes (in this case four element rings).

This $\mathbf{f}_{\text{tip}}$ is used in all crack propagation concepts. The predicted change in strain energy because of the crack propagation is computed by

$$\Delta E = \mathbf{f}_{\text{tip}}^{\text{T}} \mathbf{t}, \tag{12}$$

where $\mathbf{t}$ is the crack propagation vector with the direction and length of the crack propagation, as shown in Fig. 6.

The evaluation region with the most accurate results of the configurational force of the crack tip $\mathbf{f}_{\text{tip}}$ is not known beforehand. For a crack correction in the developed TAC concept (see Section 2.2), the evaluation region Ω_{TAC} can be defined beforehand. This can be explained by the fact that Ω_{TAC} must include all nodes affected by a crack angle correction and exclude all others. Thus, in the current work, the region Ω_{TAC} is thus defined as a circle around the crack tip with a radius equal to the crack increment Δa. In Fig. 7, this region is highlighted by a red background colour. To compute φ_{c}, Eq. (9) is evaluated for Ω_{TAC} as

$$\varphi_{\text{c}} = \arctan\left(\frac{\sum\limits_{j \in \Omega_{\text{TAC}}} \left(\mathbf{p}^j\right)^{\text{T}} \begin{bmatrix} 0 & 1 \\ -1 & 0 \end{bmatrix} \mathbf{f}^j}{\sum\limits_{j \in \Omega_{\text{TAC}}} \left(\mathbf{p}^j\right)^{\text{T}} \mathbf{f}^j} \right), \tag{13}$$

In analogy to the proposed TAC concept, other criteria for correcting the crack angle may be used as well. One possible criterion is to assume crack propagation in the direction of the pure mode I loading of the crack tip [8,13]. This corresponds to the configurational force of the crack tip, $\mathbf{f}_{\text{tip}}$, which points in the direction of the virtual crack increment. This $\mathbf{f}_{\text{tip}}$ can be divided into a parallel component $\text{f}_{\text{tip}}^{\parallel}$ and a perpendicular component $\text{f}_{\text{tip}}^{\perp}$ with respect to the direction of the virtual crack increment. For pure mode I loading, $\text{f}_{\text{tip}}^{\perp}$ becomes zero [8,13]. To obtain the correction angle, $\mathbf{f}_{\text{tip}}$ for the virtual crack is computed using Eq. (11). This single $\mathbf{f}_{\text{tip}}$ describes the loading at the crack tip. The use of one single vector changes Eq. (9) to

$$\varphi_{\text{c}} = \arctan\left(\frac{\text{f}_{\text{tip}}^{\perp}}{\text{f}_{\text{tip}}^{\parallel}} \right), \tag{14}$$

which corresponds to Eq. (1) of the explicit concept. Guo and Li [14] used a similar equation (Eq. (1)) in the global coordinate system to determine the crack propagation direction in the explicit concept, whereas Eq. (14) in the present paper is defined in the local coordinate system and yields the crack correction angle in the TAC concept.

2.3.2. Incremental crack propagation

To predict a crack path with a crack propagation concept, a criterion to determine whether a crack propagates or not is also necessary. In the current work, the deformation-based incremental crack propagation method is used, which is based on the critical energy release rate G_{c} [24].

The algorithm of incremental crack propagation using the TAC concept is illustrated as a flowchart in Fig. 8 starting from an initial FEM model. With each iteration, either the displacement u_i is increased or the crack is propagated according to the TAC concept. The crack propagates if the evaluated energy release rate G is bigger than or equal to the critical energy release rate G_{c}. Otherwise, the applied displacement is increased by the displacement increment Δu. The energy release rate is given by

$$G = \frac{-\Delta E}{\Delta a\, t}, \tag{15}$$

where t is the thickness of the plate, which is set to $t = 1\,\text{mm}$ in the 2D case. As an alternative to the TAC concept, other crack propagation concepts can be used in this incremental procedure as well.

2.4. FEM models

In modelling incremental crack propagation, the crack path arises from the change of the crack angle φ_{p} in each increment. Along the crack path, this φ_{p} varies because of the local loading and is determined by the crack propagation concept. To evaluate the crack propagation concepts themselves, a simplified FEM model is developed. A second FEM model of a three-point bending beam containing holes is introduced, in which crack paths are studied.

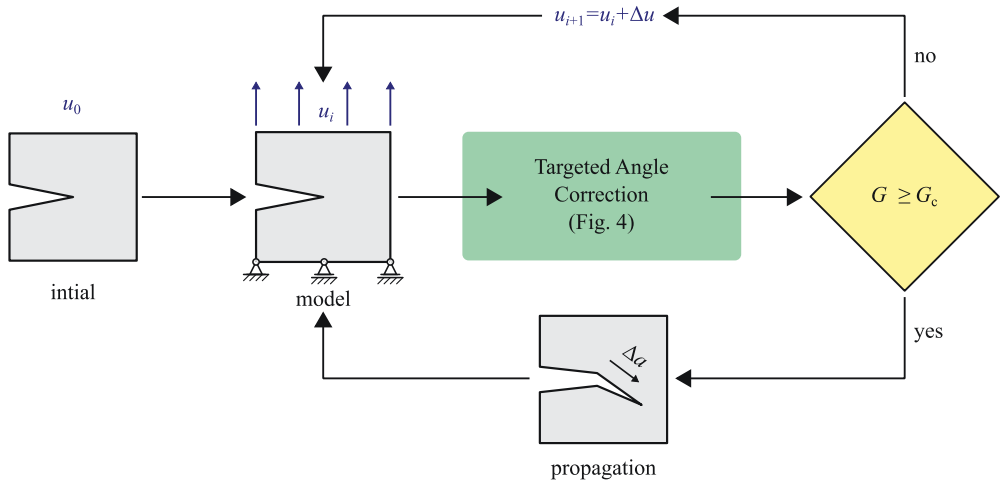

Fig. 8. Flowchart of a deformation-based incremental crack propagation method using the Targeted Angle Correction (TAC) concept explained in Section 2.2.

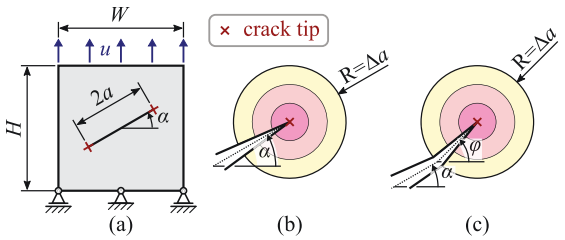

Fig. 9. (a) Sketch of the simplified model with height H and width W. The bottom is fixed in the vertical direction, and a vertical displacement u is applied at the top. The plate contains a starting crack of length $2a$ of an angle α with respect to the horizontal axis. (b) Starting crack tip with crack angle α. (c) Virtual crack increment of length Δa and angle φ for a starting crack with angle α.

Table 1
Parameters of the simplified model.

Parameter name	Symbol	Value	Unit
Width	W	50	mm
Height	H	50	mm
Half crack length	a	15	mm
Crack increment	Δa	1	mm
Radius of the evaluation region around the crack tip	R_Ω	Δa	mm
Number of circular element rows	n_{er}	10	1
Number of elements per element row	n_{epr}	16	1
Permitted angle error	φ_{err}	0.05	°
Young's modulus	E	3100	MPa
Poisson's ratio	ν	0.35	1
Vertical displacement	u	0.5	mm

2.4.1. Simplified model

Before using the TAC concept to predict a crack path, one crack propagation increment is studied in a simplified model. In this model, the orientation of the starting crack is varied. Thus, the TAC concept can be evaluated for selected load situations of a growing crack.

The setup of the simplified model is shown in Fig. 9(a). The geometry consists of a rectangular plate that contains a starting crack. The corresponding model parameters are listed in Table 1. The bottom of the plate is fixed in the vertical direction, where the centre point is additionally fixed in the horizontal direction. A vertical displacement u is applied at the top. The straight crack at the centre of the plate has a length of $2a$ and an angle of α with respect to the horizontal axis. The plate consists of PMMA, which is modelled linear-elastically using a Young's modulus of 3100 MPa according to the material property chart of Ingraffea and Grigoriu [1] and an assumed Poisson's ratio of 0.35. It is assumed that the crack is always open, so no contact is modelled between the crack flanks. The 2D model uses fully integrated eight-noded second-order plane-strain elements and the nonlinear implicit solver of the commercial FEM code Abaqus [25], including the consideration of large deformations.

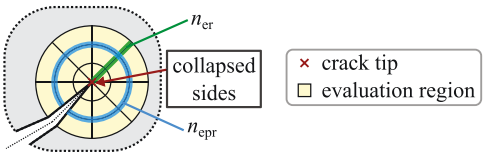

Fig. 10. Sketch of the crack tip mesh, where the element sides next to the crack tip are collapsed. The number of circular element rows n_{er} and the number of elements per element row n_{epr} are assigned.

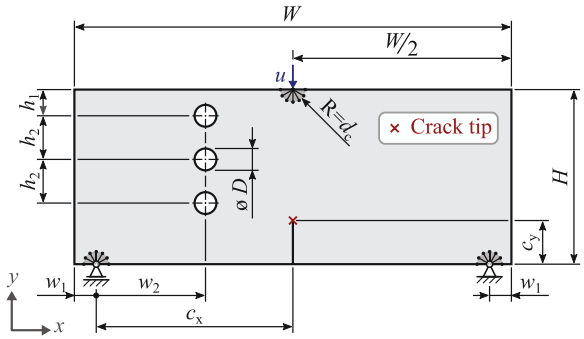

Fig. 11. Sketch of the three-point bending model with its geometric parameters. Three holes and a starting crack (the tip of the crack is marked with a red cross) are included. The model is fixed in the vertical direction at two points at the bottom, and a displacement u is applied at the top in the middle.

The crack in the model contains two crack tips. For the starting crack and virtual crack, circular partitioned regions with a radius of Δa are made around both crack tips. Both regions are meshed identically. Because of the point symmetry, only the region around the right crack tip is considered as the evaluation region. The crack is propagated point symmetrically at the second crack tip. The evaluation region around the crack tip for a starting crack and a virtual crack is shown in Fig. 9(b) and (c), respectively.

Mesh generation is carried out with different mesh sizes for the different regions in the model. In the evaluation region, the elements are arranged as rings around the crack tip, where n_{er} is defined as the number of rings in the radial direction and n_{epr} defines the number of elements per ring (see Fig. 10). For the innermost ring of elements, the side next to the crack tip is collapsed onto the crack tip node. Along the crack outside the evaluation region, a mesh seed of Δa divided by n_{er} is used. The global mesh size is used for the remaining regions of the model, which is determined after studying the mesh size.

The model is used to evaluate the necessary global mesh size and the performance of the TAC concept. A comparison of the crack propagation concepts presented in Section 2.1 is carried out, where a wide range of starting crack angles is studied. As the reference propagation direction, the direction for MERR is used, as shown in Section 2.1.2. Alternatively, singular elements, where the midside node position is moved to one fourth of the element's edge length, can be used around the crack tip to capture the crack tip singularity. The effect of using singular elements was evaluated based on the simplified model and was found to not have any significant influence. Compared with the regular mesh using the TAC concept, the average and maximum deviations for φ_p are 0.02% and 0.05%, respectively. For the strain energy of the whole model and predicted energy release rate using configurational forces, small deviations of 0.04% and 0.05%, respectively, are obtained. Therefore, the results presented below are based on the regular crack tip mesh.

2.4.2. Three-point bending model

To study the prediction of full crack paths, the three-point bending model is used. Crack paths are predicted with the TAC concept using the incremental crack propagation method presented in Section 2.3.2 for various starting crack positions. The predicted TAC crack paths are evaluated using corresponding results of the explicit crack propagation concept and the experimental results.

The setup of the three-point bending model, which is taken from Ingraffea and Grigoriu [1], is shown in Fig. 11. The rectangular plate contains three holes and a vertical crack at the bottom surface. The model parameters are listed in Table 2. To avoid numerical effects because of boundary conditions applied to one single node, reference points are created at the positions of structural supports, where the boundary conditions are applied. The reference points are rigidly coupled to nodes within a radius of d_c, where all translational degrees of freedom are coupled. The plate is fixed at the two bottom reference points in the vertical direction. Additionally, the right bottom reference point is fixed in the horizontal direction. A vertical displacement $u = 1.5$ mm is applied to the middle reference point of the top edge. The plate consists of PMMA, which is modelled as described in Section 2.4.1. As in the simplified model, no contact between the crack faces is modelled. Fully integrated eight-noded second-order plane-strain elements and the nonlinear implicit solver of Abaqus [25] are used, including the consideration of large deformations.

The evaluation region around the crack tip is partitioned and meshed, as described in Section 2.4.1. Different mesh seeds are chosen: Δa for the crack outside the evaluation region, Δa for the holes and 1 mm for the region around the reference points. The remaining regions of the model are meshed with a global mesh size of 2 mm.

Table 2
Parameters of the three-point bending model.

Parameter name	Symbol	Value	Unit
Width	W	508	mm
	w_1	25.4	mm
	w_2	127	mm
Height	H	203.2	mm
	h_1	31.75	mm
	h_2	50.8	mm
Hole diameter	D	12.7	mm
Radius of rigid coupling	d_c	6.35	mm
Radius of the evaluation region around the crack tip	R_Ω	Δa	mm
Number of circular element rows	n_{er}	10	1
Number of elements per element row	n_{epr}	16	1
Young's modulus	E	3100	MPa
Poisson's ratio	ν	0.35	1
Vertical displacement	u	1.5	mm

Table 3
Starting cracks in the three-point bending model.

Crack	c_x	c_y	Unit
A	129.8	38.1	mm
B	126.95	37.5	mm
C	108.1	37.6	mm

The model is used to investigate the crack paths predicted with the incremental crack propagation method (see Section 2.3.2). The goal is to examine the influence of the crack propagation concepts on the crack path without the influence of the changing load. Therefore, the critical energy release rate for crack propagation is set to zero for all crack propagation concepts, which results in continuous crack growth at a constant load. Note that in the experiment, the load can increase during crack propagation. Thus, nonlinear effects of this load increase are thus not accounted for in the presented model. The influence of the permitted angle error using the TAC concept is studied. Additionally, a comparison of the explicit crack propagation and the TAC concept for the three starting cracks listed in Table 3 is performed. The starting crack *A* is chosen at a position, where the resulting crack path is very sensitive to the crack propagation concept. For the starting cracks *B* and *C*, experimental data are available [1].

3. Results and discussion

3.1. Simplified model

In this section, the necessary mesh size to compute accurate results of the strain energy of the whole model and propagation angles with the TAC concept are evaluated. The propagation angle based on the criterion of MERR is taken as a reference to assess explicit and implicit concepts for crack propagation.

Following the criterion of MERR, the crack propagates in the direction of the minimum strain energy of the whole model. The strain energy of the whole model will be further referred to as the global energy E_{glob}. This direction is found as described in Section 2.1.2 by the minimum of a quadratic polynomial fitted to the global energy for introduced virtual cracks. To identify the minimum, an accurate computation of the global energy is required. The influence of the global mesh size on E_{glob} is illustrated in Fig. 12. For the three starting crack angles α of 0°, 30°, and 60°, E_{glob} is plotted vs. the angle of the virtual crack increment φ for a varying global mesh size. Appropriate ranges of φ are used for the three starting crack angles α. For a decreasing mesh size, the global energy E_{glob} generally decreases, reaching a convergence for a mesh size below 0.5 mm. For each crack angle α, the quadratic polynomial is drawn as a yellow curve, with its minimum marked as a red dot. Using a mesh size of 0.25 mm, propagation angles of 0°, −4.06°, and −3.87° are found for starting crack angles α of 0°, 30°, and 60°, respectively. Below, a global mesh size of 0.5 mm is used to compute the global energy of the model.

In the TAC concept, the global mesh size also influences the predicted crack propagation angle φ_p (see Fig. 13). The predicted φ_p is plotted vs. a starting crack angle α ranging from 0° to 60° (2° steps) for a permitted angle error $\varphi_{err} = 0.05°$. For a mesh size below 1 mm, the predicted φ_p is almost independent of the mesh size. The red dots mark the crack propagation angle determined using the global energy, see Fig. 12. As shown below, to compute φ_p, a global mesh size of 1 mm and $\varphi_{err} = 0.05°$ are used with the TAC concept.

The explicit and the implicit crack propagation concepts presented in Section 2.1 are used to predict the crack propagation angles in Fig. 14, where the crack propagation angle φ_p is plotted vs. a starting crack angle α ranging from 0° to 60° (2° steps). The reference propagation direction, which is shown as a black curve in both diagrams, is determined by the implicit concept based on the global energy (see Fig. 12). Virtual cracks are used to evaluate the global energy for the fit. Eight virtual cracks ($n_c = 8$) are distributed equidistantly in a range of ±4° around the propagation direction predicted with the TAC concept.

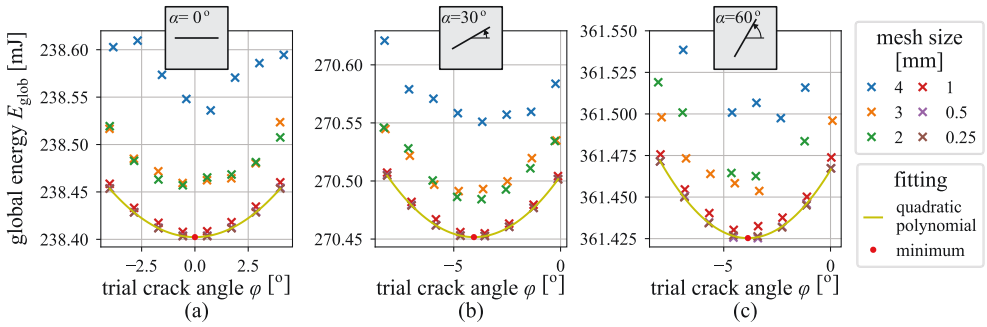

Fig. 12. Influence of the global mesh size on the values of the global energy (coloured crosses) for virtual cracks with three starting crack angles: (a) $\alpha = 0°$, (b) $\alpha = 30°$, and (c) $\alpha = 60°$. The range of the angle of the virtual crack increment φ is located around the local global energy minimum. The yellow line represents a quadratic polynomial function that is fitted to the energy values for a mesh size of 0.25 mm, which uses least squares method. The minimum of the polynomial function is marked by a red dot.

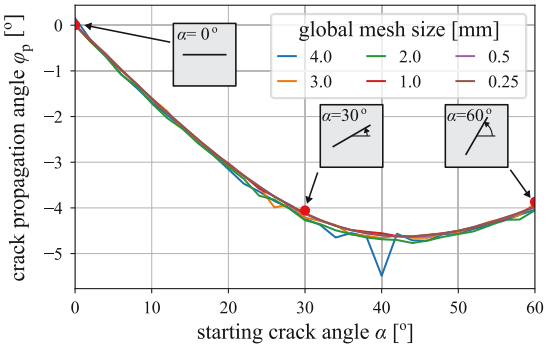

Fig. 13. Influence of the global mesh size on the predicted crack propagation angle using the TAC concept. The red dots mark the values of the starting crack angle α for 0°, 30°, and 60°, which were evaluated in Fig. 12.

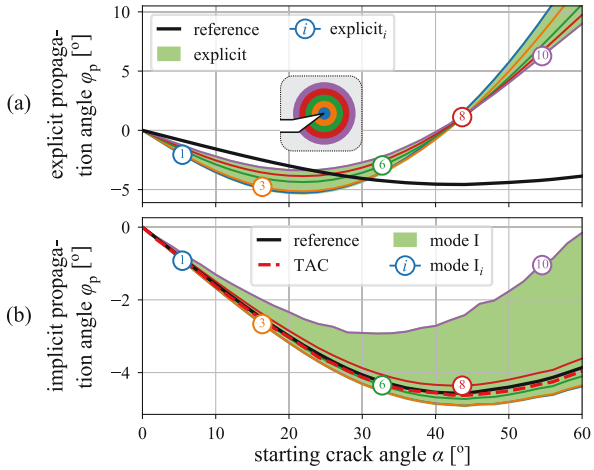

Fig. 14. Comparison of the results for the crack propagation angle φ_p from the explicit and implicit crack propagation concepts with the reference propagation angle for MERR (black line). The predicted φ_p of the explicit propagation concept and the implicit propagation concept for mode I situation at the crack tip is evaluated for variously sized evaluation regions.

The propagation direction φ_p predicted by the explicit crack propagation concept presented in Section 2.1.1 is shown in Fig. 14(a). The evaluated propagation angles for various evaluation regions are shown as coloured numbered lines, where the number defines the element rings used for evaluation. The range of the predicted values of φ_p is shaded in green. Fig. 14(b) shows the propagation

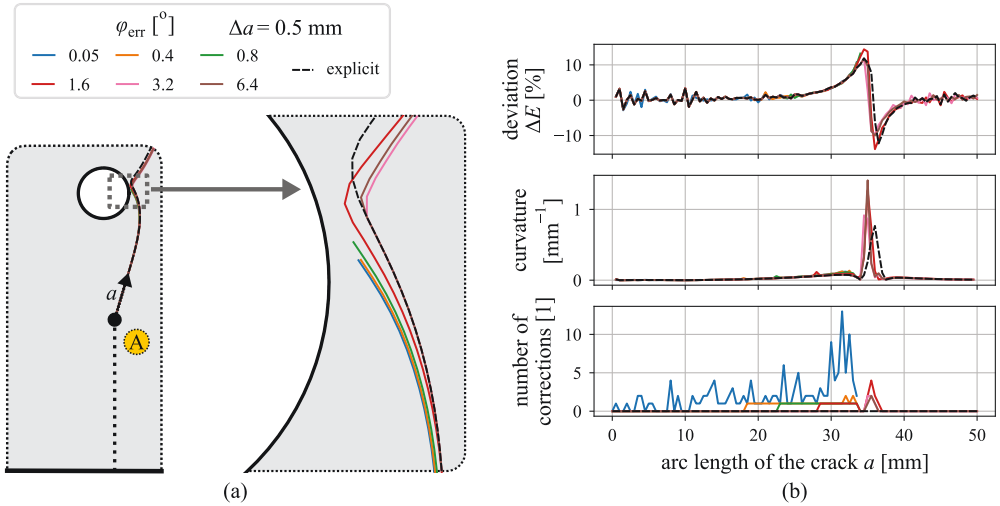

Fig. 15. Results of the incremental crack propagation based on the TAC concept for various crack angle errors for the starting crack *A*: (a) shows the crack paths and (b) illustrates the deviation of the predicted change in strain energy ΔE computed with configurational forces to the change in strain energy of the whole model, the curvature of the crack path and the necessary corrections for the given crack angle error vs. the arc length of the crack.

direction φ_p predicted using the implicit crack propagation concepts presented in Section 2.1.2, where crack corrections are performed. The coloured lines show the predicted φ_p values for the implicit propagation concept of a mode I situation at the crack tip, which is evaluated for the various evaluation regions defined above. The range of the predicted values of φ_p is shaded in green. The corresponding φ_p of the TAC concept presented in Section 2.2 is plotted by the red dashed line. As the first virtual crack direction for the implicit concepts, the explicit propagation direction evaluated for an evaluation region of three element rows around the crack tip is used.

The crack propagation angle φ_p predicted by the explicit propagation concept show all deviations compared with the reference propagation angle. The deviation results from a lack of fulfilment of the physical meaning of the configurational forces using the explicit crack propagation concept, as shown in Section 2.2. The results for the implicit propagation concept for the mode I situation at the crack tip show less deviations, which depend on the size of the evaluation region chosen. However, the size of the evaluation region that yields the most accurate results is not known beforehand. The results of the TAC concept, in which the evaluation area includes the entire geometry affected by a crack correction, agree well with the reference propagation angle because of their different computation. Two angle corrections (three virtual cracks) are needed using the TAC concept for a permitted angle error $\varphi_{err} = 0.05°$ for all crack angles α, except for 0° and 30°. The number of corrections is influenced by the deviation of the explicit crack propagation angle from the reference propagation angle because in the implicit concepts, the explicit crack propagation angle is used as the first virtual crack. For the crack angles α of 0° and 30°, zero and one correction were necessary, respectively. On average, the TAC concept needs 2.90 virtual cracks for each crack propagation. It should be mentioned that seven virtual cracks had been introduced for each crack propagation using the implicit concepts in [13]. Therefore, the TAC concept requires 2.4 times less computational effort if only the model preparation and the FEM solver are considered.

3.2. Three-point bending model

In this section, the influence of the permitted angle error on a crack path using the incremental crack propagation with the TAC concept is evaluated. This is done by comparing the predicted crack paths of the TAC concept, the explicit concept, and experiments. Because similar results had been obtained for a finer global mesh, a global mesh size of 2 mm is used in the model for the results shown here.

The influence of the permitted angle error φ_{err} is studied using a constant crack increment $\Delta a = 0.5$ mm and the starting crack *A* defined in Table 3. The crack paths for the various values of φ_{err} are plotted in Fig. 15(a), where the region of interest near the hole is enlarged. The explicit curve is equivalent to $\varphi_{err} = \infty$, where no correction is performed. The deviation of the predicted change in strain energy ΔE to the change in strain energy of the whole model because of crack propagation, the curvature of the crack path, and the necessary number of corrections vs. the arc length of the crack a is shown in Fig. 15(b). The arc length a starts from the starting crack tip (see Fig. 15(a)).

The predicted ΔE is computed using Eq. (12) with the configurational force of the crack tip $\mathbf{f}_{tip}$ computed for an evaluation region of three element rings around the crack tip. The deviation in the predicted ΔE and the number of necessary corrections increases as the crack path curvature increases. In addition, the number of necessary corrections decreases for higher φ_{err}. The predicted crack paths are nearly identical for $\varphi_{err} \leq 0.4°$, so the value of $\varphi_{err} = 0.4°$ is used. For $\varphi_{err} = 0.4°$, no correction is necessary at the beginning, which corresponds to explicit crack propagation. Otherwise, one correction is necessary, except near the hole where it is

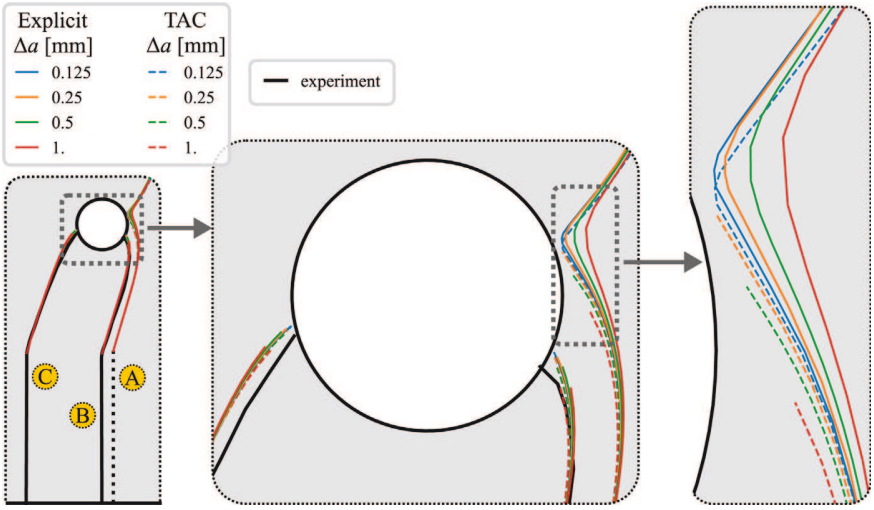

Fig. 16. Crack paths determined with the incremental crack propagation method based on the TAC concept (dashed coloured lines) and the explicit crack propagation concept (solid coloured lines). For the propagation, various crack increment lengths Δa are used. For the starting cracks B and C, the experimental results from [1] are shown as black lines.

sometimes possible for two corrections to occur. For smaller values of φ_{err}, the necessary number of corrections increase without a noticeable effect on the crack path. For $\varphi_{\text{err}} = 0.05°$ and $\varphi_{\text{err}} = 0.4°$, the TAC concept needs an average of 3.06 and 1.49 virtual cracks for each crack propagation, respectively. As mentioned before, seven virtual cracks had been introduced for each crack propagation using the implicit concepts in [13]. Thus, the TAC concept requires less computational effort. For an angle error $\varphi_{\text{err}} = 0.4°$, 4.7 times less computational effort is required.

The crack paths of the explicit crack propagation and the TAC concept for $\varphi_{\text{err}} = 0.4°$ and various crack propagation increments Δa are shown in Fig. 16. The crack paths for the three starting cracks *A*, *B*, and *C* (defined in Table 3) are plotted on the left-hand side. The region of interest near the hole, where the curvatures of the crack paths increase, is enlarged in the centre of Fig. 16. Good agreement is found between the explicit and TAC crack paths for the starting cracks *B* and *C*. The various crack increments Δa show no significant difference in the crack paths for the TAC concept, the explicit concept, and the experimental data from [1]. However, even the TAC concept cannot fully capture the experiment, even for a small Δa. The crack path *A* is most sensitive to the used crack propagation concept and Δa, which can be seen in the enlarged area near the hole on the right-hand side of Fig. 16. An early inaccuracy of the crack propagation angle can lead to a large deviation in the later crack path. The explicit concept underestimates the change in the crack angle with increasing Δa, because the configurational force of the crack tip of the current crack is used to predict the propagation angle of the increment (see Fig. 16). The TAC concept also shows a dependence on Δa, in which virtual cracks are used to determine the crack propagation direction. The size of Δa influences the approximation of a smooth crack path with straight crack increments. The TAC concept is accurate for one increment of Δa. The size of Δa affects the load redistribution during crack propagation, yielding a different propagation direction that affects the later crack path. Small Δa values are necessary to accurately capture large crack curvature. For increasing Δa using the TAC concept, an overestimation of the curvature near the hole is observed in Fig. 16. Because of the decreasing difference of the crack paths for decreasing Δa, the TAC concept for $\Delta a = 0.125$ mm is assumed to fulfil the criterion of MERR sufficiently, whereas the result of the explicit concept for $\Delta a = 0.25$ mm shows more deviation than the TAC concept for the same Δa.

4. Summary and conclusions

The current work has presented a concept to predict the direction of crack propagation with FEM using configurational forces. The method can be generally applied to other brittle materials. Classically, the configurational force of the crack tip is already used to predict the crack propagation direction. In the developed concept, configurational forces are used to iteratively correct the introduced virtual cracks. The current paper shows how to use the configurational forces concept to predict the crack propagation direction to fulfil the propagation criterion for maximum energy release rate. The developed concept is called Targeted Angle Correction (TAC) and is evaluated in terms of accuracy and efficiency:

- The accuracy of the concept is evaluated for a single crack propagation increment in a simplified model, in which the kink angle for the crack propagation can be set individually. The TAC results agree well with the reference propagation direction, while the explicit and the implicit concepts based on configurational forces show deviations. The deviations depend on the chosen evaluation region to predict the crack propagation direction, which is not known beforehand. The explicit concept shows large deviations because only information of the current crack is used, while the implicit concepts use information from

propagated virtual cracks. Less computational effort per crack propagation is observed when using the TAC concept compared with other implicit concepts.

- Crack paths are predicted with the incremental crack propagation method in a three-point bending model. Investigating the influence of the permitted angle error shows that a permitted angle error that is too small results in unnecessary corrections, which results in a higher computational effort with a negligible influence on the crack path. A suitable permitted angle error was found for the used model. Also, the number of necessary corrections depends on the curvature of the crack path. For small curvatures, the TAC concept behaves like the explicit concept. Otherwise, corrections are necessary when using the TAC concept, while the explicit concept lacks in accuracy.
- For the two selected crack paths in the three-point bending model, the explicit and the TAC concept provide similar results that are also close to the experimental results of the PMMA specimens.
- One additional crack path is introduced in the three-point bending model, which is quite sensitive to the used crack propagation concept and the chosen crack propagation increment length. To fulfil the propagation criterion for maximum energy release rate, the TAC concept gives more accurate results compared with the explicit concept, even for a larger increment length. However, the accuracy still depends on the curvature of the crack path and the increment length, which determines the computational effort. The concept could be improved in the future by updating the crack increment length depending on the local crack curvature.
- In the simplified model, a mesh size at the crack tip of one tenth of the crack increment length Δa has proven to be sufficient. To accurately compute the crack path, it is crucial that Δa is small enough to appropriately approximate the crack path. Hence, a smaller value for Δa is generally needed for crack paths with a small curvature radius; however, no general quantifiable recommendation can be given beforehand about the selection of Δa. When the TAC concept is used for a new application, a convergence study needs to be performed for Δa.

The developed concept gives more accurate results than the explicit concept in approximately 150% of the computational time. The TAC concept shows good results for curved crack paths, which is particularly important in modelling crack propagation in heterogeneous materials. Because of the material-independent formulation of configurational forces, it can be applied to nonlinear material models. The TAC concept opens up new possibilities in 3D cases, where computational efficiency plays a big role.

Declaration of competing interest

The authors declare that they have no known competing financial interests or personal relationships that could have appeared to influence the work reported in this paper.

Acknowledgments

This research was supported by the Austrian Research Promotion Agency (FFG) within the "BRIDGE" framework as part of the project "Entwicklung einer Methodik zur Vorhersage des Versagens in elastomeren Gurten mittels Finite Elemente Simulation", grant agreement 864702.

References

[1] Ingraffea AR, Grigoriu M. Probabilistic fracture mechanics: A validation of predictive capability. Technical Report, Cornell Univ Ithaca Ny Dept OF Structural Engineering; 1990, p. 155.
[2] Griffith AA. VI. The phenomena of rupture and flow in solids. Philos Trans R Soc A 1921;221(582–593):163–98.
[3] Irwin GR. Analysis of stresses and strains near the end of a crack traversing a plate. J Appl Mech 1957;24(3):361–4.
[4] Rice JR. A path independent integral and the approximate analysis of strain concentration by notches and cracks. J Appl Mech 1968;35(2):379–86.
[5] Erdogan F, Sih GC. On the crack extension in plates under plane loading and transverse shear. J Basic Eng 1963;85(4):519–25.
[6] Otsuka A, Mori K, Miyata T. The condition of fatigue crack growth in mixed mode condition. Eng Fract Mech 1975;7(3):429–39.
[7] Broberg K. On crack paths. Eng Fract Mech 1987;28(5–6):663–79.
[8] Ma L, Korsunsky AM. On the use of vector J-integral in crack growth criteria for brittle solids. Int J Fract 2005;133(4):L39–46.
[9] Eshelby JD. The force on an elastic singularity. Philos Trans R Soc A 1951;244(877):87–112.
[10] Hellen TK. On the method of virtual crack extensions. Internat J Numer Methods Engrg 1975;9(1):187–207.
[11] Gurtin ME, Podio-Guidugli P. Configurational forces and the basic laws for crack propagation. J Mech Phys Solids 1996;44(6):905–27.
[12] Miehe C, Gürses E. A robust algorithm for configurational-force-driven brittle crack propagation with R-adaptive mesh alignment. Internat J Numer Methods Engrg 2007;72(2):127–55.
[13] Brouzoulis J, Larsson F, Runesson K. Strategies for planar crack propagation based on the concept of material forces. Comput Mech 2011;47(3):295–304.
[14] Guo Y, Li Q. Material configurational forces applied to mixed mode crack propagation. Theor Appl Fract Mech 2017;89:147–57.
[15] Simha N, Fischer F, Shan G, Chen C, Kolednik O. J-integral and crack driving force in elastic–plastic materials. J Mech Phys Solids 2008;56(9):2876–95.
[16] Kolednik O, Predan J, Fischer F. Cracks in inhomogeneous materials: Comprehensive assessment using the configurational forces concept. Eng Fract Mech 2010;77(14):2698–711.
[17] Kolednik O, Schöngrundner R, Fischer FD. A new view on J-integrals in elastic–plastic materials. Int J Fract 2014;187(1):77–107.
[18] Özenç K, Kaliske M. An implicit adaptive node-splitting algorithm to assess the failure mechanism of inelastic elastomeric continua. Internat J Numer Methods Engrg 2014;100(9):669–88.
[19] Özenç K, Chinaryan G, Kaliske M. A configurational force approach to model the branching phenomenon in dynamic brittle fracture. Eng Fract Mech 2016;157:26–42.
[20] Onsager L. Reciprocal relations in irreversible processes. I. Phys Rev 1931;37(4):405–26.

[21] Svoboda J, Turek I, Fischer FD. Application of the thermodynamic extremal principle to modeling of thermodynamic processes in material sciences. Phil Mag 2005;85(31):3699–707.
[22] Mueller R, Maugin GA. On material forces and finite element discretizations. Comput Mech 2002;29(1):52–60.
[23] Mueller R, Gross D, Maugin GA. Use of material forces in adaptive finite element methods. Comput Mech 2004;33(6):421–34.
[24] Frankl S, Pletz M, Schuecker C. Incremental finite element delamination model for fibre pull-out tests of elastomer-matrix composites. Procedia Struct Integr 2019;17:51–7.
[25] Abaqus 2020. Dassault Systèmes; 2020.